Università degli Studi di Messina

DIPARTIMENTO DI SCIENZE MATEMATICHE ED INFORMATICHE, SCIENZE FISICHE E DI SCIENZE DELLA TERRA - MIFT

Corso di Dottorato di Ricerca in Fisica

PhD Thesis

Ion source by Laser-generated plasmas and relative diagnostics

Candidate:
Giovanni Ceccio

S.S.D. Fis. 01

Tutor:
Prof. Lorenzo Torrisi

PhD Coordinator:
Prof. Lorenzo Torrisi

Ciclo XXX

Contents

List of Figures

List of Tables

Introduction

The aim of my PhD was the study and characterization of plasmas produced by laser-matter interaction, the relative diagnostics, the mechanism of ion production and acceleration and some possible applications. The choice of this topic is to be sought at in the strong impact it has in modern research. The use of lasers as ion and electron accelerating systems and like x-ray source can certainly have a strong influence on the community, if laser-generated plasmas could be used as new types of ion accelerators, it would meet new scenarios for adronic therapy, with considerable savings in economic terms the current cost of accelerators. Moreover, such systems allow, potentially, to be able to obtain any type of nuclear reaction and consequently also nuclear fusion reactions. A controlled fusion reactor would be a solution to many social and environmental problems. In the last years, in fact, several laboratories and facilities have been built, not only to study the basic physics related to the formation and expansion of non-equilibrium plasmas generated by pulsed lasers, but also to realize possible applications. For example, at the National Ignition Facility of the Lawrence Livermore National Laboratory there is a high-power laser facility especially used to perform experiments on Inertial Confinement Fusion. At the LULI laser laboratory in France, that is one of the most powerful in the world (laser intensity up to 10^{20} W/cm^2), studies regarding inertial confinement fusion, particle acceleration, shock waves, X-rays and $\gamma - rays$ produced by laser ablation are carried out. Brookhaven National Laboratory in USA and the RIKEN laboratory in Japan are developing facilities in order to inject ions produced by laser-generated plasmas into classical particle accelerators for improving their energy and producing new nuclear reactions in-

duced by heavy elements. An experiment that followed this idea was performed in 2002 at LNS-INFN laboratory of Catania, using an hybrid ion source (LIS-ECRIS). The new idea was to couple an equilibrium plasma, created by a classical ECR ion source, with a non-equilibrium plasma, created by pulsed laser ablation, in order to obtain high currents of highly charged ion beams to be injected inside the cyclotron. In this thesis work I deal with the diagnostics of ions produced in a non-equilibrium plasma generated by pulse laser ablation. Ion detection was mainly performed by using two types of electrostatic devices: ion collector (IC) and ion energy analyzer (IEA). Other kind of diagnostics are explained in this thesis in order to provide a complete panorama on the possible diagnostics that can be used in the study of plasma. The measures reported in this thesis were mainly conducted in three laboratories: Laser-Plasma laboratory of Department of Physics of Messina, CELIA Laboratory in Bordeaux and Brookhaven National Laboratory in New York State. In this thesis the first chapter is an introduction about the definition of plasma state, the characteristics of plasma that we are able to measured and the plasma production from laser-matter interaction. This interaction can be performed using several condition and the plasma properties depend strongly from these. We will see like the plasma production by laser ablation depends from laser wavelength and fluence and once the ablation threshold has passed the laser energy is assorbed by the plasma in order to accelerate the particles present in the plasma, like electron and ions. Speaking about the particles energy we will study the particle energy distributions, in the last years was developed by L.Torrisi (2016. REDS 171:1-2, 34-44) a model in wich the ion velocity depends on many factors of which the most important are the plasma temperature, the adiabatic gas expansion in vacuum and the Coulomb acceleration. The ion energy distributions of the emitted ions from the plasma can be well explained by the Coulomb–Boltzmann-Shifted function, with a cut-off limitation at high energy for a wide range of laser intensities. The at the end of the chapter will be show the regime for ion acceleration that depends from the laser intensity and target thickness. These regimes cover the laser intensity range from $10^9 - 10^{22}$ W/cm^2 for relative ion energies from 100 eV/z up

to 100 MeV/z. In the second chapter are presented several diagnostic techniques useful for the determination of ion energy, plasma temperature, neutral particles detection and optical measurement of plasma properties. The diagnostic techniques can be divided in on line and off line diagnostic, using time of flight techniques or other to understand quickly the plasma properties during the experiment, while the off-line diagnostics are studies performed after the experiment on the target or on the detector that need of some kind of treatment to see the result, examples are the study of surface profile obtained on the crater created on the target during the interaction and the track detector CR 39 that need of chemical etching in order to understand the energy of particles that interacted with the detector. Some diagnostics use the trajectory deflection that undergo the charged particles through electrical and / or magnetic fields, these techniques are described in third chapter where are described the Ion Energy Analyzer (IEA) that consist of in 90° electrostatic deflector developed for the construction of ion energy distribution per charge state of the ionic species present in the plasma. The limitation of this device consist of in the big number of laser shots needed for the analysis. For this reason many peaple are developed the use of Thomson Parabola Spectrometer (TPS) that use the deflection due to the presence of a Magnetic and an Electric fields. In a typical TPS, a pencil beam of ions, selected by the pinhole located at its entrance, travels through regions of parallel magnetic and electric fields applied transversely to the beam axis. The magnetic field determines the y-coordinate of the ions on the detector, depending on their energy, while the electric field deflects the ions along the x-axis according to their Z/A ratio. The last device described in the third chapter is a magnetic spectrometer developed inside our laboratory that consist of in a fixed magnetic field and in a multi faraday cup system for the analysis of angular distribution of plasma with and without magnetic field. This system allows to study many properties of plasma producing in several acceleration regime. The fourth chapter is very important because describe the experiment performed in Brookhaven National Laboratory and in Messina laboratory for the experimental studies of heavy ion beam generation from laser ablation plasma of gold coated aluminum target sample using

IEA system at two different laser intensities. The experiments were performed with the main aim to study the produced plasma for Ion Source applications. Last chapter is a description of applications in Plasma Source for Ion Acceleration, are described devices like Radio Frequency Quadrupole (RFQ) and Superconducting Cyclotrone for the Ion Acceleration and the method that can be developed for the use of Laser Ion Source like main source of these systems. The post acceleration systems are important part of the discussion because in addition to the application in accelerator can be used for the Ion Implantation, a very important technique used in material studies. The last part of the chapter describe the results that can be obtained in ion acceleration using high intensity lasers and advanced targets. Finally, achievements and future prospects will be discussed in the conclusions.

Chapter 1

Plasmas Physics

If we increase the temperature of a gas beyond a certain limit, it does not remain a simple gas, it enters in a particular regime where there are energies and themperatures of particles that overcome the electromagnetic force that bind the electrons to the atomic nuclei. Under these conditions instead of a hot gas composed of fast neutral particles there is a population of particles composed of negative, positive and neutral particles, this environment is called plasma system. In addition to the particles, the plasma consist of all fields (magnetic, electric and electromagnetic) that are generated inside of the system. On Earth, plasma occur naturally only in lightning and in the aurora. Beyond our atmosphere, however, there is a plasma system (called magnetosphere) formed by the interaction of Earth's magnetic field and the solar wind. The sun and other stars are made of plasma, making of the plasma state the more diffused in the universe.

1.1 Properties and parameters

The ionization of system is necessary to the formation of plasma and this formation can be due to interaction with radiofrequency, high intensity laser pulse, electric breakdown, charge particle and all phenomena that are able to ionize a gas.

1.1.1 Ionization degree

The ionization degree of a plasma is the proportion of atoms that have lost or gained electrons. The degree of ionization χ is related to parameters the characterize the thermodynamic state of the plasma.

$$\chi = \frac{n_i}{n_i + n_0} \tag{1.1.1}$$

The **Saha equation** describes the n_i/n_0 ratio in a plasma as a function of temperature, density and ionization energy of atoms [1]:

$$\frac{n_i}{n_0} \approx 2.4 \times 10^{15} \frac{T^{3/2}}{n_i} \exp\left[-I/kT\right] \tag{1.1.2}$$

where n_i is the density of atoms in the ith state of ionization, n_0 is the density of atoms in ground state, T the temperature, I ionization energy for i^{th} level and k the Boltzmann constant.

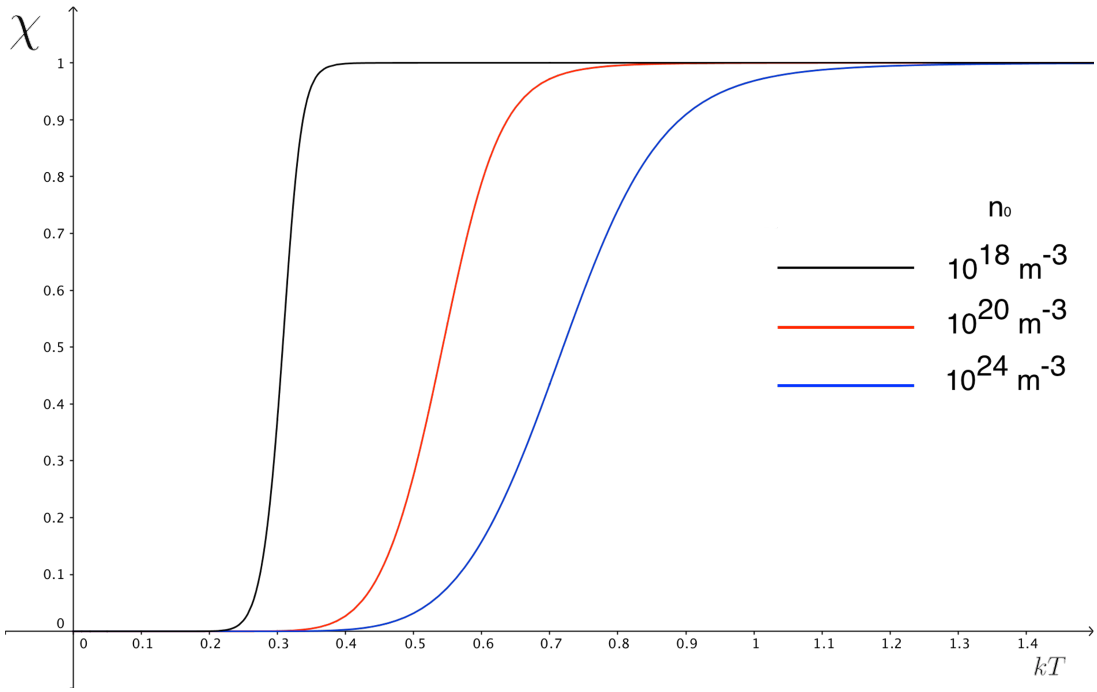

Figure 1.1: *Example of ionization degree for gold gas at three differents densities.*

In Fig.1.1 it is possible to observe the simulated ionization degree curves, these have different behavior for different densities, in particular with lower densities the ionization degree becomes quickly 1 even if the temperature is low. Instead higher densities allows to reach the maximum value slowly and in smoothing way.

1.1.2 Ionization energy

The *ionization energy* is the amount of energy required to remove an electron in an atom. There isn't just an energy of ionization, according to the number of electrons that are removed from the atom there are the $1^{st}, 2^{nd}, \ldots, i^{th}$ ionizations. Generally I increase as one moves from left to right within a given period of periodic table and decrease as one moves down a given group.

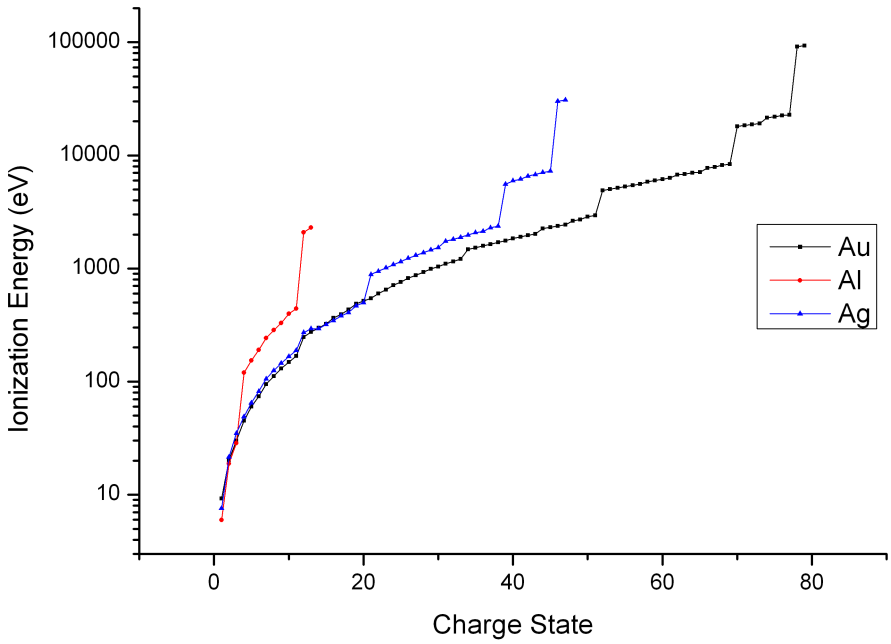

Figure 1.2: *Example of ionization energies of all electrons for three different elements, in black dots gold ions, in red aluminium ions and in blue silver ions*

In Fig.1.2 are shows the ionization energies of Al, Ag and Au, it is possible to see the differences, for the same charge state it is simplest to remove electrons at the heaviest element. In the trends there are some steps, these corrispond to particular electronic configurations that give stability to the ionizated atom. The Tab.1.1 shows the value for ionization energy of Au up to 20 and Al all charge state.

Table 1.1: Ionization Energy for Al and Au

Charge state	**I (eV) Au**	**I (eV) Al**
1	9.22	5.98
2	20.2	18.82
3	30	28.447
4	45	119.99
5	60	153.825
6	74	190.49
7	95	241.76
8	112	284.64
9	130	330.21
10	149	398.65
11	168	442
12	248	2085.97
13	275	2304.14
14	299	
15	324	
16	365	
17	392	
18	433	
19	487	
20	517	

It is important to have as a reference the ionization energies because the charge states present in a plasma depends on the temperature that it has, and vice versa. So when we have instruments capable of measuring the temperature of the plasma, we could make an estimate of the charge state present. A completely isolated plasma is globally neutral, however, it is composed of at least two species of charged particles (an ion species partially or totally ionized, and an equivalent number of electrons) its dynamic behavior is different from that of a neutral gas, because the molecular forces at short ranges which determine the dynamics of a neutral gas are replaced by electromagnetic forces, which are exercised between charges and currents, which are long-range.

1.1.3 Lotz's Theory

A calculation of the distribution of atoms over their ionization stages and quantum states is one of the key steps in the modelling of laboratory plasma experiments. For ions of any chemical element, the number of direct ionization transitions is small in comparison with the total number of transitions required for collisional–radiative calculations which provide a composition history of non-LTE (local thermodynamic equilibrium) plasmas. The shortage in the cross section data motivated a search for empirical formulae capable of reasonably accurate prediction for any transition. The most successful expression was proposed 30 years ago by Lotz [2]-[3], for total direct ionization cross sections $\sigma_{zq}^{inz}(\varepsilon)$ for ionization into all possible final states q' of A_{z+1} [4]:

$$\sigma_{zq}^{inz}(\varepsilon) = 4.5 \times 10^{-14} \sum_k \xi_{zqk} \frac{\ln(\varepsilon/I_{zqk})}{\varepsilon/I_{zqk}} cm^2 \tag{1.1.3}$$

where the subscript z = 2, 3, 4, . . . denotes an ionization stage of target-ion A_z , the subscript q denotes a state (energy level) to be ionized and the subscript q' denotes a state of product ion A_{z+1} just after removal of the electron. Here (ε) is the incident electron energy, the subscript k runs over all nl-subshells of $A_{z,q}$, I_{zqk} is the minimal energy required for ionization from state q into state k (which may be an excited state) and ξ_{zqk} is the number of equivalent electrons in the nl-subshell which has to lose one

electron for the transition. This relationship takes into account the Bethe asymptotic dependence for behaviour of the ionization cross sections for high incident electron energy ($ln(\varepsilon)/\varepsilon$) and used the following classical scaling rule:

$$\sigma_{zq}^{inz}(\varepsilon)I_{zqk}^2 = f(\varepsilon)/I_{zqk}) \tag{1.1.4}$$

1.1.4 Debye length

The essential parameter to define the state of plasma is the presence of free charges: a plasma will therefore not be physically characterized by the density and the temperature separately, but through a combination which ensures the substantial presence of ionization phenomena. In an ionized gas, the prevalence of the collective effects can be reached by increasing the number of interacting charged particles. Therefore it is possible, for a total number of charges sufficiently large that the electric fields (and magnetic), giving rise to a behavior in many bodies, unlike what takes place in a neutral gas in which the particles interact primarily in short-range force. There is a length over which in an ionized gas microscopic effects are mediated collectively, this length is called *Debye length* λ_D. Around each charge q, plasma creates a space charge cloud that reduces the Coulomb electric potential to overcome the effect of single charge over longer distances λ_D. At distances larger than the Debye length is measured only the collective effects, not those of individual charges. In the case of a plasma in which the mobile charge are primarily electrons, the Debye Length is:

$$\lambda_D = 7430\sqrt{\frac{kT}{n_e(m^{-3})}} \tag{1.1.5}$$

where n_e is the electron density. For example in a plasma with electron density of 10^{24} e/m^3 and $kT = 50\ eV$ we have a length of about 52 nm.

In Fig.1.3 is shown the comparison between the performance of the Coulomb potential (curve dashed line) and the screened potential [1].

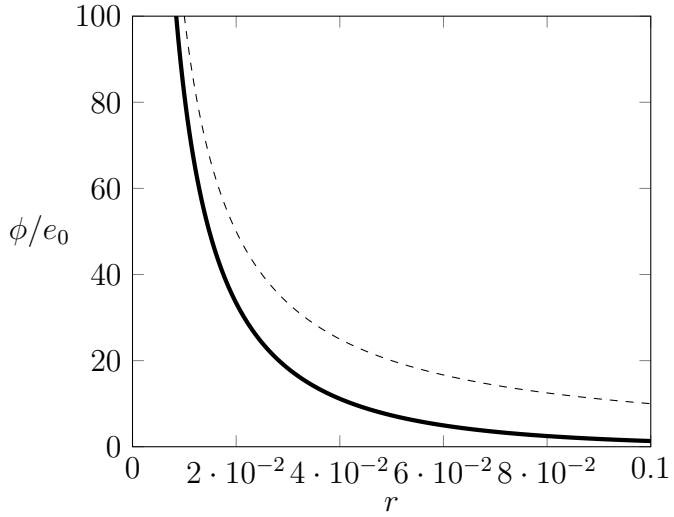

Figure 1.3: *Comparison between the Coulomb potential and screened potential for a* $\lambda_D = 0.07m$*, typical value of Sun's corona*

1.1.5 Plasma frequency

The study of the system after a little pertubation to its neutrality can provide some information on the characteristic reaction time. In the plasma we consider the ions velocity neglected respect the electron movement, because the masses are very differents, if we change the position of an electron for a distance $\mathbf{d}$, after this displacement take place an electric field $\mathbf{E}$ egual to:

$$\mathbf{E} = \frac{n_e e \mathbf{d}}{\epsilon_0} \tag{1.1.6}$$

where ϵ_0 is dielectric constant of vacuum and e the charge of electron. Thanks to this electric field, the electron came back in the original position of equilibrium, with a force $-e\mathbf{E}$, from this the motion equation for electrons are:

$$m_e \ddot{\mathbf{d}} = -e\mathbf{E} = -\frac{n_e e^2 \mathbf{d}}{\epsilon_0} \tag{1.1.7}$$

$$\implies \ddot{\mathbf{d}} + \frac{n_e e^2 \mathbf{d}}{m_e \epsilon_0} = 0 \tag{1.1.8}$$

with m_e the mass of electron. This equation rapresents the equation of harmonic oscillator with frequency:

$$\omega_{pe} = \sqrt{\frac{n_e e^2}{m_e \epsilon_0}} \tag{1.1.9}$$

this is know as plasma frequency for electrons, that in a case with a $n_e = 10^{24}\ e/m^3$ is equal to 56.4 THz. There is the same expression for ions:

$$\omega_{pi} = \sqrt{\frac{n_i Z^2 e^2}{m_i \epsilon_0}} \tag{1.1.10}$$

with Z the average charge state, n_i the ion density and m_i the mass of ion. When the movement of ions is not negligible, there is a frequency of oscillation:

$$\omega_p = \sqrt{\omega_{pe}^2 + \omega_{pi}^2} \tag{1.1.11}$$

this is called *plasma frequency*, then the characteristic time of separation of charges in the plasma is:

$$\tau_p \approx \frac{1}{\omega_p} \tag{1.1.12}$$

Critical plasma frequency

From the electron plasma frequency depend the index of refraction of plasma and its optic propertiers. The relation between plasma frequency and refraction index n is:

$$n = \sqrt{\left(1 - \frac{\omega_{pe}}{\omega}\right)} = \sqrt{\left(1 - \frac{n_e}{n_c}\right)} \tag{1.1.13}$$

where ω is the frequency of incident electromagnetic wave and n_c is the critical density [5]:

$$n_c \propto n_e \omega \tag{1.1.14}$$

If the critical density is exceeded, the plasma is called over-dense. We can also obtained the relation

$$\omega > \ \omega_p \tag{1.1.15}$$

because n cannot be negative, and from this we are able to said the laser inside plasma can propagate onoy if there is this condition.

1.1.6 Collision phenomena

Collisions between charged particles in a plasma are totally different from the interactions among molecules in a neutral gas because of the long range of the Coulomb force. It is possible to study the binary collision by defining a collision frequency, that measures tha rate at which the particles are scattered. There are different frequencies that characterize the collisions betwenn electron-electron, ion-ion and ion-electron [6].

$$\nu_{ee} \propto n_e (kT_e)^{-3/2} ln\Lambda_{ee} \tag{1.1.16}$$

$$\nu_{ii} \propto n_i Z^4 (kT_i)^{-3/2} ln\Lambda_{ii} \tag{1.1.17}$$

for the ion-electron interaction we must considerate the case in which the bullet is the electron

$$\nu_{ei} \propto Z n_e (kT_e)^{-3/2} ln\Lambda_{ei} \tag{1.1.18}$$

this is the major contribute of collisions inside of plasma. $\ln\Lambda$ is a parameter called Coulomb logarithm:

$$ln\Lambda = 8.33 - 0.5ln(n) + 1.5ln(T) \tag{1.1.19}$$

1.1.7 Distribution function

A distribution function can describe the motion of charged particles inside a plasma very well. When all particles of plasma are in thermal equilibrium it is possible to use a Maxwellian distribution [7]. A velocity function distribution $f(v)$ describes the number of particles in a given velocity interval, $dn = f(v)dv = f(v_x, v_y, v_z)dv_x dv_y dv_z$. In the case of thermal equilibrium the distribution is a Maxwellian:

$$f(v_x, v_y, v_z) = \left(\frac{m}{2\pi kT}\right)^{3/2} e^{-\frac{m(v_x^2 + v_y^2 + v_z^2)}{2kT}} \tag{1.1.20}$$

where m is the particle mass and v_i is 1-dimensional velocity. From this it is possible to obtain the distribution of speed and energy:

$$F(v) = 4\pi\ v^2 f(v) = 4\pi\ v^2 \left(\frac{m}{2\pi kT}\right)^{3/2} e^{-\frac{mv^2}{2kT}} \tag{1.1.21}$$

$$F(E) = F(v)\frac{dv}{dE} = \left(\frac{4}{\pi}\right)^{1/2}(kT)^{-3/2}E^{1/2}e^{-E/kT} \tag{1.1.22}$$

from these distributions it is possible to have information about the mean particle velocity and energy

$$\bar{v} = \sqrt{\frac{8kT}{\pi m}} \tag{1.1.23}$$

$$\bar{E} = \frac{3}{2}kT \tag{1.1.24}$$

$\bar{v}$ is the thermal velocity that in the case of proton in plasma with temperature of about 10^4 K is about $1.45 \cdot 10^4$ m/s.

1.2 Non equilibrium plasma

In the previous section, was discussed about the properties of the plasma in the case of Local Thermodynamics Equilibrium (LTE). But exists in a wide variety of astrophysical and laboratory plasmas that are in Non Local Thermodynamic equilibrium (NLTE). In laboratory, NLTE plasmas exists in laser produced plasmas based experiments.

1.2.1 Plasma production by laser

One of the most important characteristics of the laser is its ability to release an incredible amount of energy in times of the order of nanoseconds or much lower. This energy allows to develop a series of experiments as a function of the laser-intensity used. For low intensity laser it is possible to study the optical properties of materials like: trasmission, reflection, absorption, ecc. If we use high intensity laser, in the order of 10^{10} W/cm^2, for hit a solid target, it produce an effect called Pulsed Laser Ablation referred to as a process where laser produce a plume that moves away from the target and expands along three dimension but principally along the normal direction to the target [8],[9], [10]. This plume is called *non equilibrium plasma* and has different features than other kind of plasma. The plasma produced by laser is used in many fields in Physics and in Engineering research,

for welding, cutting, production and modification of surface, nanoparticles production and Laser Ion Source (LIS) [11], [12], [13], [14].

1.2.2 Ablation Threshold models

It was said that experiments involving laser ablation are performed at high laser intensity. This is because the ablation is a threshold process, below a given fluence value there is not a sufficient transfer of energy to the target that allows the removal of material [15]. This threshold value depends on both the characteristics of the laser, such as the wavelength, both the properties of the material, as we will see in the theoretical models for the calculation of the threshold.

Photothermal model

If the energy of photons are below the ionization energy, the ablation process is due to the interaction of the laser and the subsequent oscillation of the electrons, after the electrons are thermalized, they heat the lattice of the material causing the ablation process. According to the photothermal models the threshold is the density of energy enough to evaporate the target in vacuum a mass radiated of a target [16]. Then the threshold is:

$$F_{theor} = \frac{E_{heat} + E_{fus} + E_{subl}}{S} = \frac{V\rho}{S}\frac{c_s\Delta T + \lambda_f + \lambda_e}{1-R} \tag{1.2.1}$$

E_{heat}, E_{fus} and E_{subl} are the thermal, fusion and evaporation energies, while S is the laser spot, V and ρ are volume and density of ablated mass, c_s the specific heat, ΔT the increment of temperature, R the reflectivity of target and λ_f and λ_e the latent heats for fusion and evaporitation. The mass is bounded by the laser spot S and penetration length which depends on the absorption length of the light δ and by the thermal diffusion length $L = \sqrt{D\tau}$ where τ is pulse duration and D diffusion coefficient. Considering the Volume V like a cone:

$$V = \frac{S}{3}(\delta + L) = \frac{S}{3}\left(\sqrt{\frac{2}{\omega\mu_0\sigma}} + \sqrt{\frac{K}{\rho c_s}\tau}\right) \tag{1.2.2}$$

where ω is the radiation frequency, μ_0 the magnetic permeability in vacuum, σ the electrical conductivity, K the thermal conductivity.

Photochemical model

If we consider a laser, with photon energy $h\nu$ higher of chemical energy bonds, and the density of absorbed photons, n_{phot}, is bigger of atomic density of target, n_{at}, the Energy E absorbed in a volume V can be write:

$$\frac{E}{V} = h\nu n_{phot} \geq h\nu n_{at} \tag{1.2.3}$$

the minimum of flux is:

$$F_{thr} = \left(\frac{E}{S}\right)_{min} = \frac{h\nu n_{at}}{\alpha} \tag{1.2.4}$$

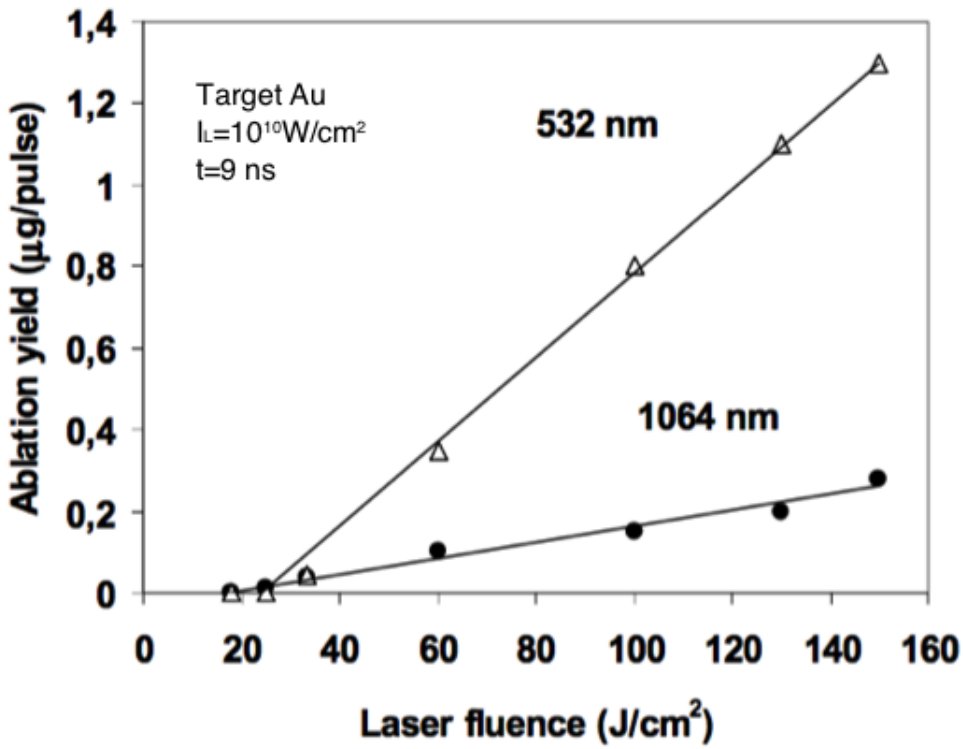

Figure 1.4: *Ablation yield of gold vs. laser fluence*

In Fig.1.4 we can observe experimental values of ablation yield as a function of laser fluence, perform with a Q–switched Nd:Yag laser, 1 064 nm and 532 nm wavelengths for the fundamental and second harmonics, respectively, 9ns pulse duration and 900mJ maximum pulse energy, interacting with a gold target in vacuum[17]. The ablation yield was calculated after the using a surface profilometer for measurement of craters profiles were performed with a surface profiler. The shape and the dimension of the crater permit to calculate the total number of atoms removed by the ablation process and to evaluate the ablation yield as a function of the laser fluence.

1.3 Laser-plasma interaction

In the plasma formed by laser ablation are produced very high electric fields and there are effects that produce acceleration of ions and electrons. This study became very important in last decades because it is possible to use femtosecond (or attosecond) laser that can to reach intensity of about 10^{20} W/cm^2 and these system could use like accelerator of every type of ions over several tens of MeV for nucleon [18]. For a better understanding of these accelerations it is important to study the phenomena of absorption of the laser light in the plasma.

1.3.1 Inverse Bremsstrahlung

When the laser intensity is very high the non linear phenomena are very important. An absorption process that take place thanks to the collisions inside the plasma is the *Inverse Bremsstrahlung*. The laser induces an oscillator movement on the electrons that have velocity v:

$$v = \frac{eE_L}{m_e\omega} \tag{1.3.1}$$

where ω in the angular frequency of laser radiation, E_L the amplitude of electric field and I_L its intensity, m_e and e the electron mass and charge respectively. The electrons, while oscillating under the action of the laser electric field, collide with the ions giving rise to

transfer of electromagnetic energy to the plasma. The fraction of absorbed laser energy after a propagation over a distance L in a uniform plasma is given by:

$$\alpha_{abs} = 1 - e^{-k_{ib}L} \tag{1.3.2}$$

where

$$k_{ib} = 3.1 \cdot 10^{-7} Z n_e^2 \ln \Lambda \omega^2 \left[1 - \left(\frac{\omega_p}{\omega}\right)^2\right]^{-1/2} (kT)^{-3/2} cm^{-1} \tag{1.3.3}$$

is the inverse bremsstrahlung coefficient [5]. It is clear from equation that collisional absorption is higher for lower temperatures, higher densities, higher Z plasmas.

1.3.2 Ponderomotive force

Electrons are much less massive than ions, so they response is more strongly than the ions to the electromagnetic fields of laser beam. The equation of motion for a single electron in an electromagnetic wave of frequency ω and wave number k travelling in the x-direction with an electric field of amplitude E_L in the y-direction and magnetic field B_L in the z-direction is

$$\frac{dv_y}{dt} = \frac{eE_L}{m_e} \cos(\omega t - kx) \tag{1.3.4}$$

$$\frac{dv_x}{dt} = v_y \frac{eB_L}{m_e} \cos(\omega t - kx) \tag{1.3.5}$$

Although the fields are oscillatory, they can exert a time-averaged force on electrons. The force is easily to calculate under the condition of low intensity and slow variation. The Electric field are considerate a small parameter and is possible to calculate the ponderomotive force like an expansion. The first order in an expansion, the electron responds only to the laser electric field. The electron equation of motion then reduces to:

$$\frac{dv_y}{dt} = \frac{eE_L}{m_e} \cos(\omega t - kx_0) \tag{1.3.6}$$

where x_0 is the rest position of elecron, integration gives:

$$v_y = v_{osc} \sin(\omega t - kx_0) \tag{1.3.7}$$

$$y = -\frac{v_{osc}}{\omega}\cos(\omega t - kx_0) \tag{1.3.8}$$

with:

$$v_{osc} = \frac{eE_L}{m_e\omega} \tag{1.3.9}$$

is the oscillation velocity of electrons, the *quiver velocity*. Then at this order, the electrons oscillates about its rest position and isn't subject to a time-averaged force. At the second order begin to be important the inhomogeneity of wave, the simplest form of inhomogeneity is a variation in amplitude in y-direction, the electric field direction. When the second order term is included, the y-component of the momentum becomes:

$$\frac{dv_y}{dt} = \frac{e}{m}\left(E_L + y\frac{dE_L}{dy}\right)\cos(\omega t - kx_0) \tag{1.3.10}$$

substituting 1.3.8 gives:

$$\frac{dv_y}{dt} = \frac{eE_L}{m}\cos(\omega t - kx_0) - \frac{v_{osc}}{\omega}\frac{e}{m}\frac{dE_L}{dy}\cos^2(\omega t - kx_0) \tag{1.3.11}$$

The first term on the right-hand side is the first order term which time-averages to zero, but the second order term can be rewritten as:

$$-\frac{1}{2}\left(\frac{e}{m_e\omega}\right)^2\frac{d(E_L^2/2)}{dy} \tag{1.3.12}$$

the force per unit volume acting on the electrons, and therefore on the plasma, is:

$$F = n_e m_e\frac{dv_y}{dt} = -\frac{1}{2}\left(\frac{\omega_p}{\omega}\right)^2\frac{d(\epsilon_0 E_L^2/2)}{dy} = -\frac{1}{2}\frac{n_e}{n_c}\frac{dU_e}{dy} \tag{1.3.13}$$

where U_e is the maximum energy density of the wave electric field

$$U_e = \frac{1}{2}\varepsilon_0 E_L^2 \tag{1.3.14}$$

If the wave was inhomogeneus in the x or z direction, the ponderomotive force has to be calculated in a different way since it originates with the $\mathbf{v}\times\mathbf{B}$ force. The response is the same, except that d/dy is replaced by d/dx or d/dz as appropriate. Consequently a general expression can be written down for the ponderomotive force [19]:

$$F = -\frac{1}{2}\frac{n_e}{n_c}\nabla U_e = -\frac{1}{4}n_e m_e\nabla v_{osc}^2 \tag{1.3.15}$$

We can make a simple calculation of the ponderomotive force in case of Nd:YAg laser pulse with intensity of 10^{12} W/cm^2 and time per pulse of 3 ns. In this case we can calculate the electric field of radiation in vacuum (impedence of vacuum $Z_0 = 377\ \Omega$):

$$E_L = \sqrt{I \cdot Z_0} = 1.9 \cdot 10^9 V/m \tag{1.3.16}$$

the frequency is:

$$\omega = \frac{2\pi c}{\lambda} = 1.76 \cdot 10^{15} rad/s \tag{1.3.17}$$

and the oscillation velocity of electrons:

$$v_{osc} = \frac{eE_L}{m_e \omega} \approx 2 \cdot 10^{15} m/s \tag{1.3.18}$$

Now if we use the previous equation

$$F = n_e m_e \frac{dv_{osc}}{dt} \tag{1.3.19}$$

and remember the quantity, $n_e = 10^{28}$ e/m^3 free electron density in metals, $m_e = 9 \cdot 10^{-31}$ kg rest mass of electron, it is possible to calculate the force.

$$F = n_e m_e \frac{dv_{osc}}{dt} = 10^{28} m^{-3} \cdot 9 \cdot 10^{-31} kg \cdot \frac{2 \cdot 10^{15} m/s}{3 \cdot 10^{-9} s} = 6 \cdot 10^{11} N \tag{1.3.20}$$

1.4 Plasma Expansion

1.4.1 Coulomb–Boltzmann-Shifted distribution

Due to the high electric field driven by intense laser pulses, the ponderomotive forces are responsible for the electron acceleration up to relativistic velocities. The different spatial and temporal charge distributions of electrons and ions in the non-equilibrium plasma generate high electric fields driving ion acceleration that occurs mainly along the normal to the target surface. Plasma emits high photons intensity, from visible to UV and X- ray regions, electrons, from relativistic (hot electrons) to low energetic ones (cold electrons) and ions at different charge state, energy distribution and angular distribution.

The laser-plasma absorption depends on many factors subjected to the laser properties (pulse energy and duration, wavelength, polarization, etc.), irradiation conditions (focal dimension, focal distance from the target surface, incidence angle, etc.) and target composition and geometry. Increasing the $I\lambda^2$ factor, being I the laser intensity and λ the laser wavelength, the laser absorption processes in plasma increase. Such factor enhances the plasma temperature and density, the maximum ion charge state, the kinetic energy of the electrons and ions and the electric field driving the ion acceleration. Depending on the laser intensity, such electric field can assume values from the order of 10^3 V/m up to 10^{10} V/m for laser intensities coming from about 10^{10} W/cm^2 delivered by ns laptop lasers up to about 10^{20} W/cm^2, delivered by fs lasers, respectively. While at low laser intensity the kinetic energy of the ions is mainly due to thermal interactions, at high laser intensity it more and more depends on the Coulomb interaction in the non-equilibrium plasma. The kinetic energy of emitted ions generally follows a Boltzmann distribution which is different for each charge state and is characterized, especially at high intensity, by a cut-off value at the maximum electric field of acceleration. Experimental measurements of ion energy distributions demonstrated that the energy distributions are regularly shifted in energy, exhibit a width depending on the plasma temperature and have an intensity distribution correlated to the multiple ionization cross section of the ion species. Assuming the main accelerations due to thermal and Coulomb interactions, the ion emission occurring along the normal to the target surface follows the Coulomb–Boltzmann-Shifted (CBS) function (introducing by Torrisi L. 2016)[20]:

$$f(v) = A\left(\frac{m}{2\pi kT}\right)^{3/2} v^3 e^{-[(m/2kT)(v_T - v_k - v_c)^2]} \tag{1.4.1}$$

where A is a constant of normalization, m the ion mass, kT the plasma temperature, v_k the adiabatic plasma expansion in vacuum velocity and v_c the Coulomb velocity. The total ion velocity along the normal direction to the target surface has three components:

- the first is the thermal velocity

$$v_T = \sqrt{\frac{3kT}{m}} \tag{1.4.2}$$

- The second is the adiabatic plasma expansion velocity

$$v_k = \sqrt{\frac{\gamma kT}{m}} \tag{1.4.3}$$

  where γ is the adiabatic coefficient.

- The third component is the Coulomb velocity

$$v_c = \sqrt{\frac{2zeV_0}{m}} \tag{1.4.4}$$

  where Z is the ion charge state, e the electron charge, and V_0 the potential applied to the acceleration distance producing the electric field driving the ion acceleration.

If we consider proton distribution with $T = 10^4\ K$ and a potential of $V_0 = 100\ V$ we can observe that v_th and v_k are very similar, $v_th = 1.5 \cdot 10^4\ m/s$ and $v_k = 1.15 \cdot 10^4\ m/s$, but v_c is higher, $v_c = 1.38 \cdot 10^5\ m/s$. This is an important result because the potential V_0 increase with the laser intensity then is the more important contribution in the final energy of particles.

1.5 Laser Ion Acceleration

It is now clear from the above that high-intensity lasers have the ability to accelerate ions to energies that depend on the intensity of the laser (as well as other parameters). In recent years the study of acceleration regimes has acquired an important role in laser-matter interaction research. Accelerators are essential for science and society, they are in use in high energy physics, nuclear physics and life science. They are important to industry, the development of new materials, energy and can be applied in many other fields. For understand the importance of accelerators it is enough to think that the beam particles produced from they is usefull for medical treatments in hospitals and the very important role in the experiment for understand the nature of our universe (for example the Higgs boson discovery at the LHC facility). Three main regimes of high intensity laser–matter interaction can be employed. The first concerns the laser interacting with

bulk targets, resulting in Backward Plasma Acceleration (BPA)[21]-[22], which has the advantage of producing high ion emission and high currents by using laser pulses in repetittion rate mode. The second regime, occurring at intensities above 10^{15} W/cm^2, known as the Target Normal Sheath Acceleration (TNSA)[23]-[22] , the third regime is known as Radiation Pressure Acceleration (RPA) [24] regime and shows very high ion acceleration, above $10MeV/charge\ state$ for laser intensity above 10^{19} W/cm^2 . The most effective mechanism for coupling laser energy to ions is predicted to be RPA, for which the momentum of the laser is efficiently imparted to the ions.

1.5.1 Backward Plasma Acceleration

Ions produced in this regime have low kinetic energies, generally below 1 $MeV/charge\ state$, it is of special interest in laser ion source applications and high ion emission yields. When laser interacts with thick target, the first particles that come out from the target are electrons, this produce a negative charge cloud out of the target and a positive on the surface, between these two there is a distance comparable with Debye length and the electrical field is very high and acts like accelerator field.

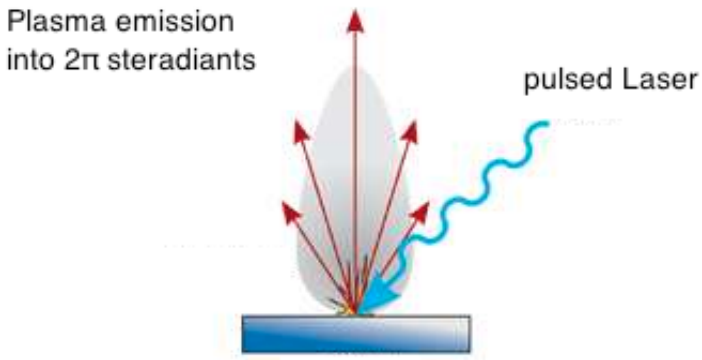

Figure 1.5: *Representation of BPA regime of acceleration*

The accelerator electric field is with a good approximation:

$$E \approx \frac{V_0}{\lambda_D} \tag{1.5.1}$$

where V_0 is the electric potential that take place between the electric clouds. These fields generally are in the range of 10^{6-9} V/m generating ions energy below $MeV/charge\ state$. In Fig.1.5 is shown BPA phenomena, produced plasma travel along the normal direction with an angular aperture, with emission of ions, electrons and photons.

1.5.2 Target Normal Sheath Acceleration

This regime has the advantage that it allows to accelerate ions with kinetic energies above 1 $MeV/charge\ state$. In this case a high electric field is generated at the rear side of a thin irradiated target, due to relativistic electrons escaping from the target and to resulting Coulomb explosion of the target. The electric field drives the ion acceleration in forward direction along the normal to the target surface. In the TNSA regime the electric field driving ion acceleration from the rear side of the target is given by the formula [22]:

$$E_{TNSA} = \sqrt{\frac{kTn_e(0)}{\varepsilon_0}} \tag{1.5.2}$$

where kT is the electron temperature, $n_e(0)$ is the electron density on the surface of target and ε_0 is the electric permittivity of the vacuum. Also in this case we can consider the case of $T = 10^4$ k and $n_e = 10^24$ m^{-3} for the calculation of $E_{TNSA} = 1.24 \cdot 10^8$ V/m. When thin targets are used, the ion acceleration in the forward direction is increased, but the ion yield decreases due to the low quantity of matter present.

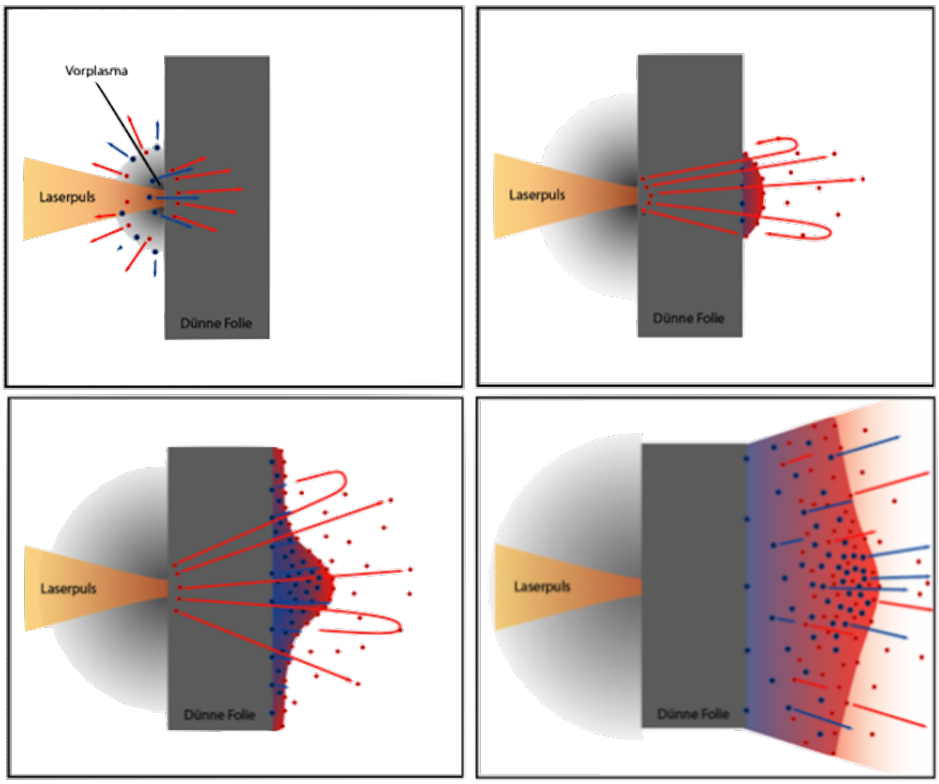

Figure 1.6: *Representation of TNSA regime of acceleration*

In Fig.1.6 is shown the scheme of TNSA regime, the laser irradiating the thin film surface produce an electron oscillation that allows the emission of electrons in forward direction, after, thanks to the Coulomb Explosion, the accelerated ions follow the electrons in forward direction.

1.5.3 Hole-Boring Radiation Pressure Acceleration

The radiation pressure acceleration mechanism is based on the effects equivalent to radiation pressure. The radiation pressure for perfect reflection is proportional to the laser intensity

$$P_L = 2\frac{I_L}{c} \tag{1.5.3}$$

Where I_L is the laser intensity and c is the light speed. For laser of intensity 10^{10} W/cm^2 the pressure is about 0.66 Pa but if we use laser with very high intensity like 10^{18} W/cm^2 or 10^{20} W/cm^2, we obtaine pressures of 6 MPa or 6 GPa. Similar pressure can be applied to a thin foil, upon whose surface plasma quickly forms. The radiation pressure effect is transmitted into the plasma by electrons via ponderomotive force. Displaced electrons produce space charge that creates a steady pressure, which in its turn transfers the effect to the ions. Two versions of radiation pressure mechanisms have received distinct names, the *hole-boring* and *light-sail* mechanism. In the case of hole-boring, that take place with less thin target, the space charge due to electrons acts on ions that are pushed into the overdense plasma, initially compressing the foils and the pushing a region of the foil forward. The velocity of ions can be estimated as [25]:

$$v = \sqrt{\frac{I_L}{\rho c}} \tag{1.5.4}$$

where ρ is the target density. The most attractive feature of the Hole-Boring is that the resulting protons beam is the near monochromatic peak at maximum energy.

1.5.4 Light-sail Radiation Pressur Acceleration

In this regime, when the laser interact with very ultra thin target, the radiation pressure mechanism is taken to the extreme when the foils is so light that its starts to accelerate immediatly as a whole. In this model the velocity of ions can be estimated as [25]:

$$v = \frac{2I_L\tau}{\eta c} \tag{1.5.5}$$

where τ is the pulse duration, η is the areal density that interact with laser,$\eta = \rho d$, where d is the target thickness. As we can see the energy scaling in the light-sail regime is more favorable than in the hole-boring case, the velocity of ions is proportional to I_L and the energy is thus proportional to I_L^2. However this mechanism cannot be completely decoupled from the competing TNSA mechanism. Now we can make an example in which we consider only the contribution of radiation pressure following the equation 1.5.5. We

consider two laser intensities interacting with Al target of 10 nm in thickness, the first one has an intensity of $10^{10} W/cm^2$ with 3 ns of time per pulse, and the second an intensity of $10^{20} W/cm^2$ with 30 fs of time per pulse. Calculating the velocities we obtain:

$$10^{10} W/cm^2 \rightarrow v = \frac{2I_L\tau}{\eta c} = 74 m/s \tag{1.5.6}$$

$$10^{20} W/cm^2 \rightarrow v = \frac{2I_L\tau}{\eta c} = 7.4 \cdot 10^6 m/s \tag{1.5.7}$$

Chapter 2

Plasma diagnostics

Different diagnostics can be used to study the plasma properties and the radiation emitted from the plasma. On line diagnostics use time-of-flight (TOF) techniques to measure the ion velocity and to calculate the mean ion kinetic energy. Ion collectors and SiC detectors, connected to a fast storage oscilloscope, are employed to measure the maximum and mean ion energy: first of them give a signal proportional to the ion charge state and the second of them give a signal proportional to the ion energy deposited in the semiconductor depletion layer. Off line diagnostics use track detectors (CR-39, Gaf chromic,..), surface profilometer and other techniques to obtain the information on the properties of the produced plasma.

2.1 Plasma diagnostics on-line

2.1.1 Ion Collectors

The most common type of probes are plane collectors or Faraday cups (with one or two grids) for ion and electron component separation. The separation usually is done by means of a static electric field that exists between either the grounded entrance grid and the biased (negative) collector or the grounded entrance grid and the biased (negative) control grid. The ion current is collected by a collector; but once it is reached, it causes a secondary ion-electron emission that affects the ion current measurement. The ion

current density, i_i, of ions reaching the collector in the absence of the secondary ion-electron emission and shielding grids is:

$$i_i = en_e v = ev \sum_{j=0}^{z_{max}} z_j n_{i,j} \tag{2.1.1}$$

where n_e is the electron density, j is the number of ion species, n_{ij} is the density of the j_{th} ion specie, v is the plasma velocity, and Z_j is the charge state of the j_{th} ion specie. In the case of a biased collector, the collector is shielded from the plasma by a space-charge layer. The latter can modify the collector current or alter the secondary ion-electron emission current. The threshold ion density for this effect is given approximately by [26]:

$$n_{iz} \leq 2.5 \cdot 10^8 \frac{E(KeV)}{(zd)^2} \tag{2.1.2}$$

where $E(keV)$ is the kinetic energy of ions with the charge state $z, d(cm)$ is the grid-collector spacing, and $n_{j,z}(cm^{-3})$ is the density of ions with the charge state z.

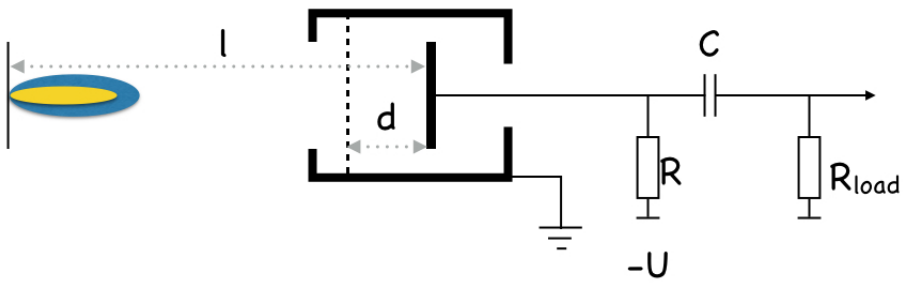

Figure 2.1: *Schematic drawing of a typical ion collector*

A scheme of an IC is shown in Fig.2.1 where it is possible to see the detector placed along the normal direction of propagation of plasma. There are also an electronic circuit of acquisition and a grid for the suppression of secondary charged particles. So the low energy ions are severely limited by the space charge. For example for a grid that is 2 cm from the collector that interacts with an ion beam of 1 keV energy with charge state of 10^+ has a threshold density:

$$n_{iz} \leq 2.5 \cdot 10^8 \frac{E(KeV)}{(zd)^2} = 2.5 \cdot 10^8 \frac{1KeV}{(10 \cdot 2cm)^2} = 6.25 \cdot 10^5 cm^{-3}$$

The same beam with energy 1 MeV instead:

$$n_{iz} \leq 2.5 \cdot 10^8 \frac{E(KeV)}{(zd)^2} = 2.5 \cdot 10^8 \frac{1000KeV}{(10 \cdot 2cm)^2} = 6.25 \cdot 10^8 cm^{-3}$$

The output current in the collector circuit, I_c, is a combination of ion current, i_i, and secondary electron current, I_e [26]:

$$I_c = I_i + I_e = e\varepsilon v S \left\{ \sum_{j=0}^{z_{max}} \left[z_j(t) + \gamma_j(t) \right] n_{i,j}(t) \right\} \tag{2.1.3}$$

where ε is the transparency of the entrance grid, S is the area of the collector, γ_j, z_j, and $n_{i,j}$ are the secondary ion-electron emission coefficient, the charge state, and the density of the j_{th} ion specie (j = 0 corresponds to neutral particles), respectively. Taking into account that:

$$n_i = \sum n_{i,j} \tag{2.1.4}$$

we obtain from equation

$$I_c(t) = \varepsilon e v S \bar{z}(t) n_i(t) \left[1 + \frac{\bar{\gamma}(t)}{\bar{z}(t)} \right] = \varepsilon \left[1 + \frac{\bar{\gamma}(t)}{\bar{z}(t)} \right] I_{coll}(t) \tag{2.1.5}$$

where:

$$\bar{\gamma} = \frac{\sum_j \gamma_j n_{i,j}}{\sum_j n_{i,j}} \quad and \quad \bar{z} = \frac{\sum_j z_j n_{i,j}}{\sum_j n_{i,j}}$$

are the average secondary ion-electron emission coefficient and the average charge state of ions, respectively, and I_{coll} is the ion current in the entrance grid for a given moment t. Thus,

$$I_{coll}(t) = \frac{U_c(t)}{\left\{ \varepsilon R_{load} \left[1 + \frac{\bar{\gamma}(t)}{\bar{z}(t)} \right] \right\}} \tag{2.1.6}$$

where $U_c(t)$ is the voltage amplitude of the collector signal, $N(t)$ is the number of ions reaching the charge collector, and R_{load} is the load resistance. Moreover it is possible to calculate the mean velocity and energy by the following equations:

$$\bar{v} = \frac{l}{\bar{t}}; \qquad \bar{E} = \frac{1}{2} m \bar{v}^2 \tag{2.1.7}$$

where l is the target-collector distance and $\bar{t}$ can be expressed as:

$$\bar{t} = \frac{\int_0^\infty f(t)tdt}{\int_0^\infty f(t)dt}; \qquad f(t) = \frac{U_c(t)}{1 + \frac{\bar{\gamma}(t)}{\bar{z}(t)}} \tag{2.1.8}$$

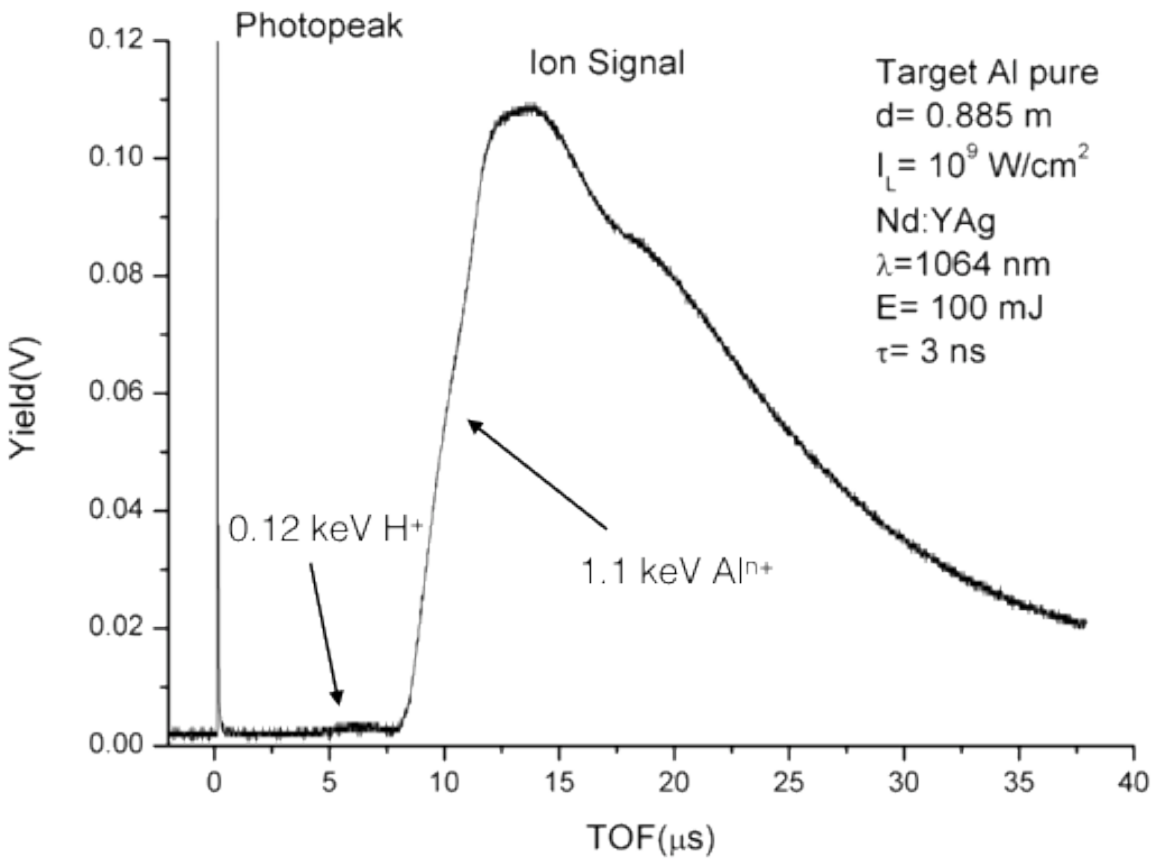

Figure 2.2: *Typical IC spectra of Al target irradiated in vacuum with laser intensity of* $10^9 W/cm^2$

A typical IC spectrum is reported in Fig.2.2. It was obtained by irradiating in vacuum an Al target with a Nd:YAG laser at plasma laser laboratory of University of Messina, with a laser intensity of $10^9 W/cm^2$. The collector applied bias is $-50V$, the detection angle is $0°$ and the detection distance is $88.5cm$. The first narrow signal is the photo-peak due

to the UV and X-rays emission from the plasma. It represents our start signal. In this example we have:

$$H^+ \rightarrow v = \frac{0.885m}{6\mu s} \rightarrow E(H^+) = 0.120keV$$

$$Al^{n+} \rightarrow v = \frac{0.885m}{10\mu s} \rightarrow E(Al^{n+}) = 1.10keV$$

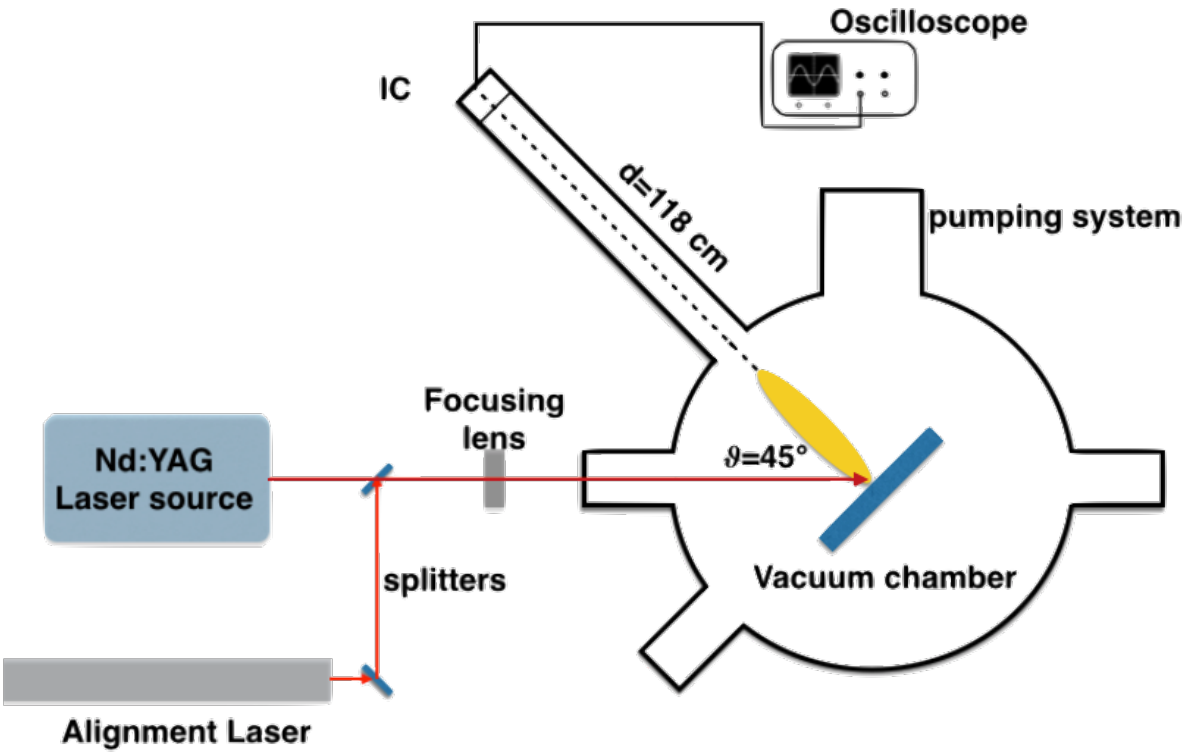

Figure 2.3: *Schematic drawing of TOF setup in Plasma laboratory in Messina University.*

In Messina the experimental setup used for Time of Flight measures is reported in Fig.2.3. The target-detector distance is variable and we can choise the better configuration for each experiment. Greater flight distance allows a better separation of the states of charge present in the plasma due to the different energy instead a shorter distance allows to increase the yield of revelation but not to separate the charge states.

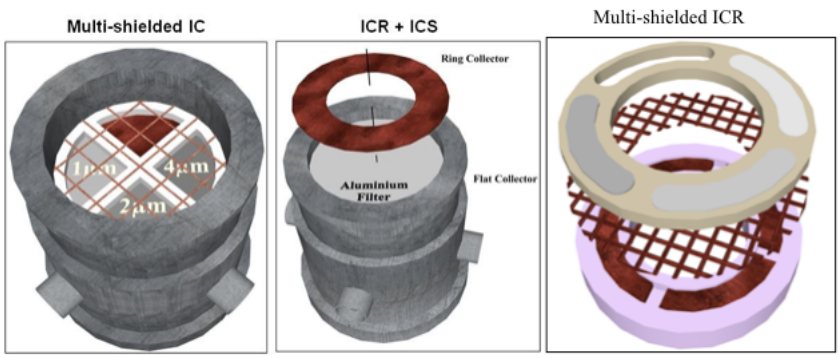

Figure 2.4: *Schematic drawing of ion collectors with filter.*

To improve the detection of certain ions within the plasma is possible to insert the absorbers in front the detector in such a way that, for example, the heavy particles are stopped and improves the visualization of protons, it is also possible to insert different types of absorbers in order to study the change of the signals with the thickness. This kind of detector is shown in Fig.2.4.

2.1.2 Silicon Carbide detectors

It is possible to use different type of detector in time og flight configuration. In the last ten years, silicon carbide (SiC) has gained remarkable and increasing attention as wide bandgap semiconductor for developing electron devices. In particular, SiC has interesting properties for manufacturing detectors of ionizing radiation (alpha, electrons, protons, ions, X and gamma rays). The wide band gap (3.2 eV) allows to realize Schottky junctions with high barrier height (> 1.5 eV) and implies completely negligible thermally generated current. This brings to detectors with extremely low leakage current densities – on the order of 1 pA/mm^2 at room temperature – more than two orders of magnitude lower than those of other semiconductor detectors. Such low leakage current makes SiC detectors ultra low noise even at high operating temperature. Due to the wide bandgap SiC detectors are also blind to visible-light, an advantage in some applications [27].

Table 2.1: *Principal properties at room temperature of SiC compared to other semiconductors/insulators interesting for radiation detection*

Property	4H-SiC	3C-SiC	6H-SiC	Si	GaAs	Diamond
Crystal structure	Hexagonal	Zinc-blende	Hexagonal	Diamond	Zinc-blende	Diamond
Band structure	Indirect	Indirect	Indirect	Indirect	Direct	Indirect
Energy gap E_g (eV)	3,26	2,20	2,86-3,03	1,12	1,43	5,45
Electron mobility $\mu_g(cm^2/Vs)$	800-1000	1000	370-600	1400-1500	8500	1800-2000
Hole mobility $\mu_g(cm^2/Vs)$	100-115	50	50	450-600	400	1200-1600
Breakdown electric field $E_c(MV/cm)$	2.2–4.0	1.2	2.4–3.8	0.2–0.3	0.3–0.6	10
Thermal conductivity τ_{th} $(W/cm°C)$	3,0-5,0	3,0-5,0	3,0-5,0	1,5	0,5	20
Saturation velocity v_s $(cm/s) \times 10^7$	0,8-2,2	2,0-2,7	2,0	0,8-1,0	1,0-2,0	2,2-2,7
Relative dielectric constant ε_r	9,7	9,7	9,7	11,8	12,8	5,5
Max working temperature $(°C)$	1240	1240	1240	300	460	1100
Melting point $(°C)$	1800	1800	1800	1420	1240	3500
e-h pair energy (eV)	7,78			3,62	4,21	13
Hole lifetime $\tau_p(s)$	6×10^{-7}			$2,5 \times 10^{-7}$		10^{-9}
Density $\rho(g/cm^3)$	3,21	3,21	3,24	2,33	5,32	3,52
Physical stability	Excellent	Excellent	Excellent	Good	Fair	Very Good
Atomic weight	44	76	46	28	144,6	12
Lattice constant (Å)	a=3,07 c=10,05	4,36	a=3,07 c=15,12	5,43	5,65	3,567
Electron affinity (V)	3,08	3,83	3,34	4,07	4,07	-1,07

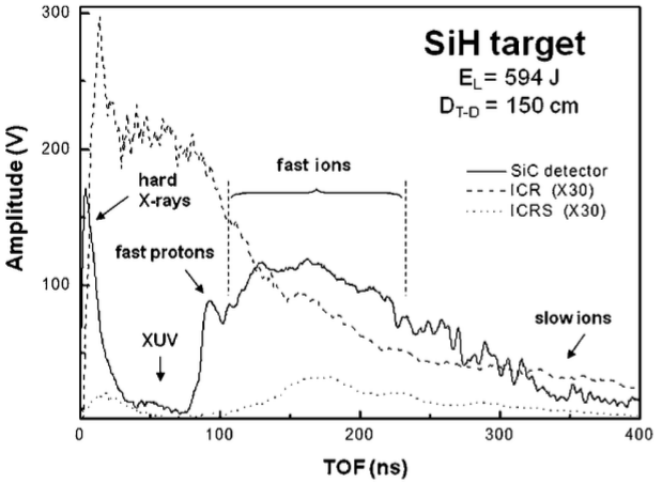

Figure 2.5: *TOF spectra detected by an unshielded ICR, the shielded one (ICRS), and the SiC detector. The spectrum is obtained using a SiH target and a laser energy of 594 J.*

Fig.2.5 was obtained using ICR, SiC and IC shielded detectors in the diagnostics of plasma produced by an hydrogen-enriched silicon target irradiated at a laser energy of 594 J [28]. The ICR spectrum (dashed line) shows a broad peak between 0 and 250 ns related to x-rays, UV radiation, and fast ions, followed by a broad structure with some peaks between 250 and 400 ns related to slow ions. The ICR resolution is very poor and it does not permit a good separation of the different ion contributions. To filter out the XUV component, a simple method based on the application of thin absorbers has been developed: a thin (2 μm) Al foil has been placed in front of the ion collector to absorb the heavy ions and to reduce the photon background. Both case with IC detector shown results that present some problems. With the IC shielded (ICRS) the signal is to small, and this is due to the presence of aluminium, of course the X-UV signals are reduced but also the ions signals. The SiC spectra instead shows very big signals for fast ions and hard x-ray but very low for X and UV ray thanks to energy gap of material. From SiC results we can calculate:

$$H^+ \rightarrow v = \frac{1.5m}{90ns} \rightarrow E(H^+) = 1.4MeV$$

$$Si^{n+} \rightarrow v = \frac{1.5m}{150ns} \rightarrow E(Si^{n+}) = 14MeV$$

SiC detectors appear very useful to the real-time monitoring of the laser-generated plasma due to their high response velocity, high sensitivity, and well proportionality to the ion energy. The main advantage with respect to ICR is the proportionality to the ion energy instead of the ion charge state. The utility of SiC like detector can be found also in the diagnostic of x-ray produced by plasma. For example in Fig.2.6 it is possible to observe experimental results of monitored xray produced by laser target interaction for several targets, using SiC detector [29].

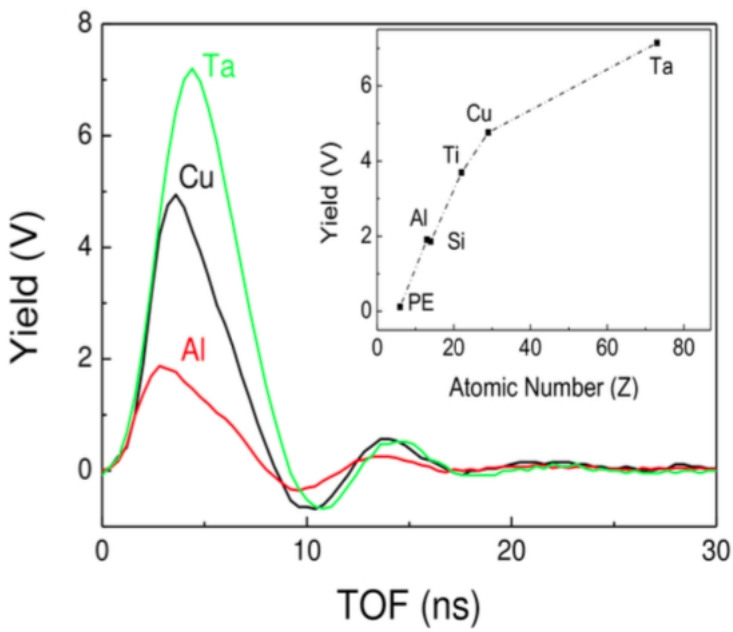

Figure 2.6: *SiC yield vs time for plasma generated Al, Cu and Ta target irradiated in the same experimental conditions. The insert reports the yield as a function of the atomic number of the target material*

From this experiment was clear that the efficiency of conversion of laser energy to hard X- rays is proportional to Z [30]. This dependence can be explained by an increase in the concentration of hot electrons generated in a plasma, which is proportional to $\sqrt{Z}$.

2.1.3 Mass Quadrupole Spectrometer

Mass quadrupole spectrometer (MQS) can be used to detect the gas particles ejected from the laser-generated plasma. A quadrupole mass spectrometer consists of an ionizer (bombardment by electrons from a hot filament) showed in Fig. 2.7, an ion accelerator, and a mass filter consisting of four parallel metal rods arranged as in the Fig.2.8.

Figure 2.7: *PrismaPlus ion sources for to ionize the gas*

The filter system of a quadrupole mass spectrometer consists of four parallel rods arranged in the form of a square [31]. Each pair of opposite rods in Fig.2.8, designated (+) or (-), is connected to each other. Between the two pairs of rods, an electrical voltage consisting of a DC portion U and an AC portion with amplitude V and frequency $f = \omega/2\pi$ applied:

$$U_{quad} = U + V\cos(\omega t) \tag{2.1.9}$$

Ions in a quadrupole field are focused by the rods [32]. The motion of the ions in the field is described by solutions to the Mathieu equation:

$$\frac{d^2u}{d\xi^2} + (a_u - 2q_u cos(2\xi))\, u = 0 \tag{2.1.10}$$

where u represents the x, y and z coordinates, ξ is a dimensionless parameter given by $\xi = \omega t/2$, and a_u, and q_u, are dimensionless trapping parameters. The parameter ω, is the radial frequency of the potential applied to the ring electrode.

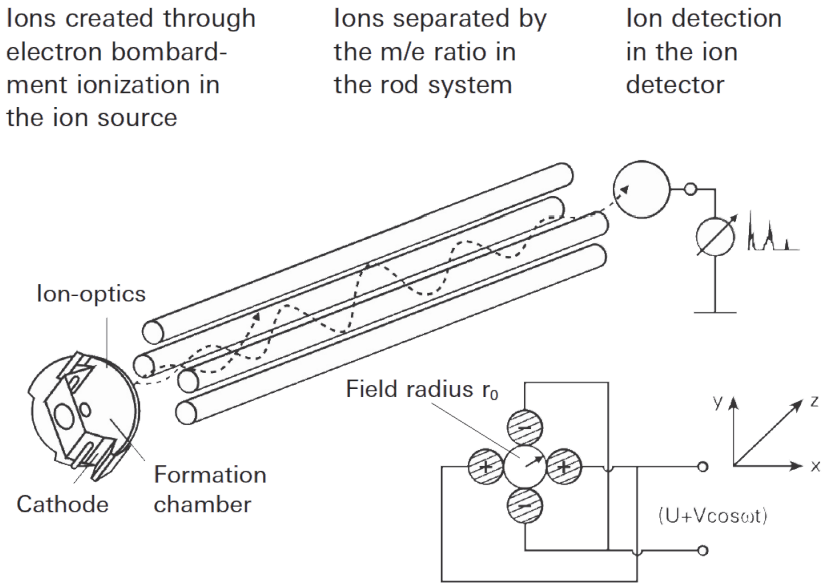

Figure 2.8: *Schema of Mass Quadrupole Spectrometer*

Solving this equation it is possible to obtain that:

$$a_u = \frac{8zeU}{m\omega^2 r_0^2} \tag{2.1.11}$$

and

$$q_u = \frac{8zeV}{m\omega^2 r_0^2} \tag{2.1.12}$$

where z is the charge state, e charge magnitude of electron, m the ion mass and r_0 is the distance from the rods to the center of propagation direction [31]. The selected m/z ratio depends by the voltage applied to the rods, in addition to geometrical parameters that are fixed during the experiment.

LAMQS measurements

The quadrupole operates by plotting the mass yield vs. the mass value or, by fixing the masses of interest, by plotting the masses vs. the irradiation time.

Laser Ablation coupled to Mass Quadrupole Spectrometry (LAMQS) is a techniques recently used for the deep profile and compositional analysis of different solid materials. Flexible laser conditions (pulse energy, wavelength, spot size, incidence angle, etc.) and relative speed of analysis are advantages of the method, which make this technique attractive for depth profile analysis, for cleaning and for non-disruptive surface analysis [33]. The energy of the laser pulses is deposited onto the analyzed surface to induce desorption and vaporization of the most superficial mono-layers of the sample material. The vapor is then ionized and analyzed in mass by a suitable quadrupole spectrometer. In Fig.2.9 and 2.10 are showed MQS spectra obtained irradiate Nuclepore polymer ($C_{15}O_3H_{14}$ and a molecular weight of 242) and Nuclepore containign Ag nanoparticles respectivelly.

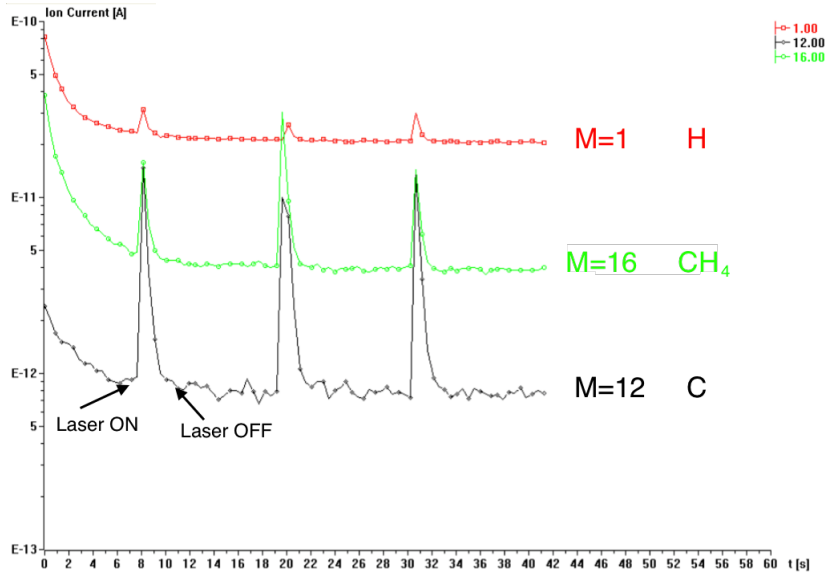

Figure 2.9: *Mass yield vs time of nuclepore polymer target irradiated at* 10^{10} W/cm^2*,in red dots is H particles, blacks C particles and green dots* CH_4*.*

Thanks to the high sensitivity of the device it is possible to observe the little quantitive of Ag that are present in the vacuum chamber produced by laser irradiation. The green line in both plot represent the molecule of CH_4 produced in the plasma after irradiation, this kind of investigation permits to discover this molecules produced during the irradiation

and allows a better understanding of time of flight measurement that can be do simultaneously.

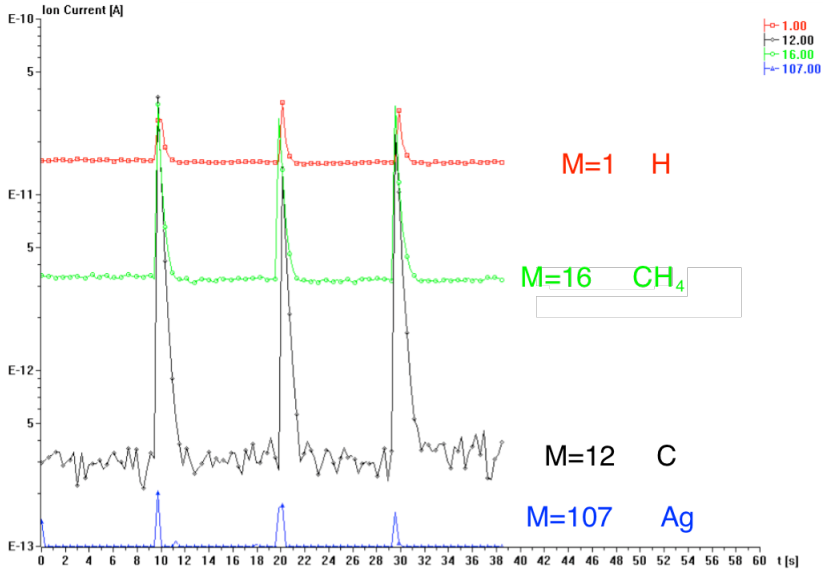

Figure 2.10: *Mass yield vs time of nuclepore polymer target with Au nanoparticles irradiated at* 10^{10} W/cm^2*, in red dots is H particles, blacks C particles, green dots* CH_4 *and blue Ag.*

We can consider the difference between the peak during the laser shot and the background, this difference is related to the quantity of neutral atoms produced during the plasma formation. Taking in consideration the Fig.2.11 it is possible to observe that the presence of Ag nanoparticles enhance the production of C, H and in little part CH_4 molecules. This result can be observe if we take a look to the TOF measurement, Fig.2.12, on the same target were the maximum yield enhance from 10 mV in case of pure nuclepore to about 18 mV with the insertion of nanoparticles [34].

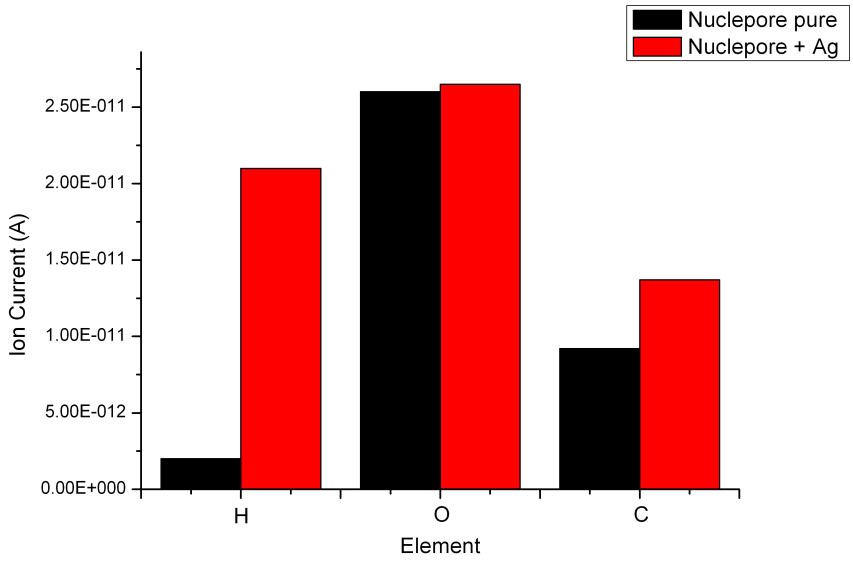

Figure 2.11: *Differences between the quantities of elements in Nuclepore target and Nuclepore+ Ag nanoparticles*

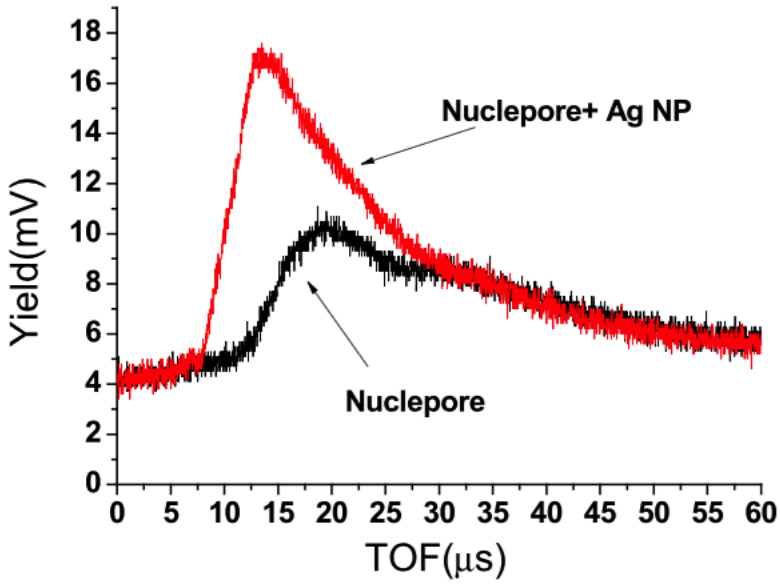

Figure 2.12: *Time of fligh spectra of nuclepore and nuclepore+ Ag nanoparticles*

Table 2.2: Maximum ion kinetic energy of protons, carbon ions, and nanoparticle ion species when polymer substrates are irradiated.

Ion Energy	**Nuclepore**	**Nuclepore + Ag NPs**
E(H^+) (eV)	80	171
E(C^{n+}) (eV)	319	869
E(Ag^{n+}) (keV)		2.55

2.1.4 Optical spectroscopy

This technique is useful in laser-generated plasma characterization not only to determine the spectral emission of such a system, but also to calculate a mean value of electron density and temperature. The calculated electron temperature values, for example, may be compared with the ion temperature ones, obtained by TOF measurements, in order to observe the similarities or differences [35]. The laser is focused to form a plasma, which atomizes and excites samples. Because all elements emit light of characteristic frequencies when excited to sufficiently high temperatures, the optical spectroscopy can (in principle) detect all elements, limited only by the power of the laser as well as the sensitivity and wavelength range of the spectrograph and detector.

Focusing the laser onto a small area at the surface it ablates a very small amount of material, in the range of nanograms to picograms, which generates a plasma plume with temperatures in excess of 100,000 K. During data collection, typically after local thermodynamic equilibrium is established, plasma temperatures range from 5,000–20,000 K. At the high temperatures during the early plasma, the ablated material dissociates (breaks down) into excited ionic and atomic species. During this time, the plasma emits a continuum of radiation which does not contain any useful information about the species present, but within a very small timeframe the plasma expands at supersonic velocities and cools. At this point the characteristic atomic emission lines of the elements can be observed.

Under the assumption of Local thermal equilibrium (LTE) the electron temperature in the plasma can be determined by relative line intensity measurements. If one observes two isolated lines, say 1 and 2 with central wavelength λ_1 and λ_2 , respectively, emanating from the same atomic or ionic species and if the level population are distributed according to the Boltzmann law, the relative intensity of these two lines, I_1/I_2 , can be given as [36]

$$\frac{I_1}{I_2} = \frac{f_1 g_1}{f_2 g_2} \left(\frac{\lambda_2}{\lambda_1}\right)^3 \exp\left(-\frac{E_1 - E_2}{kT_e}\right) \tag{2.1.13}$$

where I, f, g and λ are the total intensity, the absorption oscillator strength for the transition, the statistical weight of the lower level and the wavelength, E is ionization energy, k Boltzmann constant and T_e the electron themperature.

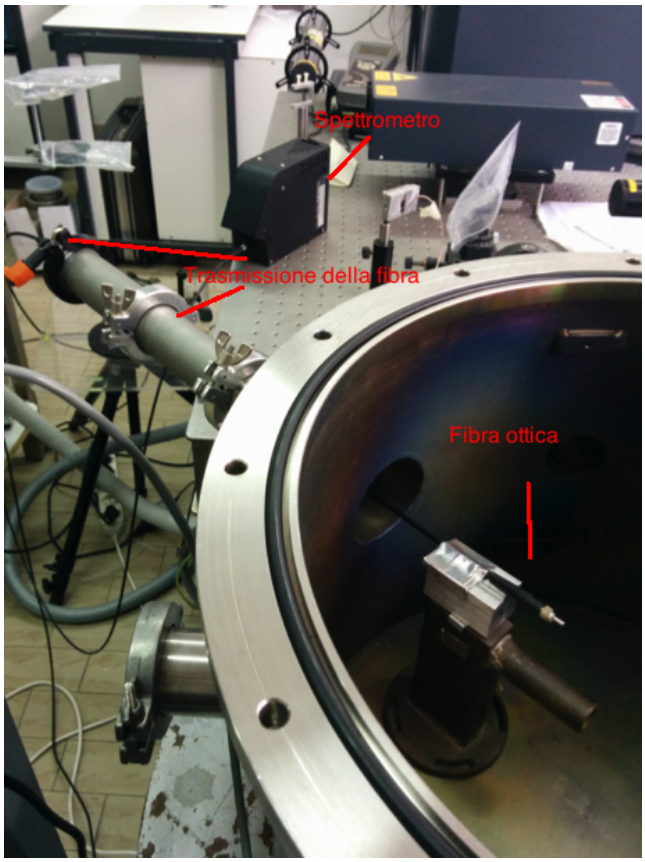

Figure 2.13: *Experimental setup for UV-VIS spectroscopy*

VS140 Linear Array Spectrometer is a spectra analyzer that integrates a spectrograph

and a high performance-multichannel photo-detector in a single compact chassis. Light collection is simplified by using an optical fibre. The diffraction grating of the spectrograph and multichannel photo-detector are rigidly fixed, resulting in excellent wavelength reproducibility. The wavelength axis and spectral response characteristics are calibrated, so that the spectral measurements can be carried out easily and accurately.

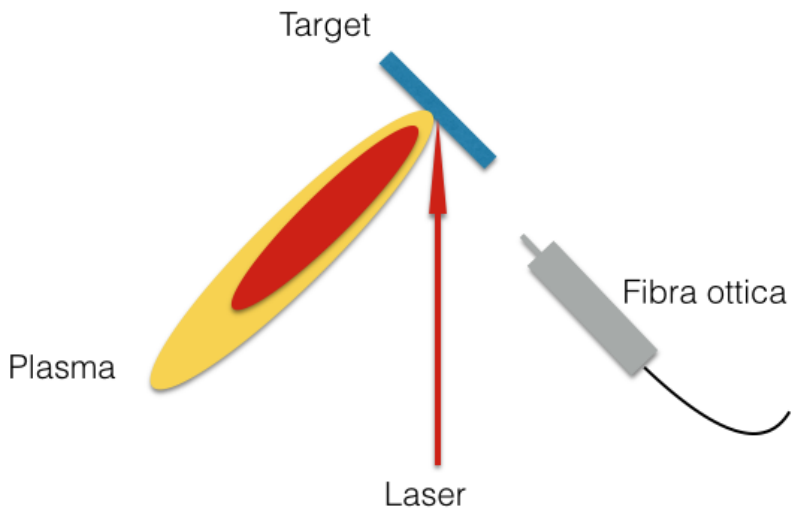

Figure 2.14: *Experimental UV-VIS radiation emitted from Al target irradiated with Nd:YAG laser*

In order to carry out the optical spectroscopy measurements, the optical fiber connected to the spectroscope is placed at 90 degrees with respect to the plasma propagation direction. Photons emitted by the plasma are reflected within the optical fiber until they reach the spectroscope where they can be analyzed depending on the wavelength.

A typical spectrum, obtained by irradiating in vacuum an Al target at first harmonic Nd:YAG wavelength with a 200 mJ laser energy, is reported in Fig.2.15 where we can see the peaks due to the presence of Al^{2+}.

Taking in consideration the wavelenghts $\lambda = 464\ nm$ and $\lambda = 580\ nm$ for Al^{2+},

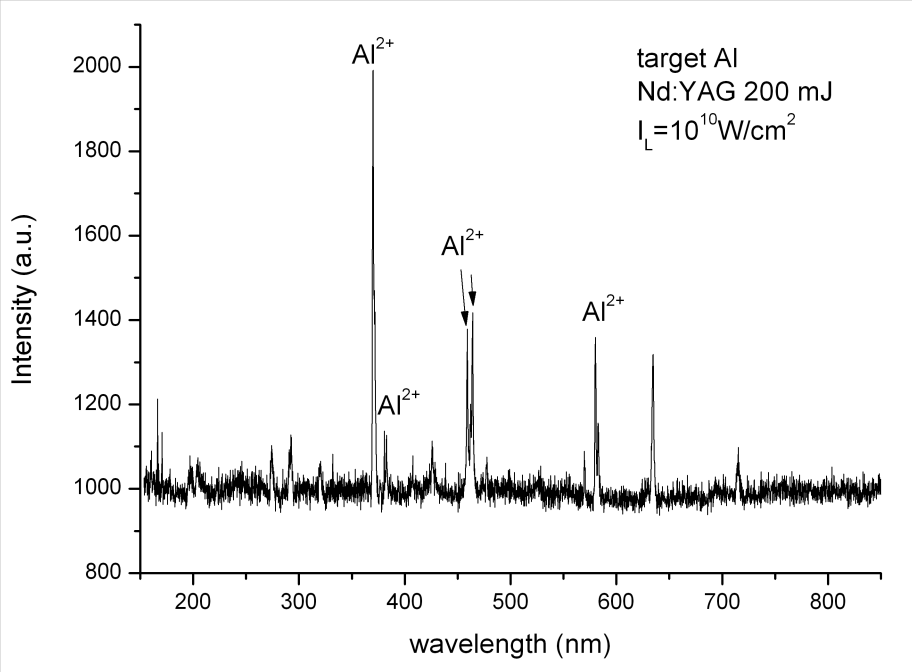

Figure 2.15: *Experimental UV-VIS radiation emitted from Al target irradiated with Nd:YAG laser*

datasheets [37] for g and f values, and using the equation 2.1.13 we are able to calculate the temperature of plasma:

Table 2.3: Value for the electron transition of Al^{2+}

λ **(nm)**	**f**	**g**	**E(eV)**
464	0,104	5	10,59
580	0,15	7	15,05

$$kT_e = 5,13eV \tag{2.1.14}$$

The oscillator strength, f, of a transition is a dimensionless number that is useful for

comparing different transitions. It is defined as the ratio of the strength an atomic or molecular transition to the theoretical transition strength of a single electron using a harmonic-oscillator model. Oscillator strengths can range from 0 to 1, or a small integer. A strong transition will have an f close to 1. Using theoretical values it is possible to obtain a theoretical spectra using simulation by NIST database, in Fig.2.16 is showed the optical emission from an Al plasma with temperature of 5.13 eV.

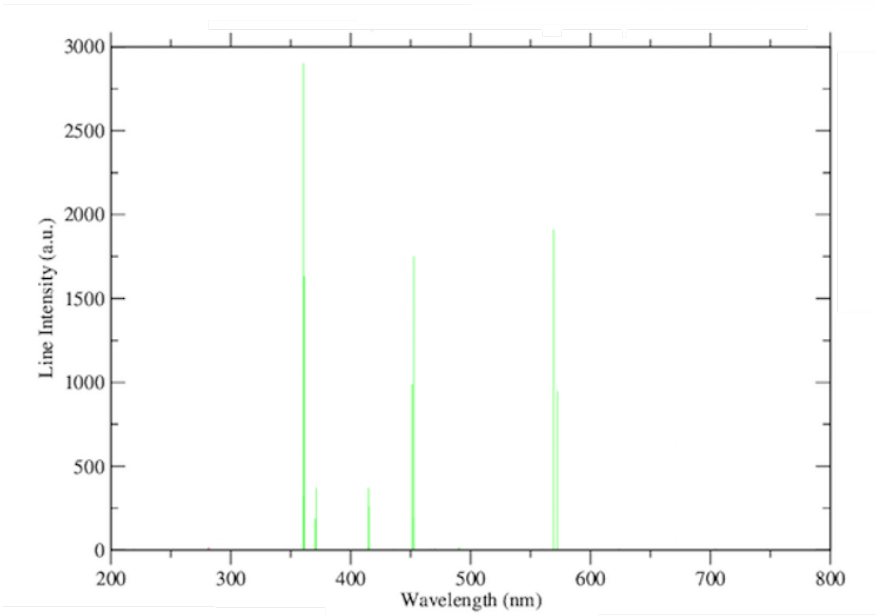

Figure 2.16: *Theoretical UV-VIS radiation emitted from Al^{2+} plasma*

2.2 Plasma diagnostics off-line

2.2.1 Track detectors CR-39

The detection of charged particles, and neutral, using solid state nuclear track detector is of interest to many scientific disciplines, this includes laser-plasma experiments. The solid state track detector is a solid material exposed to nuclear radiation, etched and examined for the characterization of beam. When an ionizing charged particle passes through a dielectric material, the transfer of energy to electrons results in a trail of damage molecules along the particle track. In some materials, the track can be made visible upon etching in a strong acid or base solution. The entire surface of material is attacked, but those points at which particle tracks have entered are etched about 10 times faster. The tracks in this way become large enough to be easily visible through a conventionale microscope [38].

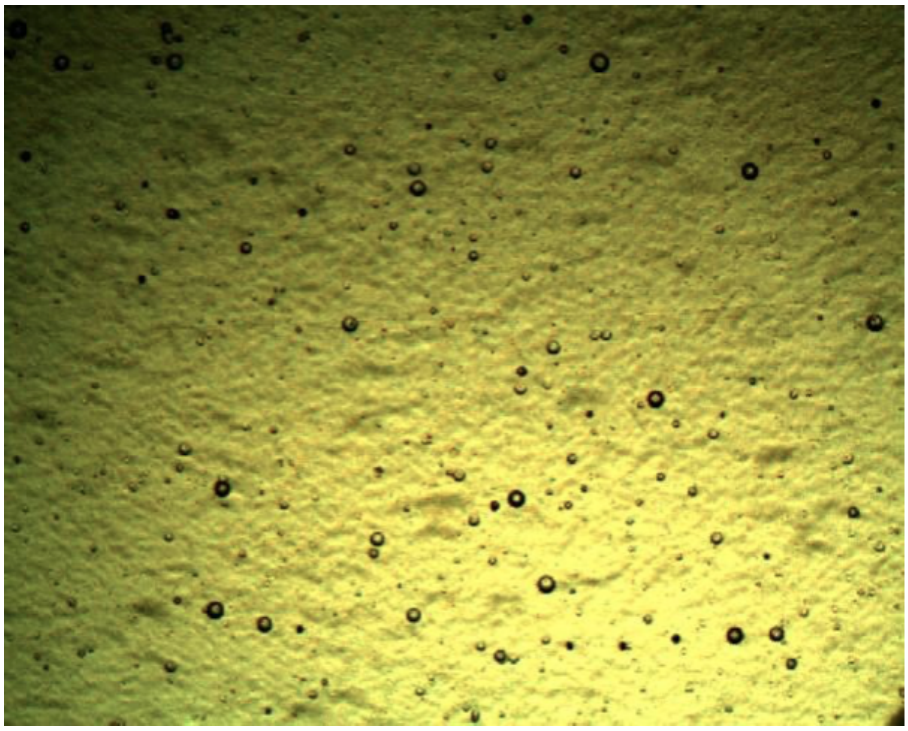

Figure 2.17: *Neutron detection through elastic scattering with protons*

If the interaction between the radiation and the material ar ortogonal, tha shape of path will be circular, otherwise will be elliptical, this will permit to understand the direction of particles. Other information will be get thanks to preliminary calibration for particles energies. It is possible to distinguish particles with different energy and mass.

A qualitive picture of how the tracks are revealed by etching is sketched in Fig.2.18. A track is assumed to exist perpendicular to the surface of the medium, which is exposed to the etching solution. As a simplified model, we assume that the undamaged surface is eroded away at the velocity V_G perpendicular to the surface. We further assume that the etching velocity along the damage track is a greater value V_T. Under these conditions, the sketches illustrate that a coneshaped pit is formed with an axis along the damage trak. Usign this model, it can be shown that the angle of incidence must exceed a critical angle θ_C in order to avois its disappearance due to the progressive etching:

$$\theta_c = arcsin\left(\frac{V_G}{V_T}\right) \tag{2.2.1}$$

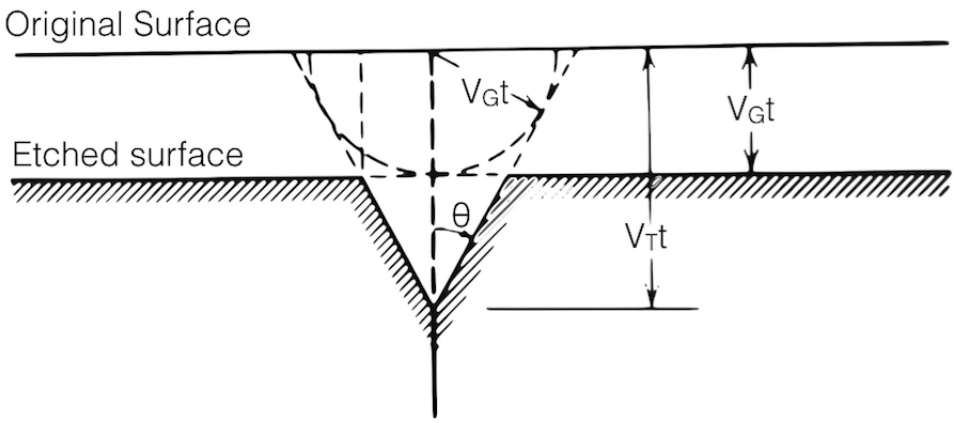

Figure 2.18: *Model of track etching*

The erosion velocity depend to several parameters of etching process. The main parameters can be identified like temperature, concentration of acid and time of erosion. Many investigations are carried out to discover how the etching characteristics of CR-39 de-

tectors change with varying conditions of the etching process.In Fig.2.18 is showed the erosion process described above. In the non-irradiated zone, the erorion is costant while in the irradiated material there is an increase of erosion with the conical shape of aperture θ in addition to the normal erosion.

Normally the etching is made using NaOH like etchant or solution of NaOH/ethanol. The bulk etch rate properties of NaOH/ethanol were tested by etching CR-39 (polyallyl diglycol carbonate) in NaOH/ethanol of various temperatures and molarities. It was found that as temperature increased the bulk etch rate increased. However, the molarity of the NaOH/ethanol solution did not have a significant effect on the bulk etch rate [39]. The five measurements taken at each 30 minute interval were averaged to find the average thickness of the CR-39 detector at each interval. For each interval, the average thickness was subtracted from the initial average thickness to find the amount of CR-39 removed in millimeters. These values were plotted on a graph with x-values representing time in hours and y-values representing the amount of CR-39 removed in millimeters Fig.2.19 1.5M NaOH/ethanol at $60°C$ yielded the fastest bulk etch rate of $27.3\mu m/hr$.

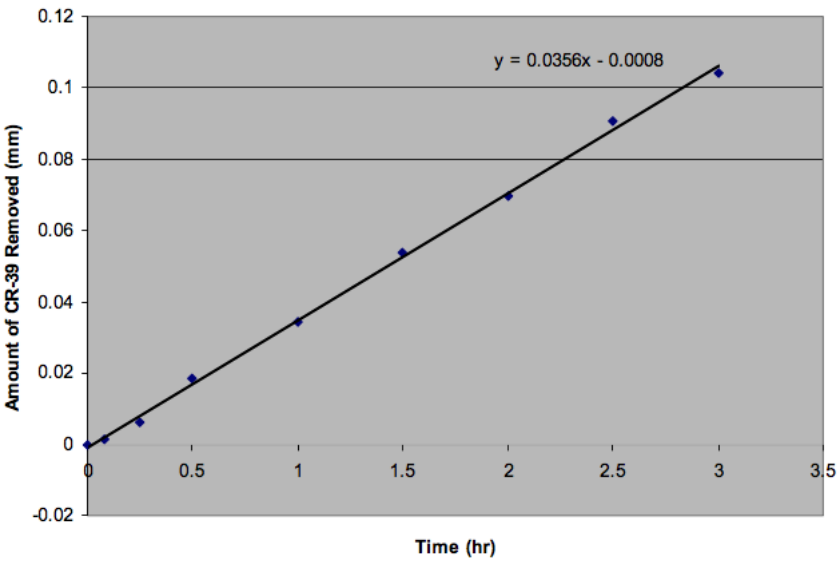

Figure 2.19: *The amount of bulk removed from CR-39 detector in 2.5M NaOH/ethanol at* $60°C$ *over time*

As the temperature of NaOH/ethanol increased the bulk etch rate increased. Change in molarity had a greater effect on the bulk etch rate as temperature increased, but there is no apparent relationship between molarity and bulk etch rate for all temperatures. The bulk etch rate of NaOH/ethanol at $50°C$ was consistent despite changes in molarity. These results are summarized in Fig.2.20

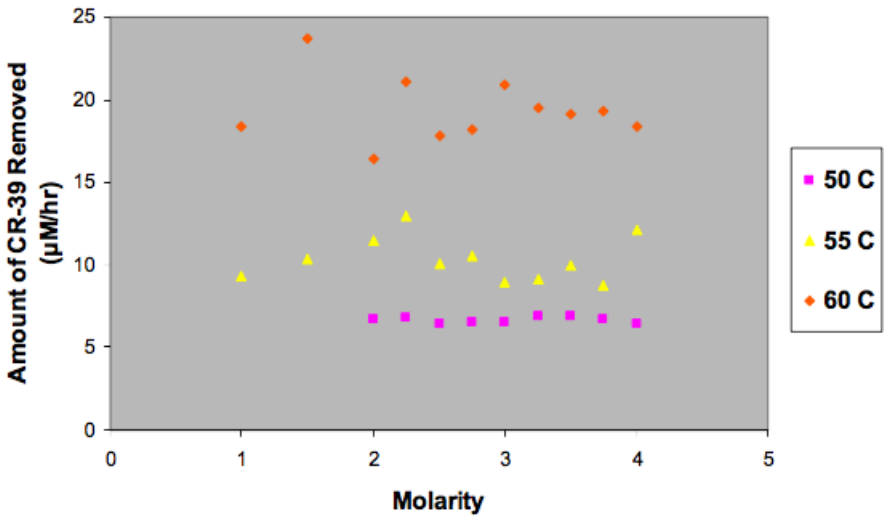

Figure 2.20: *The bulk etch rate of CR-39 in NaOH/ethanol solutions as a function of Molarity at different temperatures*

2.2.2 Surface Profilometer

The Profilometer is a measuring instrument for quantifying the roughness of a surface.

There are two types of profilometers: stylus vs optical. Stylus profilometers use a probe to detect the surface, physically moving a probe along the surface in order to acquire the surface height. This is done mechanically with a feedback loop that monitors the force from the sample pushing up against the probe as it scans along the surface. A feedback system is used to keep the arm with a specific amount of torque on it, known as the 'setpoint'. The changes in the Z position of the arm holder can then be used to reconstruct the surface.

Stylus profilometry requires force feedback and physically touching the surface, so while it is extremely sensitive and provides high Z resolution, it is sensitive to soft surfaces and the probe can become contaminated by the surface. This technique can also be destructive to some surfaces.

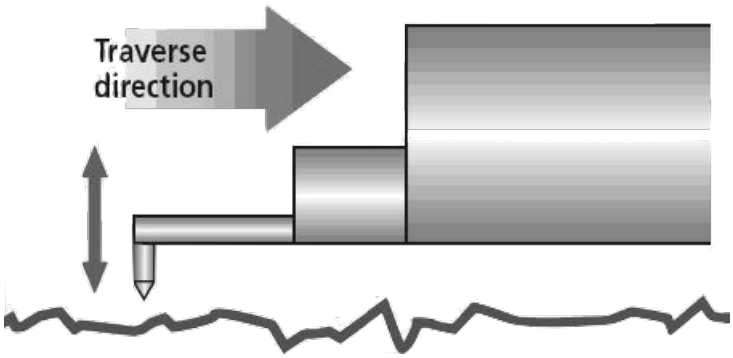

Figure 2.21: *Schema of how work a stylus profilometer*

Because a stylus profilometer involves physical movements in X, Y and Z while maintaining contact with the surface, it is slower than non-contact techniques. The stylus tip size and shape can influence the measurements and limit the lateral resolution. Optical profilometry uses light instead of a physical probe. This can be done a number of ways. The key component to this technique is directing the light in a way that it can detect the surface in 3D [40]. Examples include optical interference, using a confocal aperture, focus and phase detection, and projecting a pattern onto the optical image.

The Tencor P-10 Surface Profilometer is stylus type and characterizes a substrate by scanning it with a thin diamond stylus. A diamond stylus moves vertically in contact with the sample and then laterally through the sample to measure the distances and the specific contact forces. A profilometer can measure small vertical surface variations as stylus position functions. The resulting trace represents a cross-sectional view with high vertical and spatial resolution. The instruments digitizes the data signal to permit an easy evaluation of the results, in addition, the software provide storage facilities for data and scan recipes. The Tencor P-10 has a capacity sensor that registers the horizontal and

vertical motion of the stylus. The measurement stage rests on an optical flat reference that ensures smooth and stable movements across the scan length. The guide bar for the stage provides straight and directional movements of the stage beneath the stylus. The instrument has 10 Å vertical resolution and 100 Å horizontal resolution. During the measurement there is the possibility to display the sample by an optical microscopy with two possible image magnifications (150x and 600x).

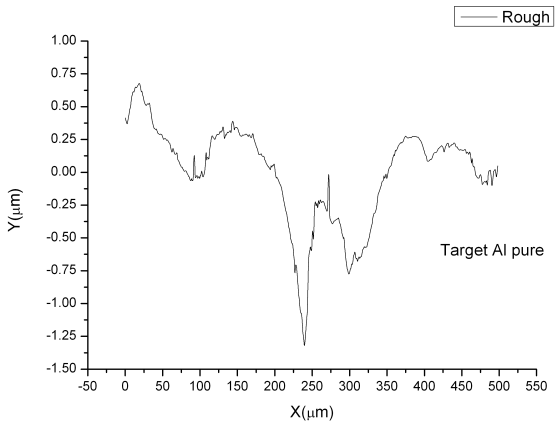

Figure 2.22: *Profile of Al pure surface performed with Tencor P-10 Surface Profilometer*

The Tencor P-10 is important to perform "ex situ" measurements regarding the determination of crater depth, shape and dimension. Such measurements, in fact, permit to understand some formation mechanism of the plasma and, moreover, to calculate the plasma ablation yield, i.e. the mass emitted per laser pulse. In Fig.2.22 is shown the pure surface of an Al target before laser irradiation. It is possible to observe that before laser interaction the maximum vertical depth is about 1.5 μm. After the laser interaction we can observe the same target but we measure the crater profile. Crater profiles performed after pulsed laser ablation are shown in Fig.2.23 refers to a crater obtained after 1 pulse of the 1064 nm Nd:YAG on the same Al target, performed at *Brookhaven National Laboratory* (BNL) with a laser energy of 1094 mJ.

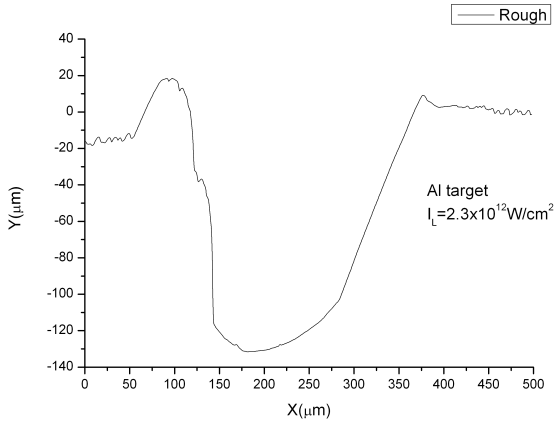

Figure 2.23: *Profile of crater on the surface of Ta target irradiated at LNS with Nd:YAG laser*

Calculating the crater volume and knowing the target material density, it is possible to give an estimation of the ablation yield in terms of ablated mass per laser pulse. The calculated values for the crater shown in Fig.2.23 is about:

$$V = \frac{\pi r^2 h}{3} = \frac{\pi (300\mu m)^2 115\mu m}{3} = 10,83 \cdot 10^{-12} m^3 \tag{2.2.2}$$

Considering conical shape for the crater, a radius of 300 μm and height 115 μm. From the density of material we can calculate the total amount of mass removed from surface:

$$m = V \cdot \rho = 10,83 \cdot 10^{-12} m^3 \cdot 2700 \frac{kg}{m^3} = 2.9 \cdot 10^{-8} kg = 29\mu g \tag{2.2.3}$$

With this type of measurements are obtained the yield curves as a function of laser fluence. From the eroded material is possible to calculate the number of particles like show in Fig.2.24 [41] useful for the calculation of ablation threshold. The results are very attractive because they permit to evaluate, approximately, the ionized component (obtainable using time of flight detector) relative to the neutral one.

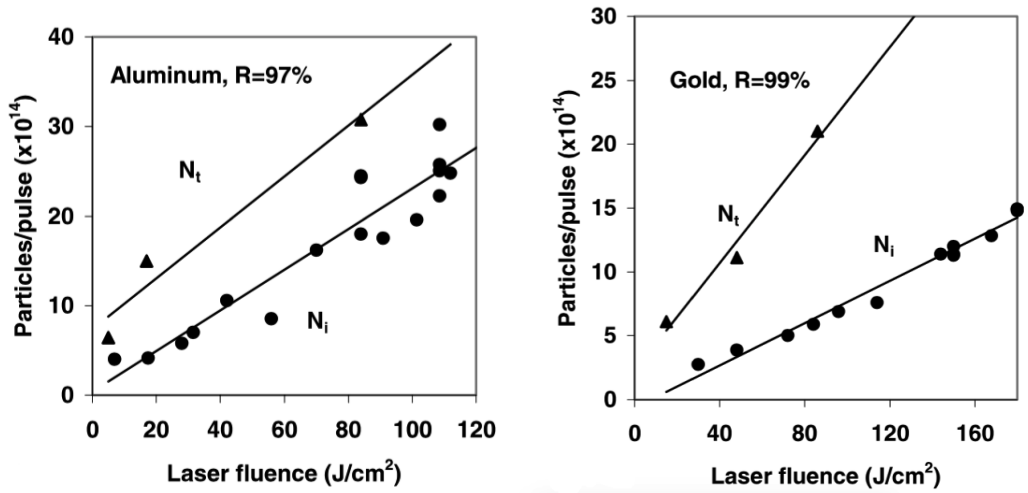

Figure 2.24: *Total and neutral number of particles emitted from laser-generated plasma in Al (left) and Au (right) targets*

Optical and modern profilometers use optical system to analyse the surface and obtain 3D view of craters, an example is reported in Fig.2.25 where an Al target were irradiated with Nd:Yag laser and using a software calibration was possible to make 3D reconstruction and characterization of laser induced craters by in situ optical microscopy.

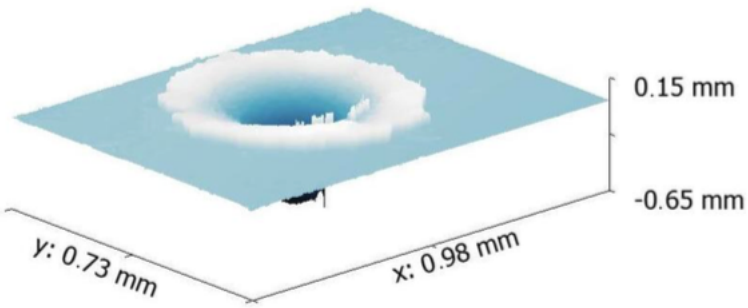

Figure 2.25: *3D crater obtained using optical profilometer*

Chapter 3

Electric and Magnetic deflections for plasma diagnostics

For to perform plasma diagnostics can be used the deflections caused by the presence of external electric and/or magnetic field to distinguish the ionic components of plasma and find their energies and charge states. Indeed particles with different charge states, mass and energy are deflected through differents trajectory inside the fields. These diagnostics are important because knowing the energy distribution, the angle of deflection and other features measurable thanks to the used field, it is possible to calculate the plasma temperature, the self-generated electric field and others as a function of laser intensity. The diagnostics that will be presented in this chapter are based on the same principle descrived above on the deflection of charge particles in fields. The only electric deflection used in the Ion Energy Analyser permits the study of the energetic distributions, but we need to perform a big number of measures, so of shots. This isn't always possible, for example thin target are damaged after the first shot, for this the Ion Analyser is an unusable technique in TNSA regime. Instead the magnetic deflection permits in a single shot to obtain the separation of all charge state without filter operation like will be showed. The simultaneous use of magnetic and electric fields is widely used for decades in the beam diagnostic using Thomson Parabola Spectrometer, device that in a single shot shows all

charge state inside of plasma and the energetic range of particles. The Thomson Parabola Spectrometer will be discussed and will be showed of our device studied for low energy plasma.

3.1 Ion Energy Analyzer

The mass spectrometer described below is an electrostatic cylindrical ion energy analyzer (IEA) combined with the time-of-flight method designed for the diagnostics of pulsed ion sources. In particular, it is used for measurements of laser-produced plasmas [26]. The main part of the IEA is the deflection system. It is a sector of two coaxial metallic cylinders of radiuses R_1 (inner plate) and R_2 (outer plate) maintained at potentials V_1 and V_2 , respectively and with deflection angle θ, like showed in Fig.3.1.

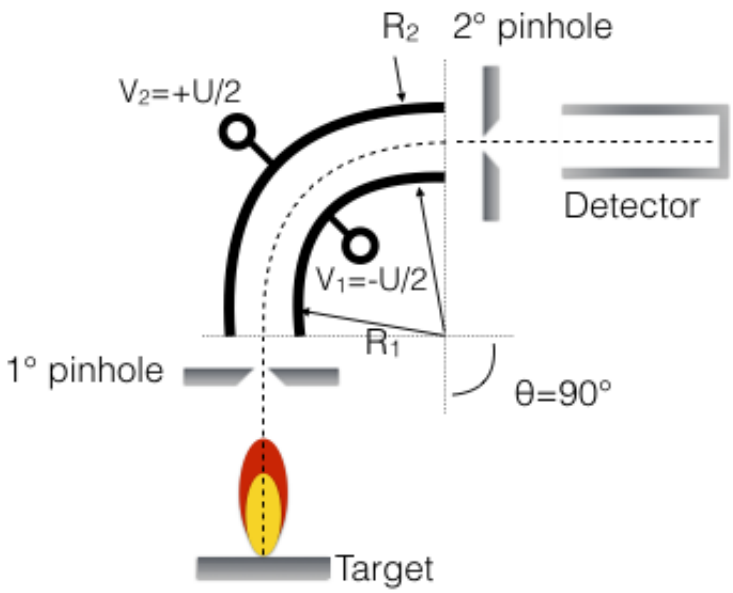

Figure 3.1: *Schematic drawing of IEA.*

The radial electric field inside the deflection system is given by:

$$E_r = \frac{V_2 - V_1}{r \ln \frac{R_2}{R_1}} \tag{3.1.1}$$

where $r$is the radius of an equipotential surface and $R_1 \leq r \leq R_2$. If the potentials are symmetric, $V_2 = -V_1 = U/2$, there is a equipotential surface $V_0 = 0$ for:

$$r = R_0 = \sqrt{R_1 R_2} \approx \frac{R_1 + R_2}{2} \tag{3.1.2}$$

Under these conditions the force equation is:

$$\frac{Mv^2}{R_0} = ezE_r \tag{3.1.3}$$

Where M is the mass of particle, v the velocity and ez its charge. The previus can be rewrite like:

$$\frac{E}{z} = eR_0E_r = \frac{eU}{2ln\frac{R_2}{R_1}} \approx keU \tag{3.1.4}$$

where $k = R_0/(2\Delta R)$, with $\Delta R = R_2 - R_1$, is the geometric factor of the IEA and E is the kinetic energy of the particle. We have that only ions with a given energy-to-charge state ratio, E/z, can pass through the IEA, that is, the IEA is operated as an energy filter. Ions are separated on the path of flight d from the ion source to the detector due to their energy spread. The time of flight of ions from the ion source to the detector is

$$t = d\sqrt{\frac{M}{2E}} = d\sqrt{\frac{M}{2ezkU}} \tag{3.1.5}$$

From the previous equation we can understand that the IEA allows both to create energy distributions of the same ion species in the different states of charge, both to function as a spectrometer and identify various elements, as having different masses (E/z set by the energy filter) will reach the detector at different time.

In Fig.3.2 is reported a schema of experimental setup for TOF-IEA measurements in Messina, while in Fig.3.3 is reported pictures of setup and deflection zone, respectivelly.

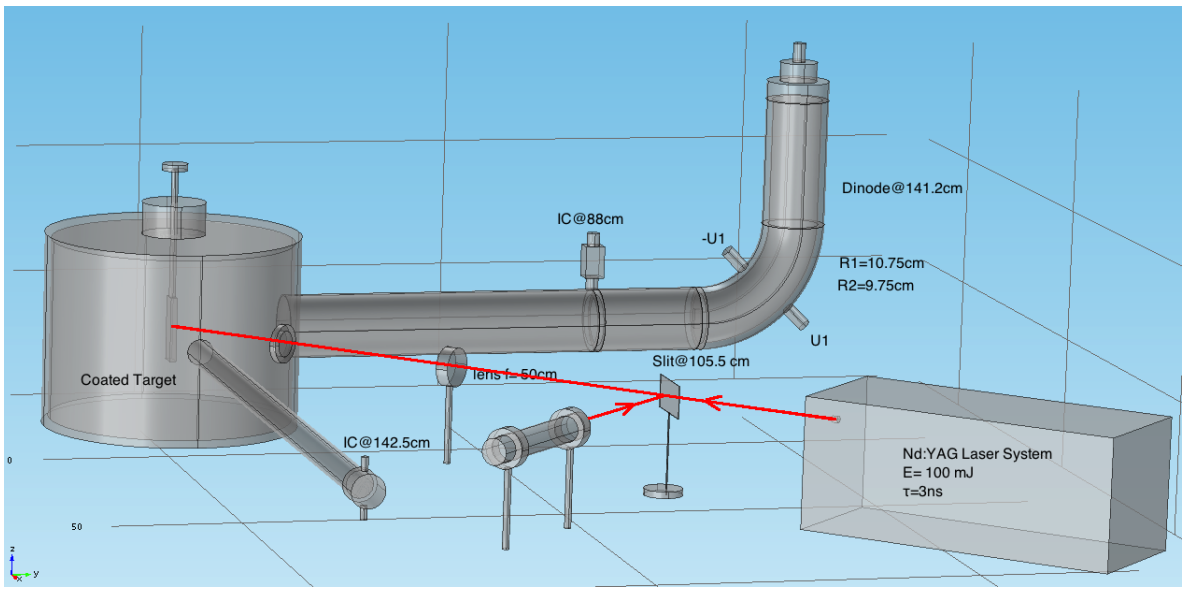

Figure 3.2: *Draw of experimental setup of IEA present in Messina*

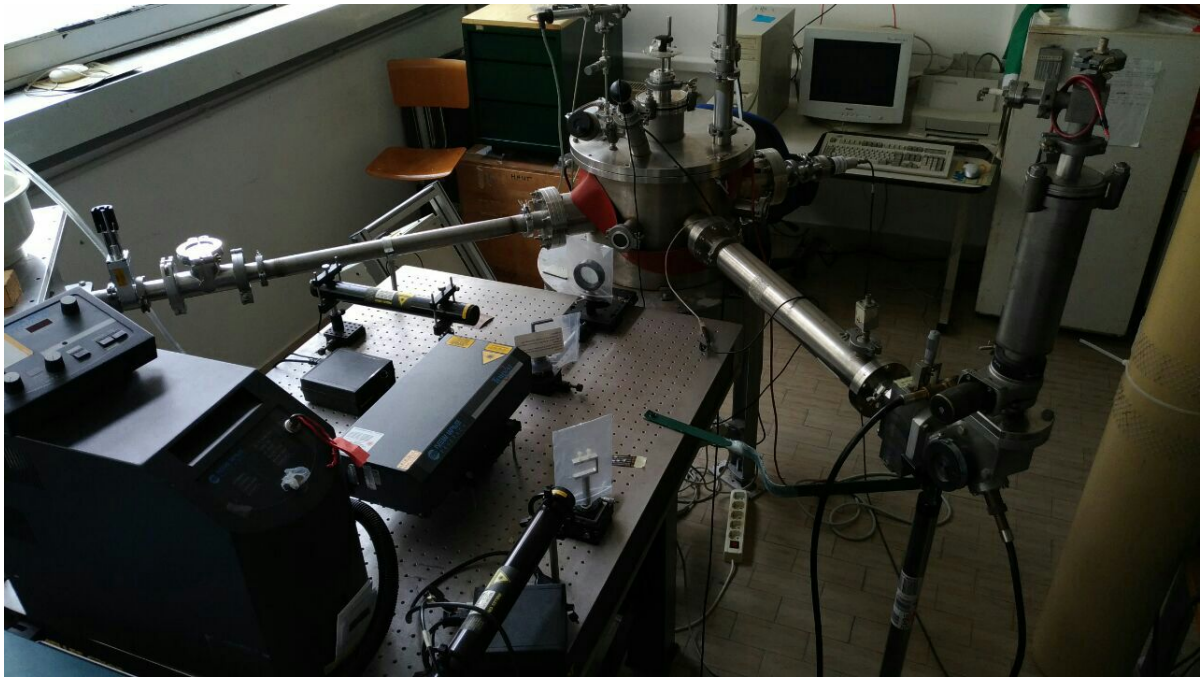

Figure 3.3: *Picture of experimental setup for IEA present in Messina*

3.1.1 IEA resolution

One of the basic characteristics of a mass spectrometer is its resolving power. The mass resolution of an electrostatic analyzer is given by[26]:

$$\begin{aligned} R_m &= \frac{m}{\Delta m} = \frac{t}{2\Delta t} \\ m &= \frac{m_1 + m_2}{2} \\ \Delta m &= m_1 - m_2 \end{aligned} \tag{3.1.6}$$

where with m is indicate the mass-charge state ratio, t is the time of flight of an ion that may be resolved from a neighboring ion, and Δt is the time distance between the resolved ion pulse.

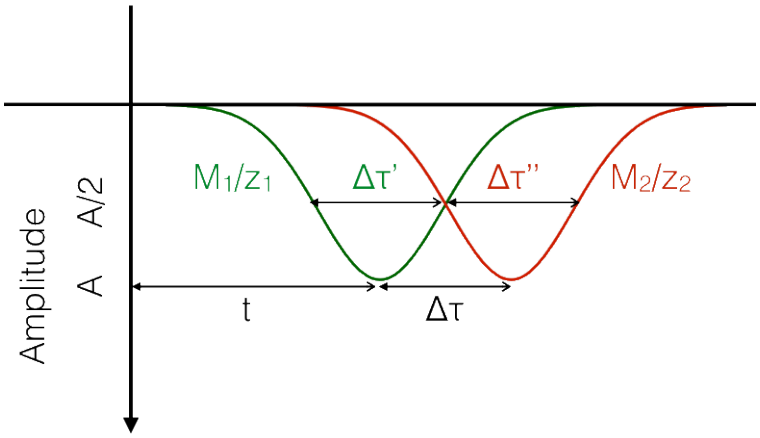

Figure 3.4: *Explanation of notations used for resolving power determination*

3.1.2 Analysis of IEA spectra

Taking in cosideration a spectrum obtained using IEA is possible to get informations about the energetic distribution of each charge state, the temperature of plasma, the yields per charge state and accelerating fields. To obtain all informations about plasma we need to perform several shots changing each time the voltage of plate for the deflection. For each voltage we have a ratio E/z take from $E/z = ekU$.

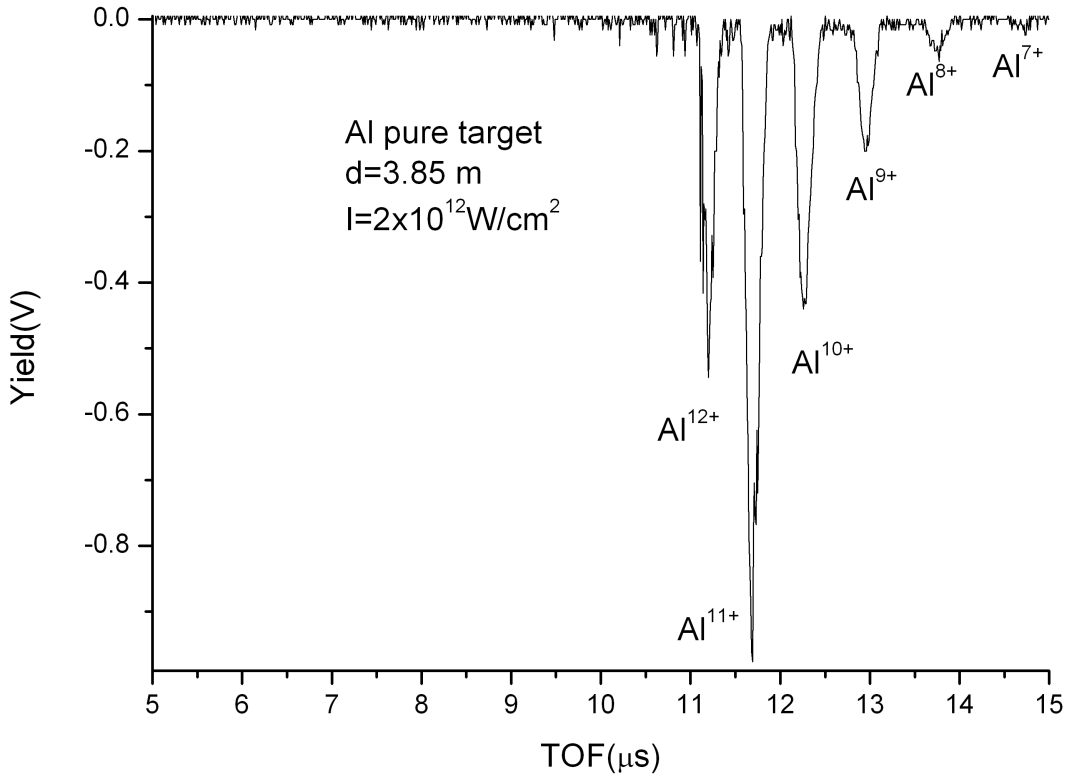

Figure 3.5: *IEA spectrum obtained irradiated Al target with* 10^{12} W/cm^2 *laser intensity and 70 V per plate*

Considering the Fig.3.5 it shows a typical spectrum obtained by irradiation of Al target using Nd:YAG laser with 10^{12} W/cm^2 intensity and using an IEA with geometrical parameter of 10. The applied voltage per plate was $70V$, that means that only ions with $E/z = 1.4$ keV are detected from the instrument. In this case there is a presence of 6 charge state of Al ions, from Al^{7+} to Al^{12+} like shows in the experimental spectra. The corresponding energy distribution is shows in Fig.3.6

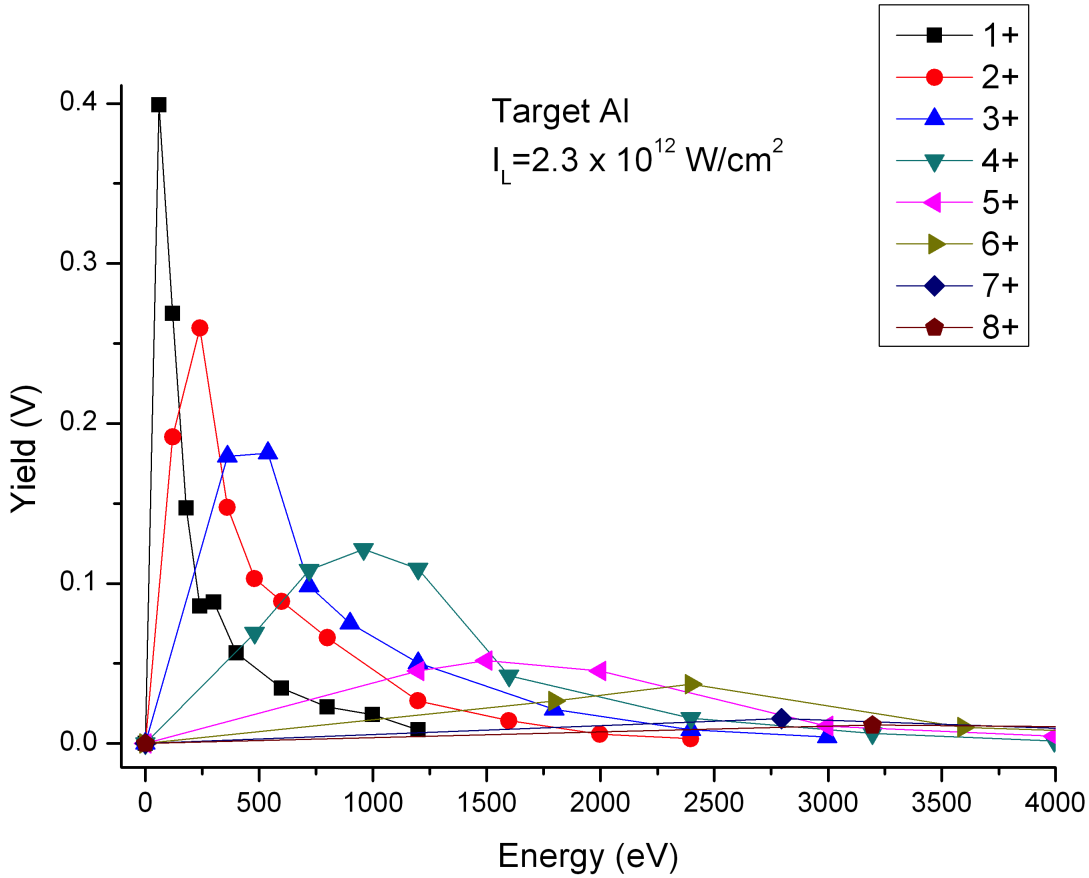

Figure 3.6: *Energy distribution obtained from IEA spectrum obtained irradiated Al target*

In particular from a spectra like Fig.3.6 it is possible to obtain informations about the yield per charge state, the energy separations and more. In this case the yield reduce with high charge state and energy separation increase. Considering the distribution of a single charge state it is possible to do the fit for the determination of plasma temperature. In the case take in consideration of Al target, if we consider the charge state 4+ we can use the CBS [20] function describes in chapter 1 for make the fit. The results of the fit operation is reported if Fig.3.7, where we found a plasma temperature of 125 eV.

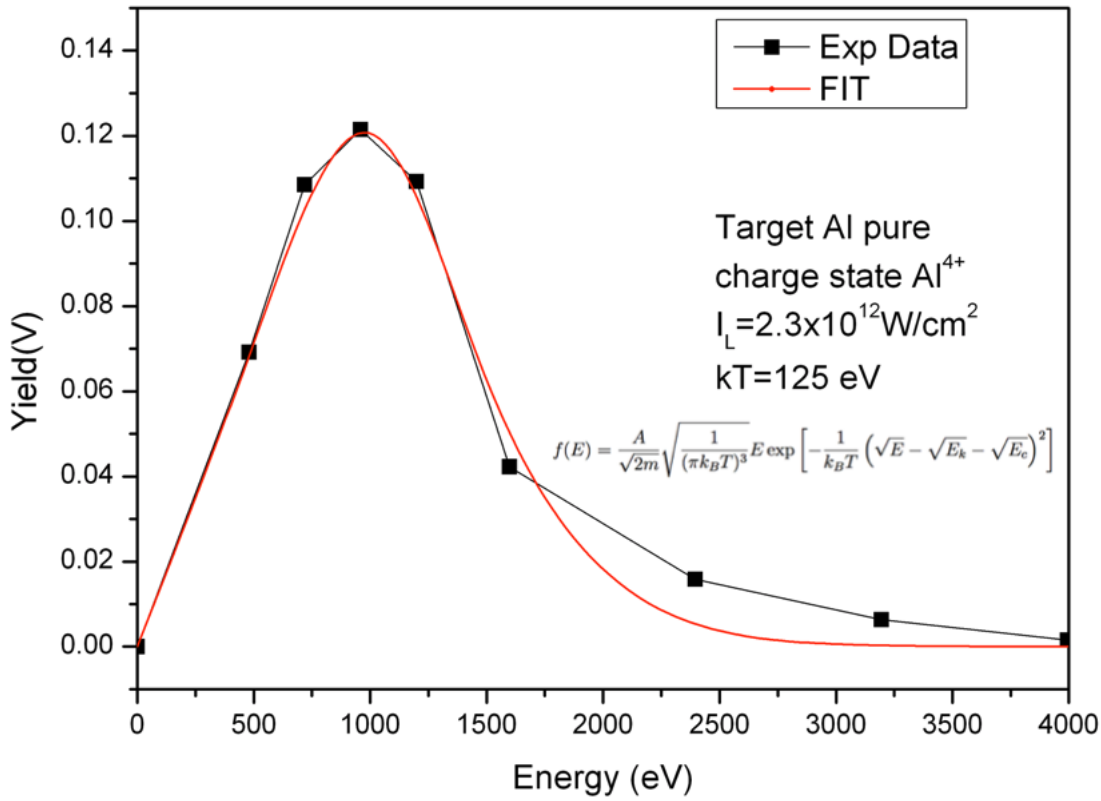

Figure 3.7: *Fit operation on Al^{4+} peak using CBS function*

We can observe the differences between the spectra obtained with 10^{12} W/cm^2 of laser intensity and 10^9 W/cm^2 on the same target. Take in consideration the results reported in Fig.5.21 and Fig5.13 we can observe that the max charge state is in this case only 3+ just in little quantities.

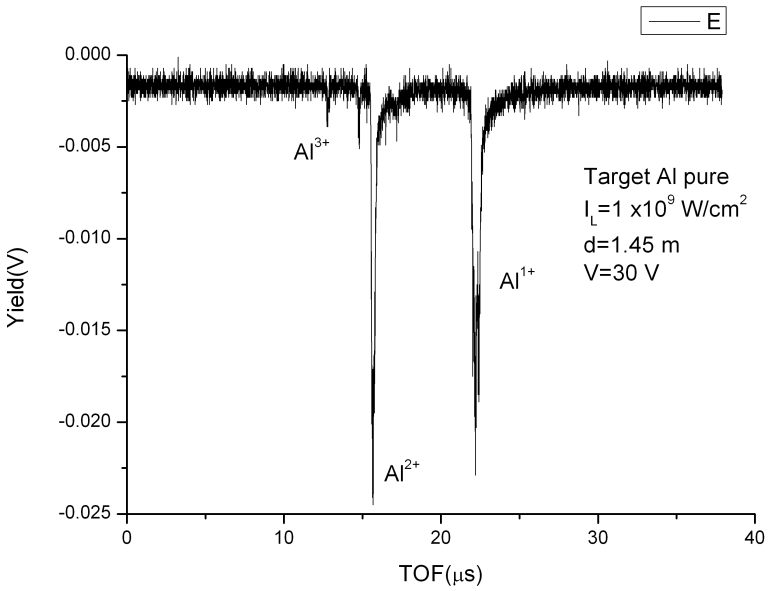

Figure 3.8: *IEA spectrum of Al target at* 10^9 *W/cm*^{2} *and 30 V per plate of deflection*

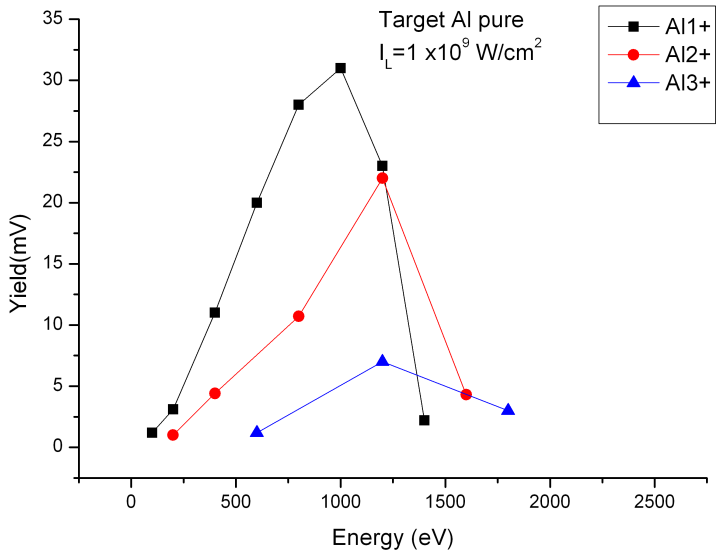

Figure 3.9: *Al energy distribution obtained at* 10^9 *W/cm*^{2} *laser intensity*

If we make a fit operation also for results obtained using Nd:YAG laser at 10^9 W/cm^2 we can observe that the temperature is less compared with 10^{12} W/cm^2, in particular we have 50 eV of plasma temperature.

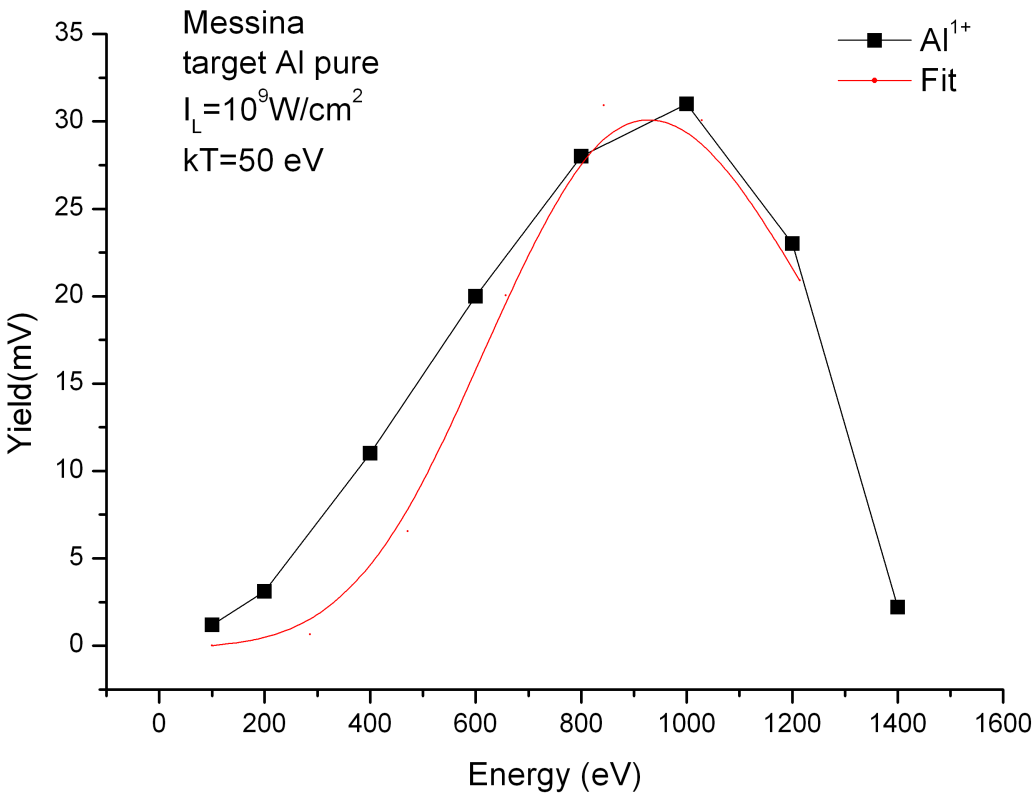

Figure 3.10: *Fit operation on Al^{1+} peak using CBS function on data obtained with* 10^9 W/cm^2

We spoke about the limitation of IEA due to the high number of shots that are needed. There is another important limitation link to the energetic rang of application of the IEA. This limitation is due to to the limit that there is in the potential applicable between two plates before it happens the breakdown. Remembering that $E/z = ekU$ if we conrider

that there is an U_{max} there will be:

$$\left(\frac{E}{z}\right)_{max} = ekU_{max} \tag{3.1.7}$$

Generally the limit is about some MV/m, this for plates that are placed at the distance of some mm means U_{max} of about ten KV, so $\left(\frac{E}{z}\right)$ can be max hundreds ok keV, this involves that ions with energy above $E/z \geq 1MeV$. For produced beam with this high energy are employed diagnostics that don't present this limitations in energy but permits to analyse very high energy beam from laser-produced plasma and allows to study many characteristics of beam in a single shot. A device of this type is the Thomson Parabola describe below.

3.2 Thomson Parabola Spectrometer

The Thomson Parabola (TP) is a spectrometer much used in plasma physics generated by laser bacause it allows to obtain information both on the energy of that beam and on the state of ionization of the ions [42]. It consist of three main parts: the deflection of particles, the collimation region and the detection. For the collimation generally are used pinholes for the convergence of beam, for the deflection are used electric and magnetic fields with parallel direction and orthogonal to the direction of propagation of the beam and for detection can be used MCP, phosphor screen and imaging plate.

3.2.1 Principle of operation

Thanks to the presence of fields the ions are deflected with force:

$$\mathbf{F} = q(\mathbf{E} + \mathbf{v} \times \mathbf{B}) \tag{3.2.1}$$

the motion equations are:

$$x = \frac{1}{2}\frac{Ze}{Am}\frac{Bl_B^2}{v} \tag{3.2.2}$$

$$y = \frac{1}{2}\frac{Ze}{Am}\frac{El_E^2}{v^2} \tag{3.2.3}$$

with:

- e elementary charge;
- Z charge state of ion;
- m mass unit;
- v ion velocity;
- l_E length of electric field;
- l_B length of magnetic field;
- A atomic mass;
- E electric field magnitude;
- B magnetic field magnitude.

from these follow:

$$y = \frac{2E}{l^2 B^2} \frac{Am}{Ze} x^2 \tag{3.2.4}$$

this is a parabola equation, it is simple to understand that ion with different charge state, mark out on the detector different parabola, while a single parabola are marked from ion with same charge state but different energy.

In Fig.3.11 is shown a typical setup of Thomson Parabola Spectrometer, different configurations can be equipped with a deflection zone in which the magnetic and electric field overlap. The distances between the various components are importants parameters can change the results of experiments.

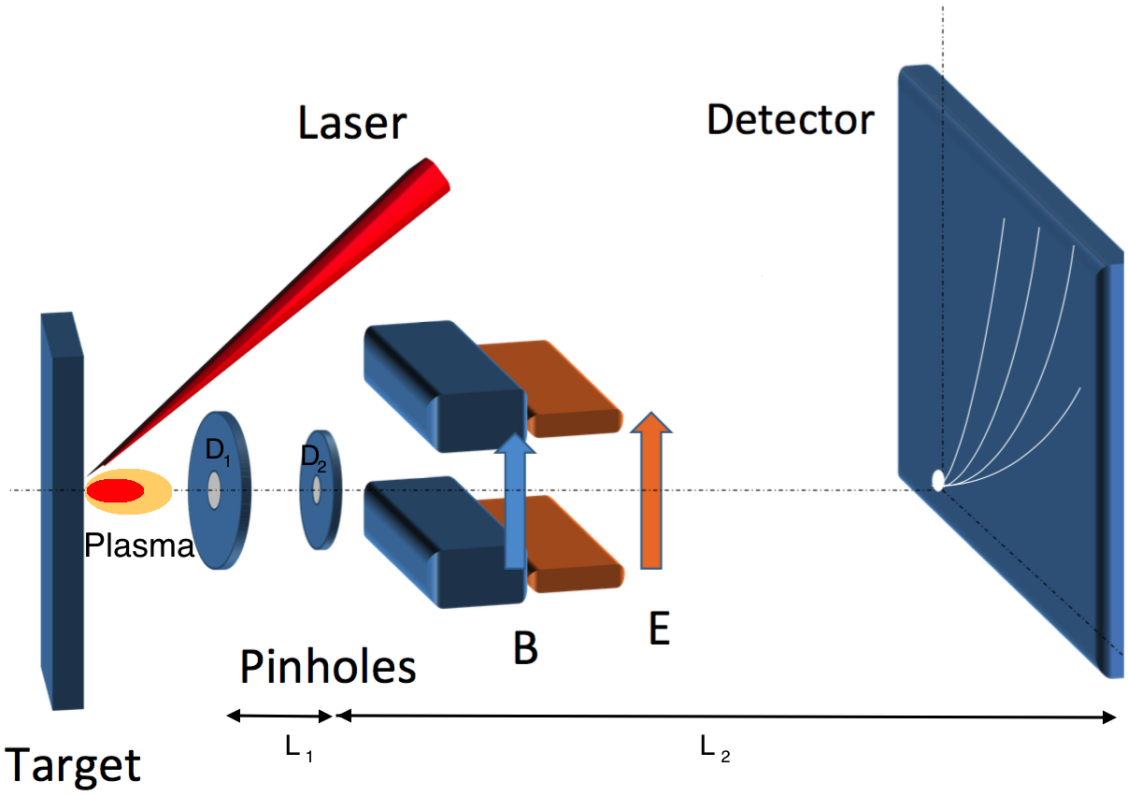

Figure 3.11: *Thomson Parabola schema*

3.2.2 Collimation and Spatial Resolution

A major purpose of the Thomson spectrometer is to separate parabolas of different charge to mass ratio in order to differentiate ion species and charge state. This, in principle, happens naturally if the parabola is an infinitely thin line. Practically, however, this can never be done since the collimation procedure utilizes two pinholes which produce an image with a finite diameter. Considering a collimation system that consist of two pinholes. The thickness of the parabola on the detector, $D3$, it is possible to calculate from geometrical consideration [43]:

$$D_3 = \frac{L_2}{L_1}(D_1 + D_2) + D_2 \tag{3.2.5}$$

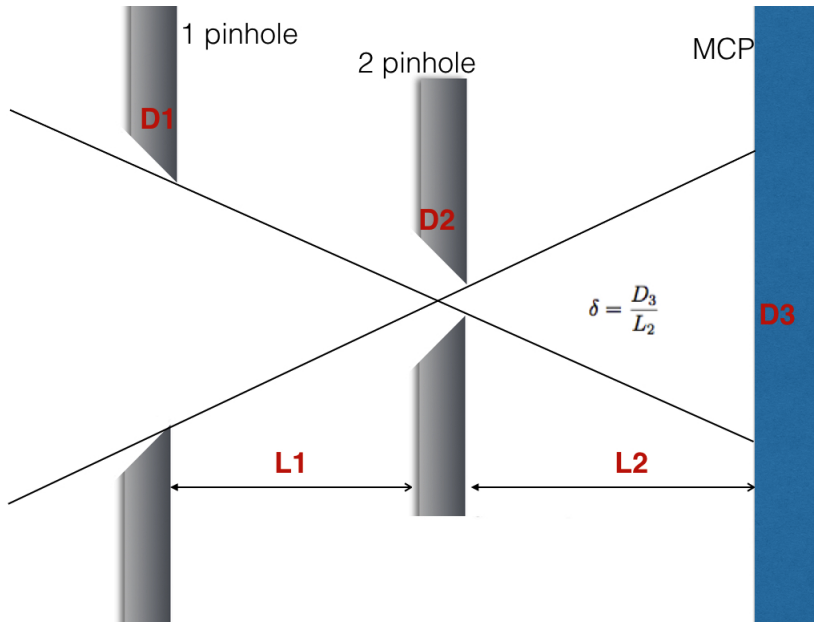

Figure 3.12: *Detector image geometry showing spot sizes given by 3.2.5*

This corresponds to a subtended angle of

$$\delta = \frac{D_3}{L_2} \tag{3.2.6}$$

Defined in this way, δ is expressed in radians. Making an example in wich we use D_1 is $1mm$ and D_2 is $0.1mm$, with $L_1 = 100mm$ and $L_2 = 200mm$, we can calculate:

$$\begin{aligned} D_3 &= \left[\frac{200}{100}(1+0.1)+0.1\right] mm = 2.3mm \\ \delta &= \frac{2.3mm}{200mm} = 0.0115rad \end{aligned} \tag{3.2.7}$$

Consireding the angle deflection, two parabolas will be resolved when the vertical distance from their centers ($\Delta\theta_m$) is bigger of thickness δ of parabolas. Considering the electrical and magnetic deflection angles, θ_e and θ_m respectively, it is possible get for the resolution in charging the equation of a line below which parables are not distinguished [43]:

$$\theta_m = \left\{\left[4+\left(\frac{k}{A\delta}\right)^2\right]^{1/2} - 2\right\}^{1/2} \theta_e \tag{3.2.8}$$

with:

$$\theta_m = \frac{Ze\int Bdl}{p} \qquad \theta_e = \frac{Ze\int Edl}{E_{kin}} \qquad k = \frac{e}{u}\frac{\left(\int Bdl\right)}{\int Edl} \tag{3.2.9}$$

where A is the atomic mass, Z the charge state, p the linear momuntum, u the unit mass of nucleon. In Fig.3.13 are shown examples in which the parabolas are overlapped because of their thickness, is also shown the resolution line that separe the region where the parabola are overlapped and the region where are separeted.

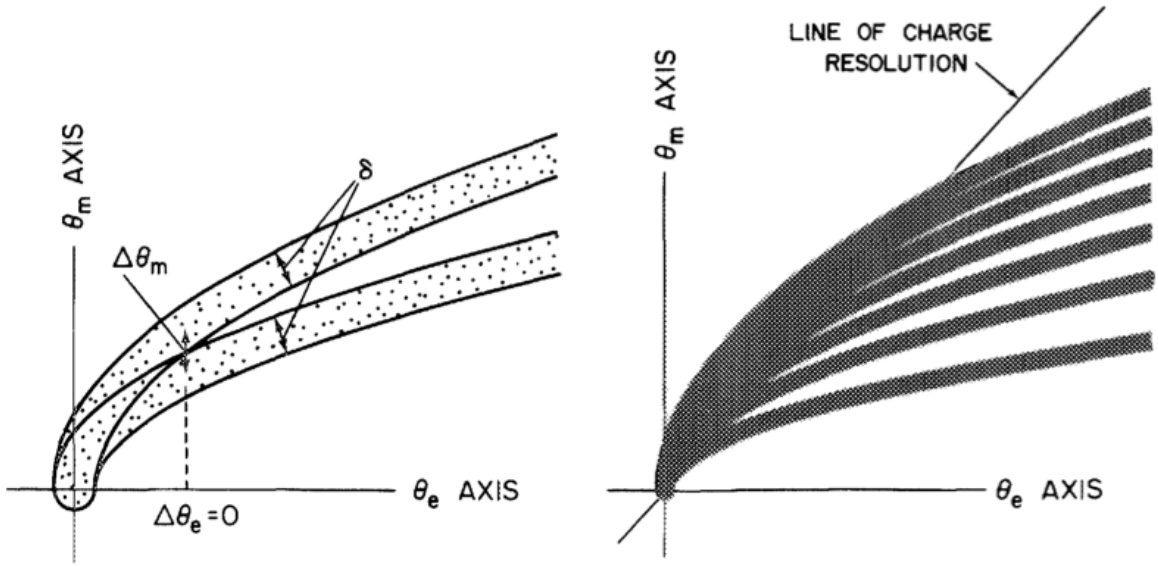

Figure 3.13: *Two parabolas resolved when $\Delta\theta_m > \delta$ - Charge resolution geometry. Shown is a set of parabolas.*

3.2.3 Detector System

Many systems can be used for particle detection at the end of TPS. The more important characteristics is the ability of the detector to show the parabolas mark out from the deflected particles. One of the most used is the Micro Channel Plate coupled with Phosphor screen. Micro Channel Plate (MCP) is a specially fabricated plate that amplifies electron signal similar to secondary electron multiplier (SEM). Unlike SEM, MCP has several million independent channels and each channel works as independent electron

multiplier. In other words, one can imagine MCP as an assembly of millions miniature SEMs [44]. MCP consists of a two-dimensional periodic array of very-small diameter glass capillaries (channels) fused together and sliced in a thin plate. A single incident particle (ion, electron, photon etc.) enters a channel and emits an electron from the channel wall. A typical channel of MCP has diameter of about 10 μm. Each channel acts as an independent photomultiplier and parallel electrical contact to each channel is provided by depositing of a metallic coating on the front and rear surface of the MCP, being then the input and output electrodes. When a particle, whatever its nature, hits the channel wall a fraction of its energy is transferred to the electrons in the channel surface. Thus the electrons energy can be enough to be pushed form the channel surface and a current due to secondary emission is formed. The high-voltage applied across the MCP surface produce also a current flowing through the plate surface. The electrons forming this current, called strip current, refill the electron depleted regions of the channel wall for the secondary emission. A scheme of the processes in the channel is provided in Fig.3.14.

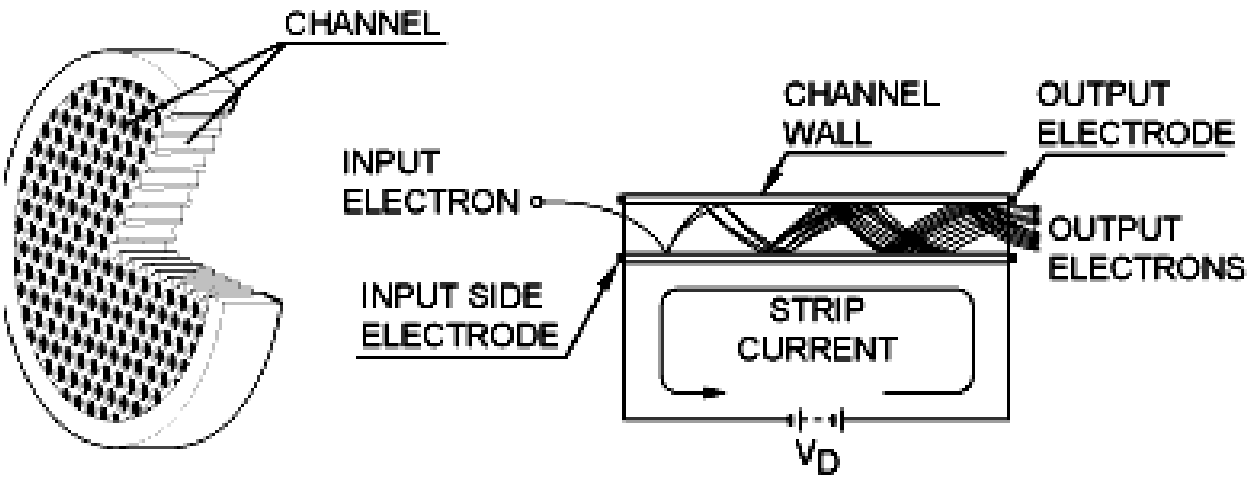

Figure 3.14: *diagram of operation of MCP*

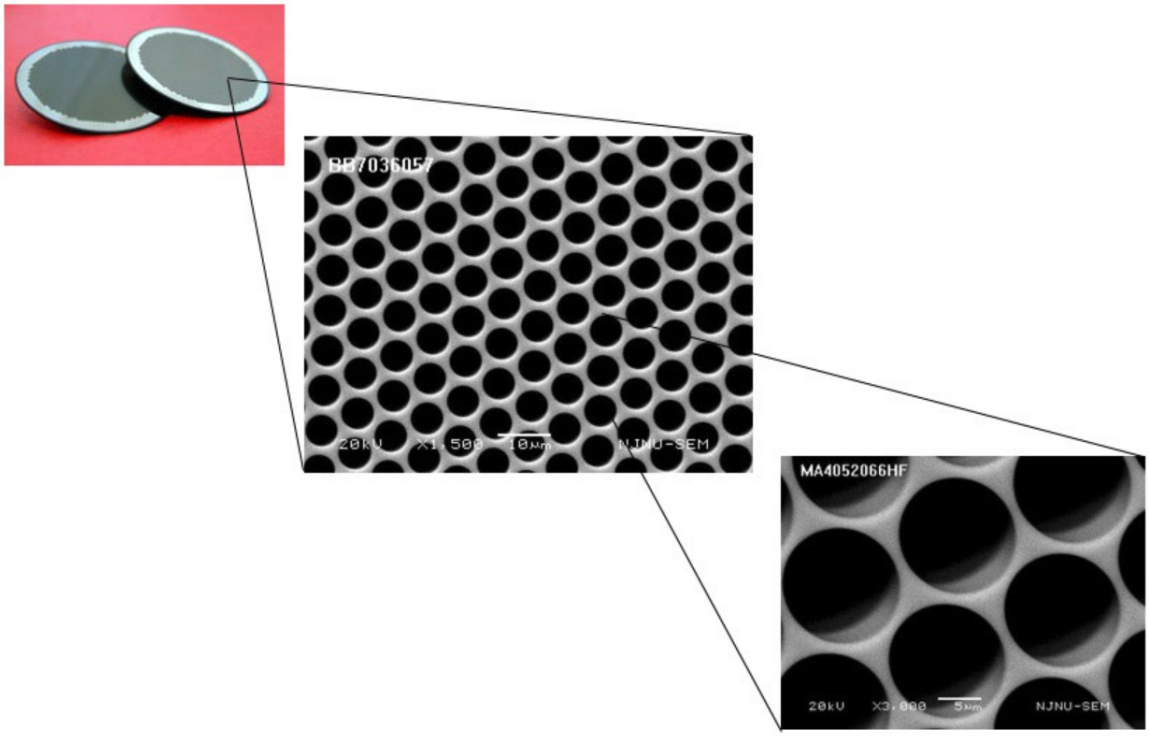

Figure 3.15: *SEM images of MCP*

In Fig.3.15 is shown a SEM picture of MCP, it is possible to observe the input side of channel and is inclination respect the normal direction for increase the interaction probability with the beam. The output electrons are the signal that we need to aquire for the display of parabolas. For this it is possible to use a phosphor screen that permit to record via CCD camera the parabolas for further analysis. The phosphor screen emittes photons if accelerated electrons hit the material. The most common use of phosphor screens are cathode ray tube displays which are used in the early TV's and oscilloscopes. Phosphors for these cathode ray tubes were standardized and designated by the letter "P" followed by a number. The phosphor screen of image intensifiers converts the electron avalance from the micro channel plate back into photons.

Although MCP system is often used as the detector at the rear of the Thomson parabola spectrometer, other kind of detector can be employed in Thomson Parabola

spectrometer for to see the parabolas for example, Gafchromic films, CR39 and Imagin plate. The Gaf Chromic films consists of radio-chromic miceocrystalline dispersion on a thin polyester bulk. Its radiographic sensitivity is based on the solid-state photo-polymerization of diacetylene monomer molecules. The color of film change with the total dose, become darker with the increase of dose [45]. This detector shows many advantages in the detection of particles emitted from plasma laser generated, it is not sensible to the visible light, has a good spatial resolution and does not need of any special development for the lecture. The negative aspect is that the films are off-line detectore, we need to remove the film for make the lecture and change with new one, this means the aperture of vacuum chamber. In addition we need to operate in the same experimental condition because with this detector if we change the target there is overlap of parabola.

Image plate is a reusable film where ionizing radiation (ions, electrons and photons) excite electron levels in the plate [46]. The plate is then scanned in a purpose built scanner which de-excites these levels with a specific wavelength of light and causes light to be emitted that is read by the scanner. Once the plate is fully de-excited it can be reused. For image plate at the back of the Thomson parabola spectrometer the point of zero deflection is marked by x-rays passing along the unobstructed line-of-sight. The image plate is reusable and can have a very large dynamic range, but compared with MCP-phosphor system don't give the possibility to analyse different kind of target because with image plate there is a overlap of all parabola produced from two different de-exitation, instead with MCP you can record every single shot.

We showed the advantages of a device like TPS, among these there is the high adaptability at the experiments, changing B, E and the geometry it is possible use the device in different energetic ranges. We show below three examples in which the spectrometer is designed for three different energetic ranges: high energy, very high energy and low energy (TPS of our laboratory).

3.2.4 Thomson Parabola for high energy plasma

Several experiments were performed at PALS laboratory in Prague (Czech Republic) using the Asterix Iodine laser that was employed for this experiment. Laser operates at 1315 nm wavelength, 700 J maximum pulse energy, 300 ps pulse duration, 70 μm laser spot diameter, 10^{16} W/cm^2 pulse intensity and single pulse mode. Generally with this beam the non-equilibrium charge distribution of the plasma generates high electric fields driving ion acceleration at energies exceeding 1 MeV per charge state. For plasma diagnostics was developed a TPS with two pinholes collimate the ions species accelerated along the normal to the target surface; the first has 1 mm diameter and the second, placed at 10 cm distance from the first, has 100 μm diameter. This second pinhole is located at a distance of 5mm with respect to the magnet. A magnetic field of 0.06- 0.12 T and a parallel electric field at 0.5-1.4 kV/cm have been applied orthogonally to the direction of the incident ions. Charged particles are deflected by electrostatic and magnetic fields towards the multi-channel plate (MCP) fixed at a distance of 16.5 cm from the electrostatic plates.

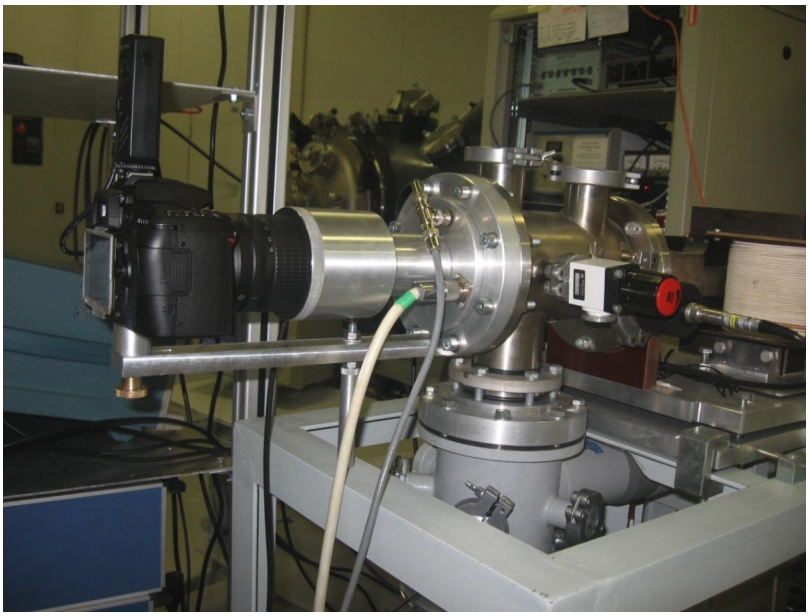

Figure 3.16: *Picture of TPS of PALS laboratory in Prague*

Fig.3.17a reports a typical TPS spectrum obtained by irradiating 6μm thin PE target with 590 J pulse energy [47]. The spectrum shows a circular zone where photons and neutral particles arrive on MCP and a lot of parabolas outgoing from this circle. Fig.3.17b shows the conversion of the experimental spectrum in gray scale levels and the simulation data (lines) overlapped to the experimental one, the simulated and experimental data were obtained with $B = 0.02T$,$V = 2.4kV$, in this case the simulation was make using the Opera 3D/ TOSCA code.

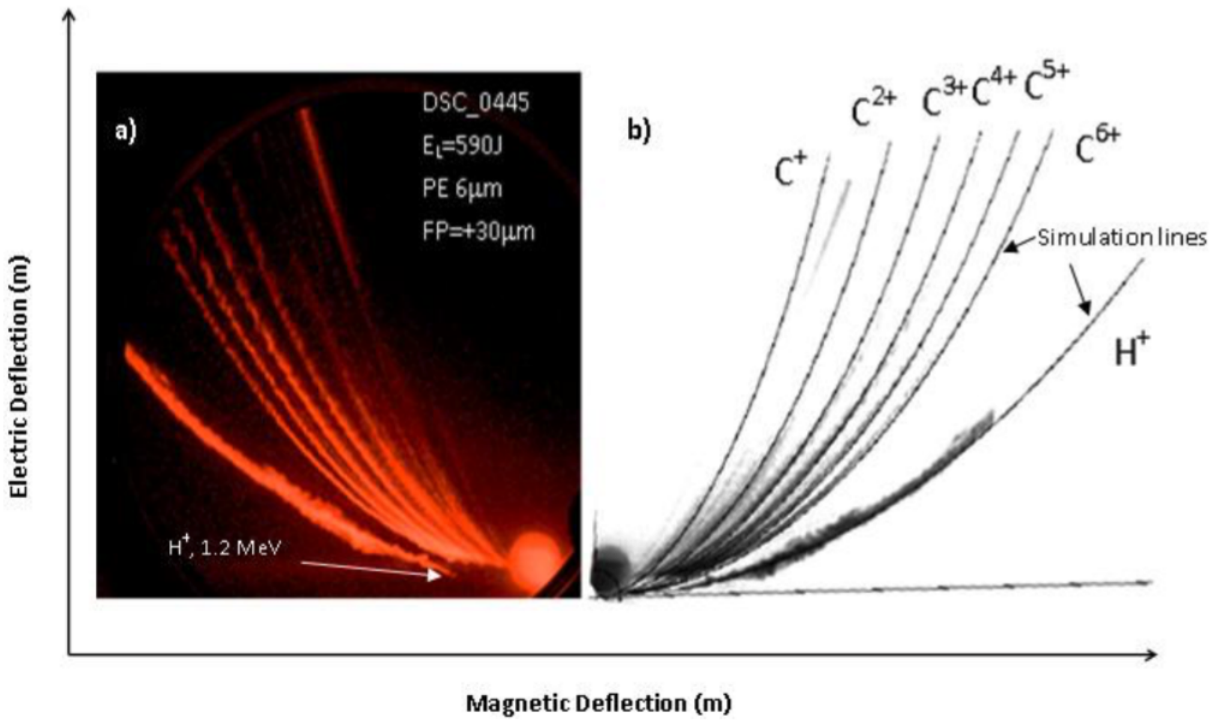

Figure 3.17: *Experimental parabolas from a 6 μm PE irradiation at 590 J (a), and spectra transformation in gray scale with identification of the different parabolas (b)*

The distance between the protons parabola and the centre circle is compatible with a proton maximum energy of 1.2 MeV. The brightness of parabola are proportional to the number of particles, with a analysis software it is possible to plot the intensity as a function of particle energy.

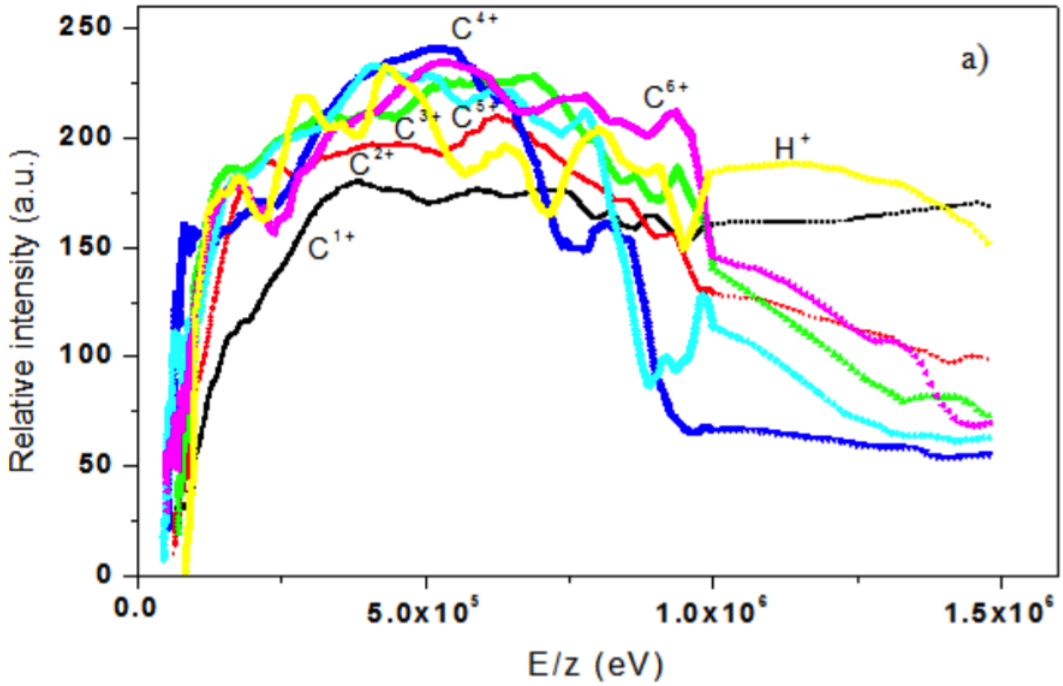

Figure 3.18: *Experimental parabolas from a 6 μm PE irradiation at 590 J (a), and spectra transformation in gray scale with identification of the different parabolas (b)*

Figure 3.18 [47]shows the ion energy distributions with, as a first approximation, Boltzmann-like shapes. Protons reach the energy of 1.5 MeV while carbon ions reach the energies of 900 keV, 1.8 MeV, 2.7 MeV, 3.6 MeV, 5 MeV and 6 MeV for the charge states C^{1+},C^{2+},C^{3+},C^{4+},C^{5+} and C^{6+}, respectively. Thus in average an acceleration of about 1 MeV/charge sate is obtained.

3.2.5 Thomson Parabola for very high energy plasma

In this section is described the design of a TP detector entirely developed at INFN-LNS. The TP-LNS with the wide acceptance of its deflection sector and its fields tunability have a working range up to 40 MeV for proton and 1.2 AMeV/z. The collimation system consist of 2 pinholes with diameter of 1 mm for the closest to the target and 100μ m closest to the detector. In the deflection sector an electric (7.0 cm long) and a magnetic (15.0 cm long)

field, partially overlapping with each other are applied. The magnetic field is generated by an electromagnet composed by two resistive coils and the maximum magnetic field intensity is 2500 gauss. The electric field is generated by two copper electrodes 7.0 cm long and with a gap of 19 mm, it can be tuned up to 30 kV over the electrodes distance. This configuration if showed in Fig.3.19

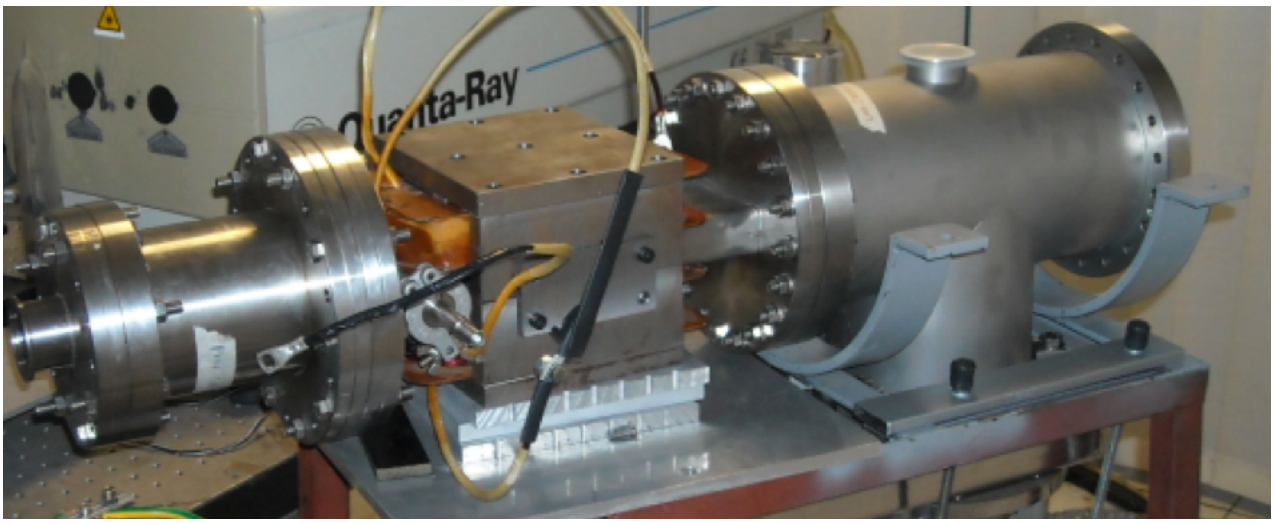

Figure 3.19: *Pictures of TPS-LNS*

In Fig.3.20 (right side) is showed a spectrum obtained irradiated Al + Mylar (50 nm+2.5 μm) with 472 J of laser energy, using B = 0.01135 T and E = 100.0 kV/m. On the left side of picture is reported the simulation make using the experimental parameters and MATLAB software code.

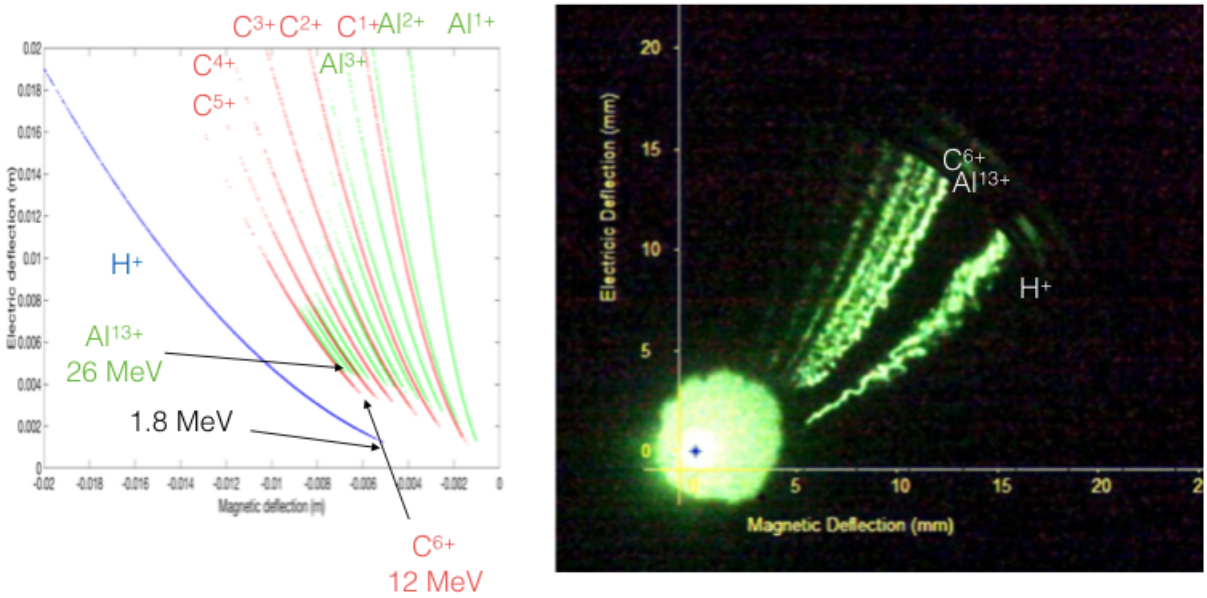

Figure 3.20: *Simulation of TPS using the experimental setup, in blu are plotted the protons, in green the Al ions and in red the C ions (left side), experimental result obtained irradiate Mylar+Al at PALS laboratory with 472 J of laser energy (right side)*

For to confirm the quality of simulation we overlap the experimental and simulated results. How it is possible to observe in Fig.3.21 the simulation follow very good the line for protons and 3 charge state of Al and C but the resution does not allow to resolve from Al and C. From the simulation we can calculate also the maximum proton energy that result about 1.8 MeV.

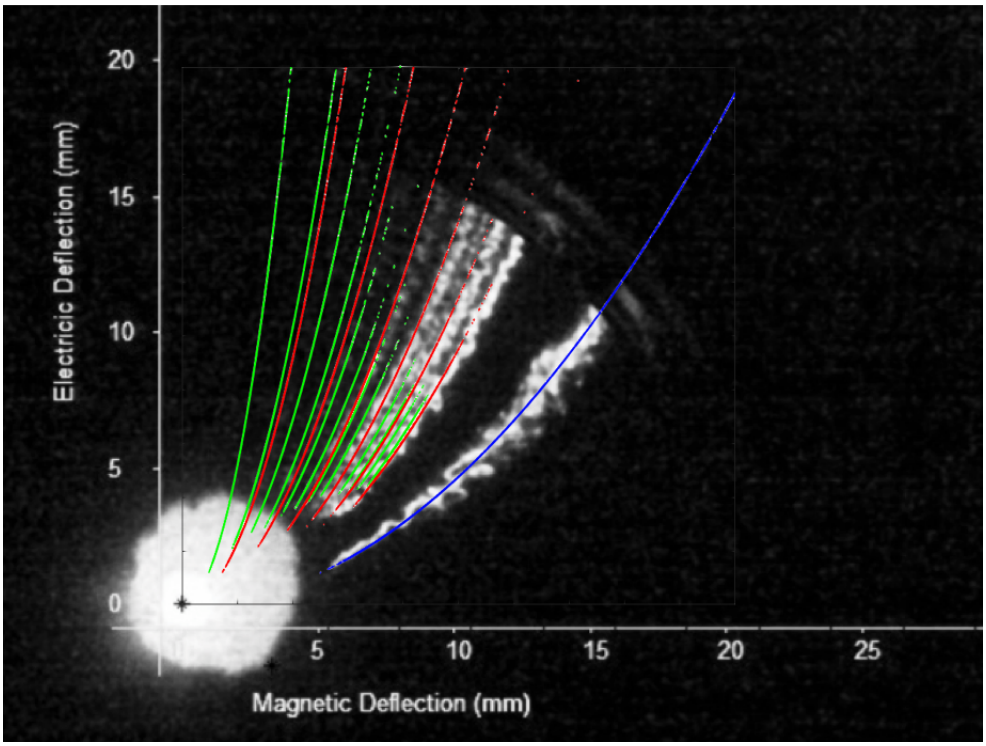

Figure 3.21: *Overlap of simulated parabolas and experimental results*

3.2.6 Thomson Parabola for low energy plasma

With the purpose to obtain a TPS in low energy plasma range and able to be adapted at many different setup, we assembled a TP with permanent magnetic field and variable electric field, with the possibility to change the position of all components of spectrometer. Our TP has been designed for analyze ions in the energy range of 1 keV − 30 keV per charge state using fixed magnetic field of 0.3 T and variable electric field of about 1.5 kV/cm. The advantageous features are the relative small dimensions of the system (that permit a simple alignment and the easy transport) and the possibility to move the position of the elements which assemble the setup in order to prepare the instrument in the best possible configuration for the energy that will be analyzed.

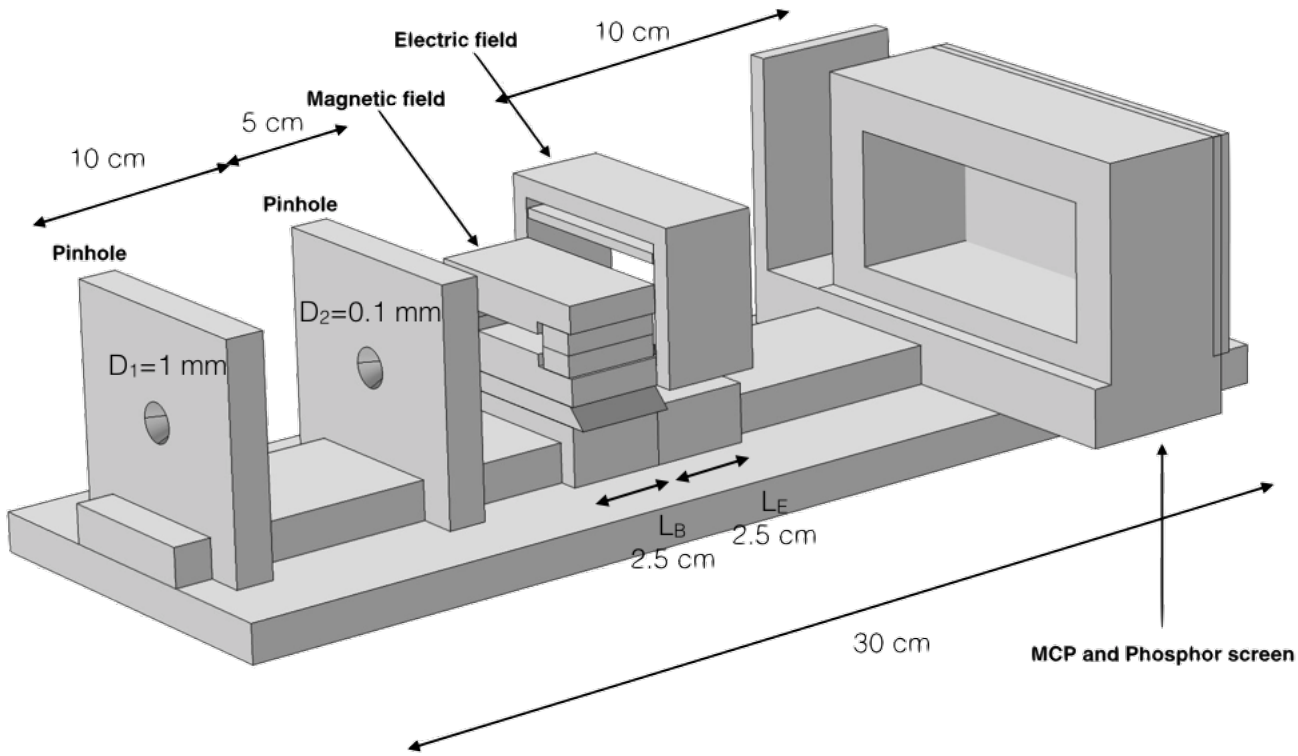

Figure 3.22: *3D schema of TPS*

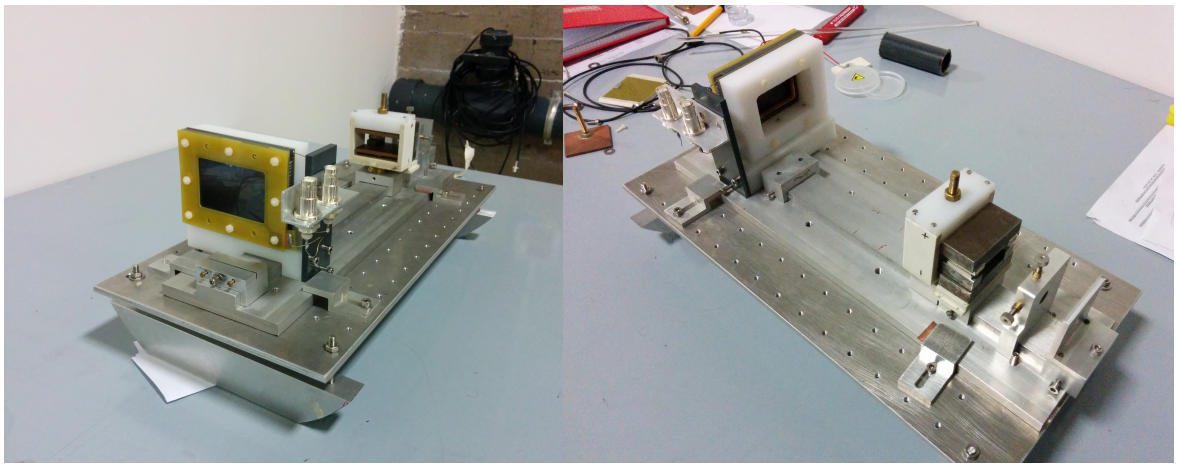

Figure 3.23: *Pictures of TP spectrometers*

It is possible to observe in more details the setup in Fig.3.22. The setup showed in Fig.3.22 has the possibility to change the relative distance between the components of TP, in this way it is possible to arrange the setup in the best configuration for the beam to be analyzed.

In this way we can use the position of pinholes for improve the resolution of system. For understand the best configuration we performed simulations using different diameters and distance from the pinholes. We simulated a beam of Al with energy distribution from 0 up to 2.5 keV per charge state. With charge state from 1+ up to 3+.

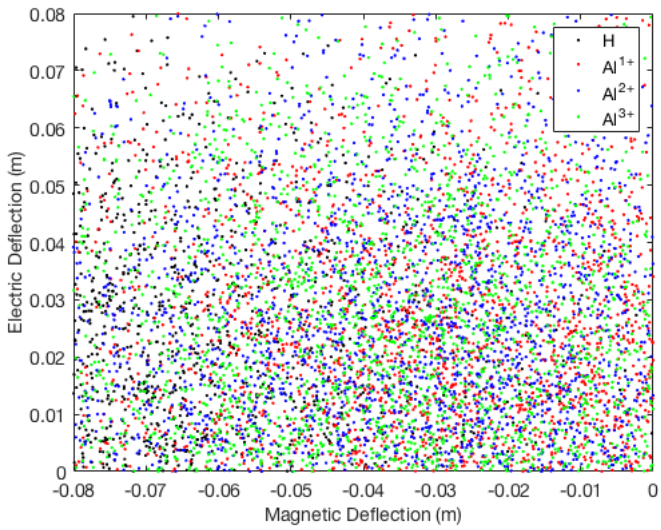

Figure 3.24: *Simulation of Al beam in TPS without collimation system*

In Fig.3.24 is showed the detector simulated in the case in which there isn't collimation systems. This is important to understand the fundalment role on collimation in TP system, in fact in this situation are impossible to resolve the parabola and the single charge state. If we introduce the collimator system, like two pinholes we can use the Eq.3.2.5 for the implementation of simulation code and introduce the collimators effects. In Fig.3.25 are showed 4 situation, in d) we can see the ideal situation in which the beam is unidirectional without space spread. In a) are showed a system in which there are 2

pinholes of 1 mm distant from each other 9 cm, in b) the same distance between the pinholes but with different diameters of 1 mm and 100 μ m, and in c) the same pinholes of b) but with the distance of 18 cm. These results shown like the distance and diameters of pinholes are very important in the resolution of parabolas.

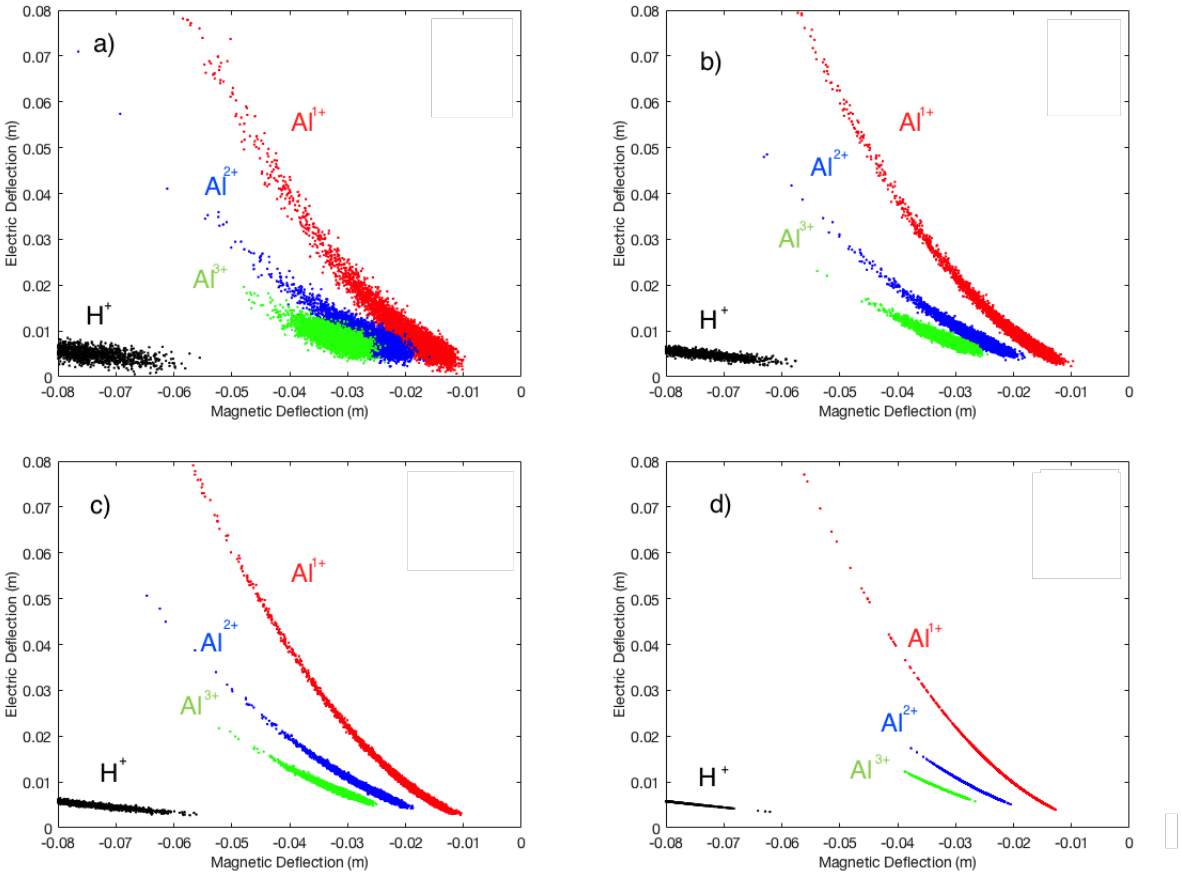

Figure 3.25: *Simulation of TPS with different collimator configurations*

3.2.7 Post Acceleration System

In this section will be described the coupled of TPS with post acceleration system. This because extractor systems geometry must be employed to couple Laser Ion Source with the first stage of post acceleration and for this the TPS can be a good information about beam. The post accelerated ions are characterized by multi-energetic energy distributions.

The accelerating set-up consists of a close plasma expansion chamber of aluminium, with a parallelepiped shape (26 cm length and 11 cm side square base). At the centre of the parallelepiped chamber is placed the target. A lateral input hole permits to the laser to incoming and to hit the target. The target and the expansion chamber are placed at the same electrical potential, that can be set between 0 and +30 kV by a power high voltage supply. The base of the extraction chamber is placed on an insulator base to insulate the extraction to the vacuum chamber. A lateral hole permits the laser-target interaction and the geometry don't limit the possibility of mouvement of target. The frontal side respect the target are totally open and in front of it, 12 discs 2 mm tick and 10 cm diameter, are aligned to the axe of chamber. Each disc has a central hole of 8 mm in diameter and are all connected on the other one by a resistor of 10 MΩ, in this way the first disc is connected directly with the high voltage and the last one with the ground [48].

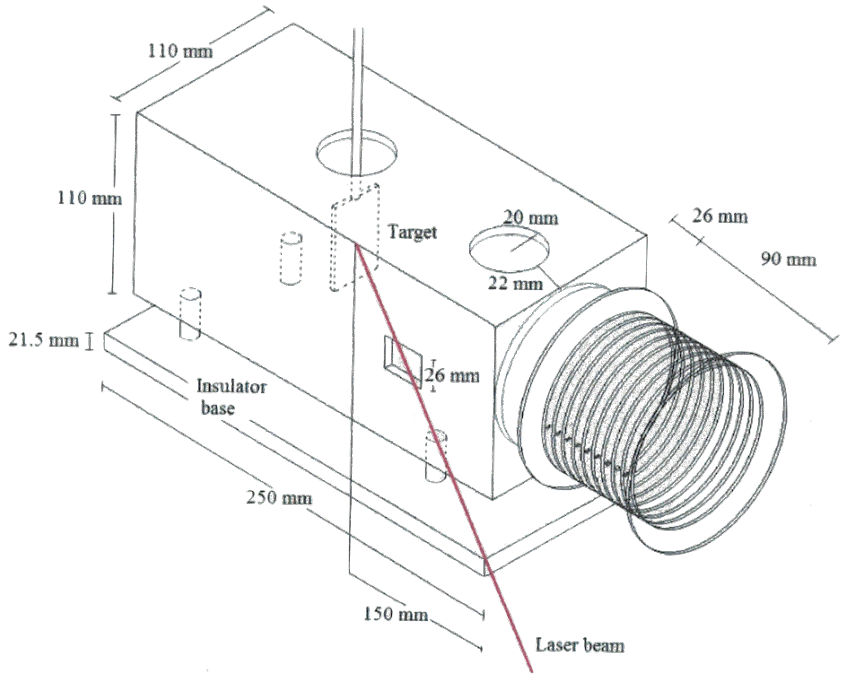

Figure 3.26: *Schema of post acceleration system*

The post acceleration can be coupled with TPS in the case of to low energy plasma.

This can be possible to analyse the charge state. In Fig.3.27 are shown the simulated dots that corrispond to different voltages of acceleration from 5 kV up to 25 kV, with 5 kV of step.

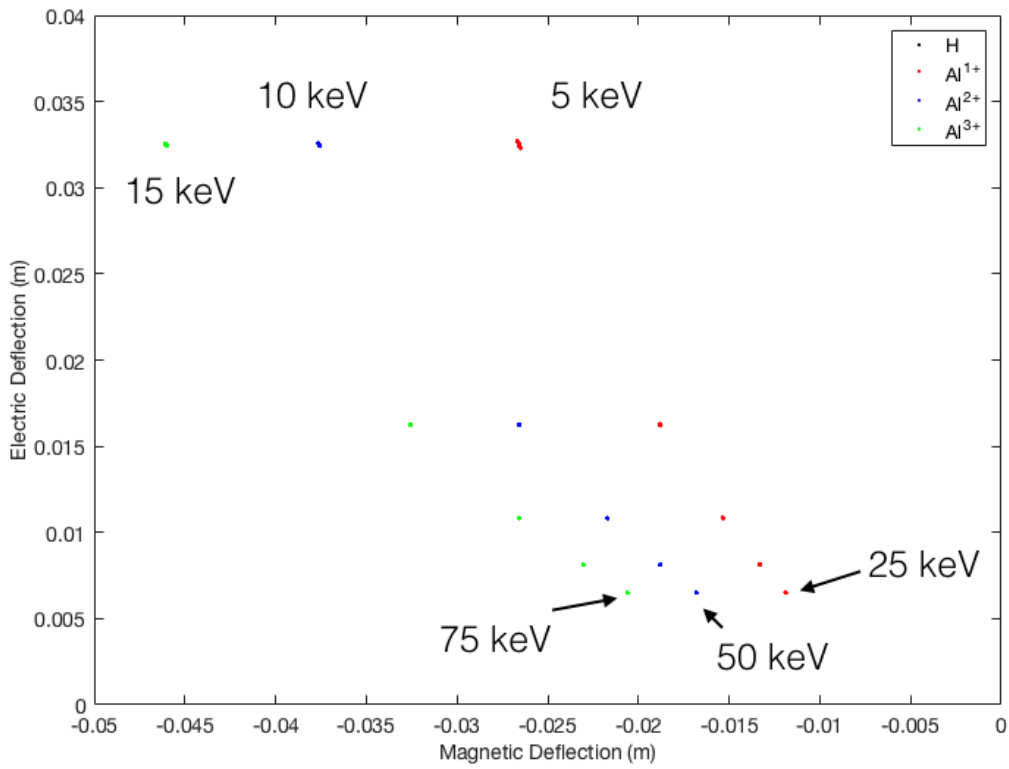

Figure 3.27: *Simulation of TPS coupled with post acceleration for Al target with different voltages of acceleration*

Now we want report the simulated results that we can obtain using the Nd:YAG laser of LNS, with 800 mJ, 9 ns per pulse, with an intensity of $10^{11} W/cm^2$. From many experiences we know that in these conditions an irradiated target of Ta produces plasma with charge state from 1+ up to 10+ with 1 keV of energy per charge state. Using the TPS for low energy with an electric field of $5kV/m$ and a magnetic field of $0.3T$ we obtain the parabolas shown in Fig.3.28. If the same target is irradiated with 30 kV of post acceleration we need to increase the electric field up to a magnitude of $300kV/m$ and the

result is shown in Fig.3.29.

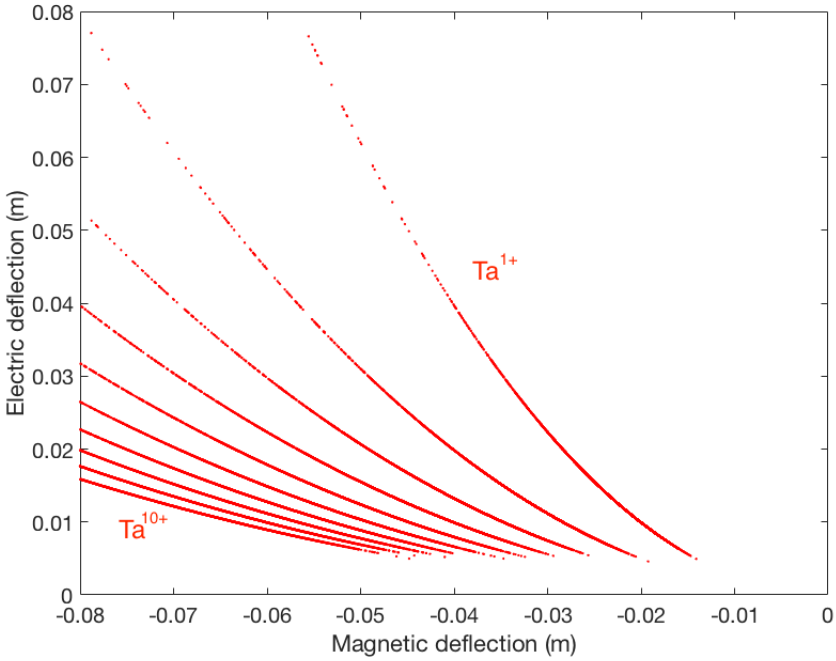

Figure 3.28: *Simulation of TPS coupled without post acceleration of a plasma of Ta*

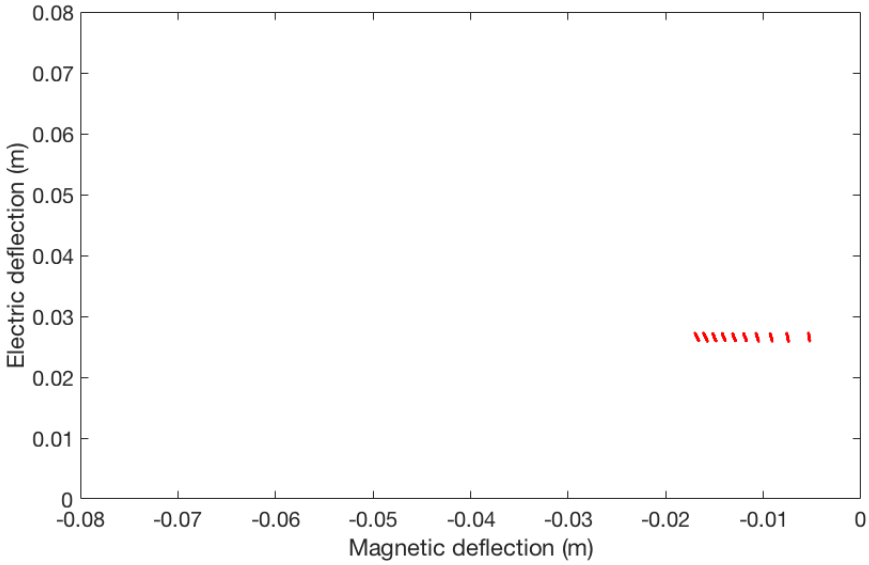

Figure 3.29: *Simulation of TPS coupled with post acceleration of a plasma of Ta*

How we can observe Fig.3.29 shows only 10 dots due to the 10 charge states of Ta without the energetic spread, thanks the presence of post acceleration system. But the simulation suggest to change the setup when we put the post acceleration becaus can be difficult to read the spectra in this way, instead changing the distance we can use all available screen.

3.3 Magnetic Mass Spectrometer

Particles deflection due to the use of magnetic fields may have several applications. In previously paragraph we showed its utility coupled with eletric field in Thomson Parabola Spectrometer. In this paragraph the target is to show how can be used alone for the particles diagnostic. Several beam analisys tecnique use the magnetic deflection because it separates the particles for velocity or mass or charge state. When a singly charged particle of energy E and charge q enters a uniform magnetic field B oriented transversely to the particle trajectory, it experiences the deflecting Lorentz force $F_L = qvB$, which is

counterbalanced by the centrifugal force $F_c = mv^2/r$, where v is the particle velocity and m its mass:

$$\frac{mv^2}{r} = qvB \qquad \frac{mv}{r} = qB \tag{3.3.1}$$

from which we get the radius of the circular trajectory

$$r = \frac{mv}{qB} \tag{3.3.2}$$

Fastening the velocity, the particles with different m/q ratio will travel follow different trajectory. This can be used in different ways for beam analisys. A possible configuration can be the follow shown in Fig.3.34

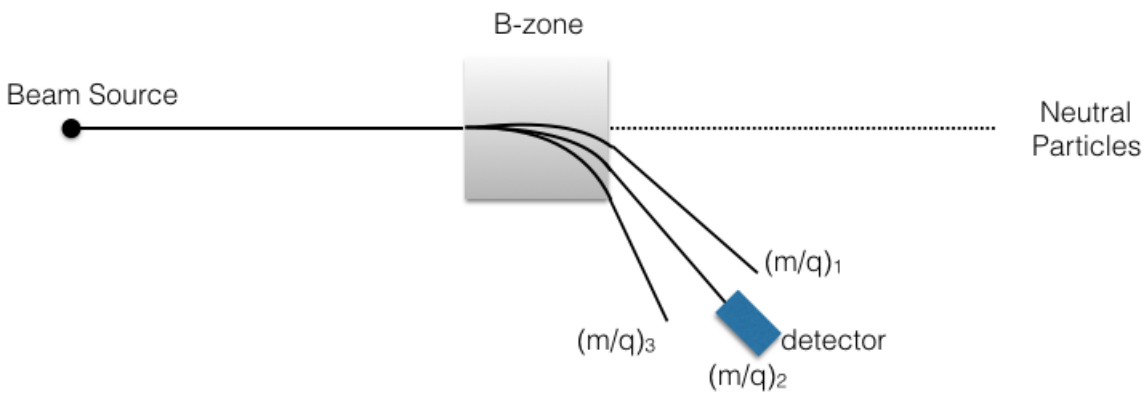

Figure 3.30: *Example of magnetic spectrometer*

Where like detector we can put or Faraday Cup, SiC detector, or others time of flight detectors. In this kind of setup we need to consider a magnetic field that separe the particles in mass-charge state ratio but only one of these reach the detector, the only one that has the right ratio. In this way the magnetic field is a filter. Changing the field it is possible to analyze all charge state and possible energy spred of the same because with the same m/q ratio the particles can be deflected in different way for the energy. This configuration anyway is usefull with continous beam and has very big limitation for plasma produced by laser because should be need a very big number of shot only for the analisys of a charge state considering the energy spred. To overcome this limitation we

thinked a different configuration in which the field is fixed, but there is the presence of multi detector at different angle.

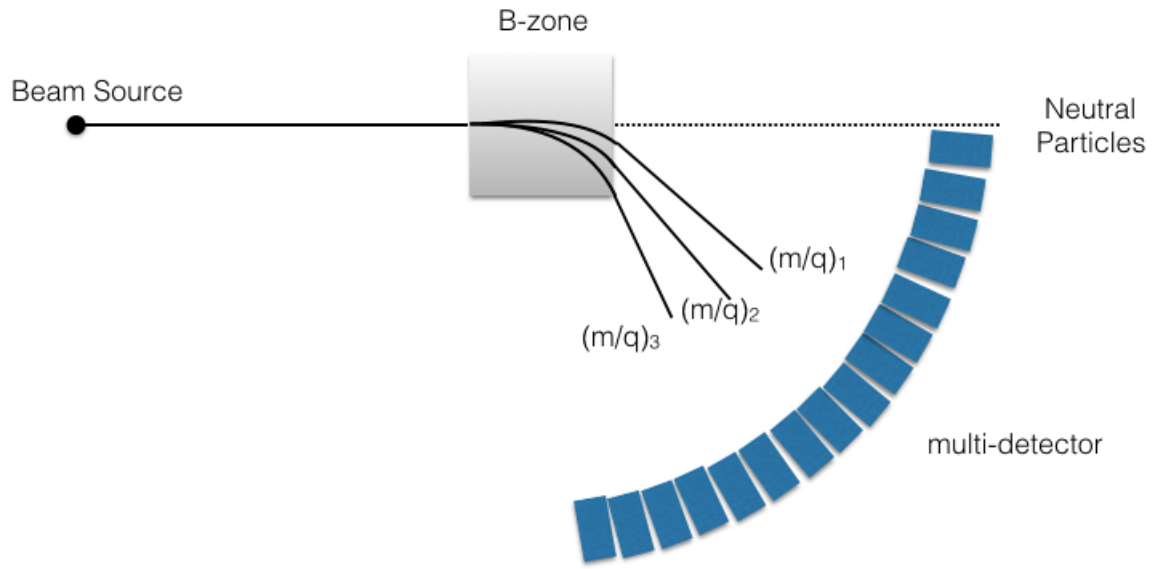

Figure 3.31: *Multi Faraday Cup system*

In this way with a single pulse should be possible to study the complete distribution from 0 to 90 of deflected plasma, obtaining information about the charge state and the energetic distribution. Of course the same setup can be used both for ions and electrons changing the magnitude of magnetic field. In Fig.3.32 is shown a vacuum chamber projected for this kind of experiments in which the plasma should be deflected by magnetic field at the enter of chamber and detected on the Faraday Cup present on the edge of the chamber or within the same. The choise of magnetic field as a function of ion energy permits to study several range of energy and particle, from electrons to protons up to very heavy ions like gold. The first step for the plasma diagnostics using this setup is the simulation of plasma in the magnetic field, this is a very important step because it allows to understand the necessary magnetic field to deflect the particles.

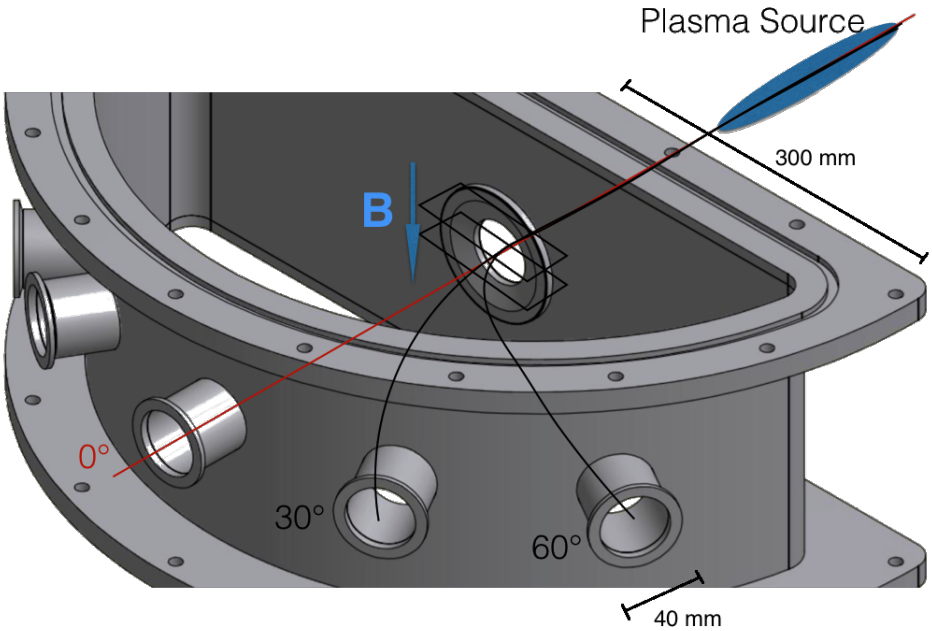

Figure 3.32: *Vacuum chamber for plasma mass spectrometry*

Figure 3.33: *Internal part of vacuum chamber*

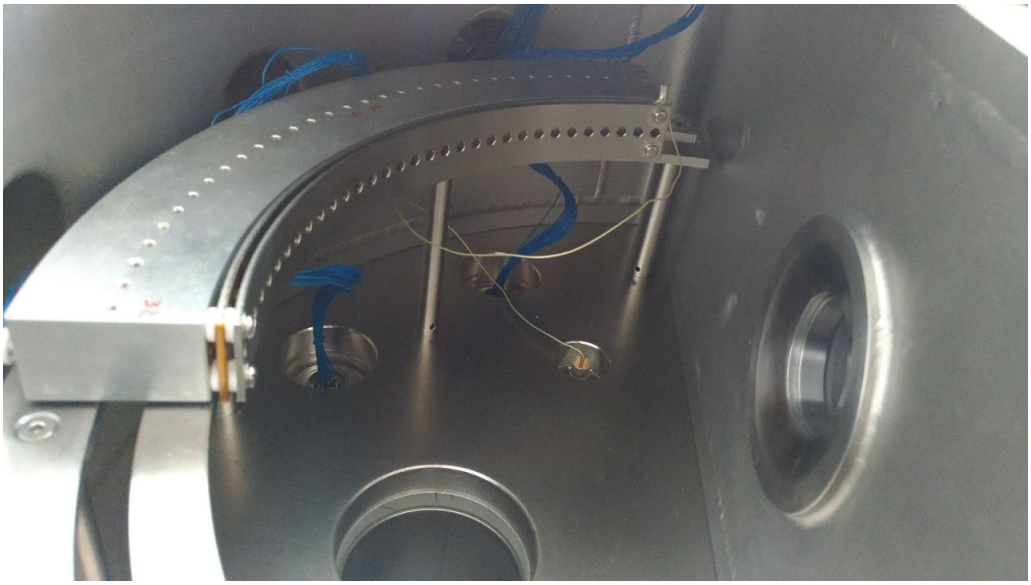

Figure 3.34: *Detail of multi Faraday Cup system*

In Fig.3.33 and 3.34 it is possible to observe in details the internal part of vacuum chamber. It is seen that there is a slide which allows the lease of a system that contains 32 Faraday cups that can cover angles from 0° (normal direction) up to 90°. When we use deflection system it is very important to understand the effect of collimation on the system. For this magnetic spectrometer it is possible to insert collimators before the magnetic field. The Fig.3.35 shows simulations makes with MatLab that shown different situation for collimation system.

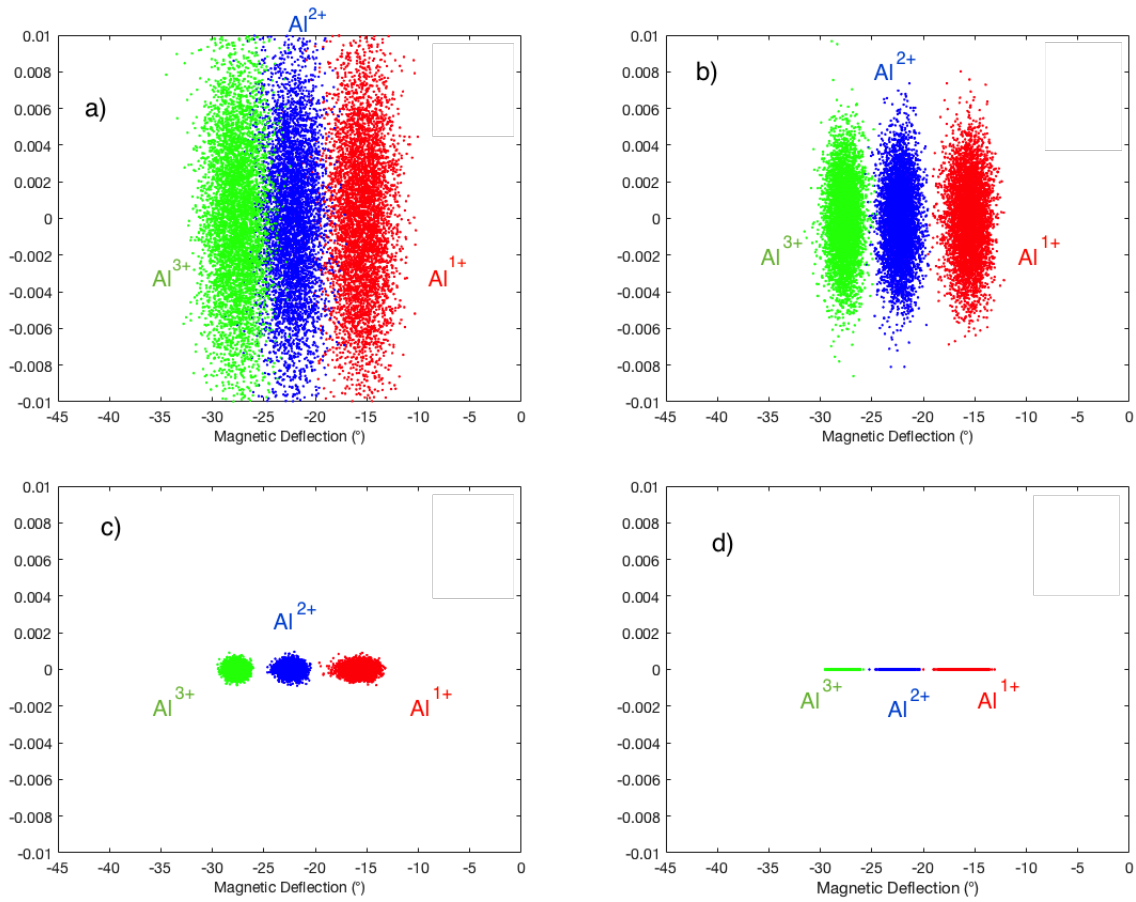

Figure 3.35: *Simulation of Al beam with several collimation configuration*

In particular in a) we can observe the situation in which there isn't collimator before magnetic sector. The geometrical spread of particles are very important major in vertical direction instead if we observe the deflection in angle the energetic spread permit the diffusion of particles at very large angle. In d) we can see instead a simulation of the ideal case in which the beam is unidirectional without space spread. The situations shown in b) and c) represents two configurations of different collimations. In b) we have a configuration with 2 pinholes of 3 mm of diameter distant from each other 30 cm, in c) we have the same position of pinholes but differents diamaters, the closest to the target 1 mm and the farthest 100 μm.

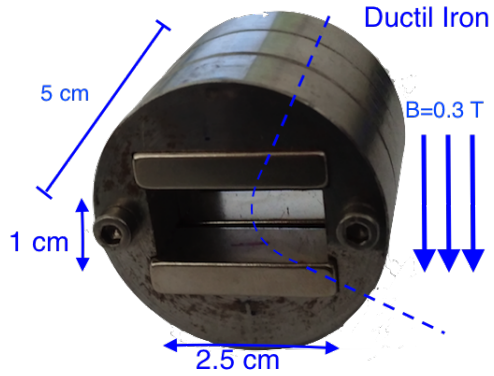

Figure 3.36: *Permanent magnets used for ions deflection*

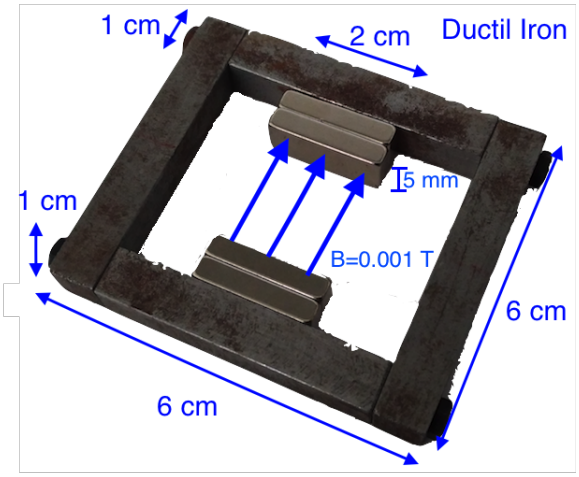

Figure 3.37: *Permanent magnets used for electrons deflection*

Fig.3.36 and Fig.3.37 show the permanent magnets used for the deflection of ions and electrons with magnitude of 0.3 T and 0.001 T, respectively. In addition to a difference of magnitude there is a difference in the length of magnets, for what concern the magnet for ions, it consist of 3 parts that can be combined up to the length of 5 cm, instead for electrons we have a single section of 1 cm.

3.3.1 Angular distribution measurements

The assembled setup like said before has many advantages and applications. Using it we obtained the angular distribution of plasma for a light element, aluminium, and for a heavy element, tantalium with and without magnetic field. All Faraday cups were placed at 1 m of distance from the target. In Fig.3.38 it is possible to observe the detail of one of these Faraday cups pulled out of the slide.

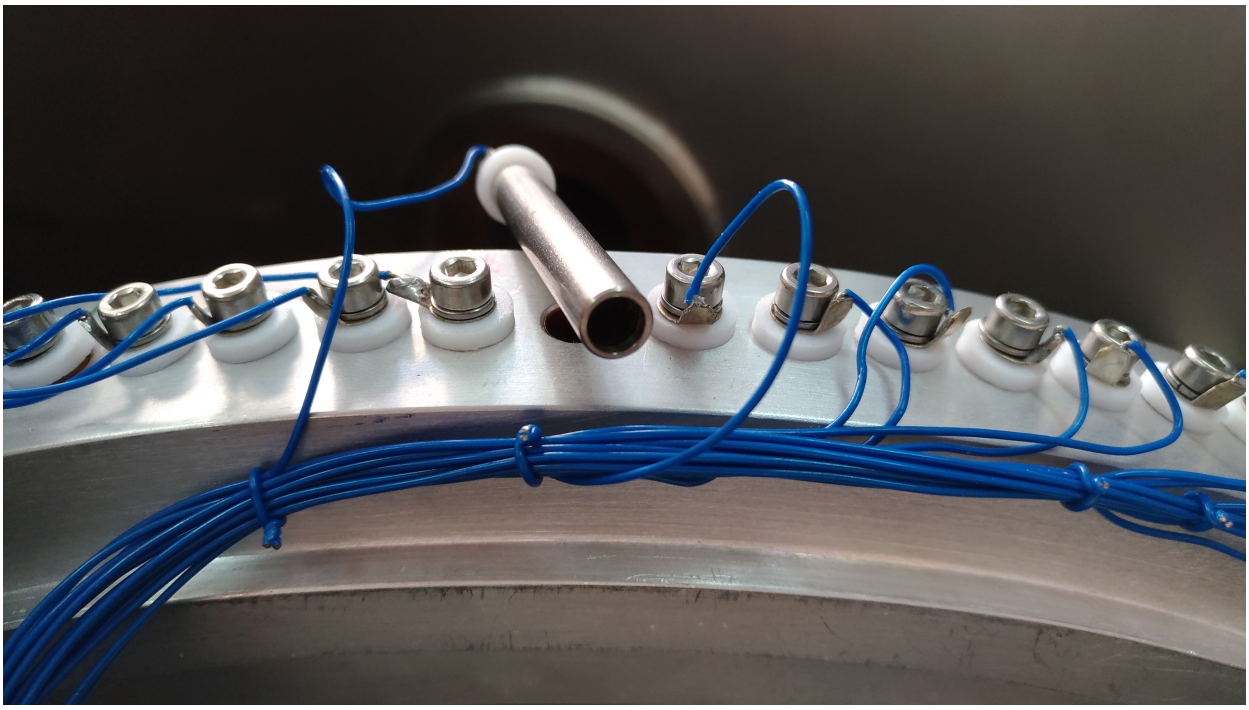

Figure 3.38: *Faraday cup of spectrometer*

Of we can see in Fig.3.39 the design is very compact for a total lenght of 4 cm, and the little aperture allow to put many faraday cup in order to cover all position with high angular resolution.

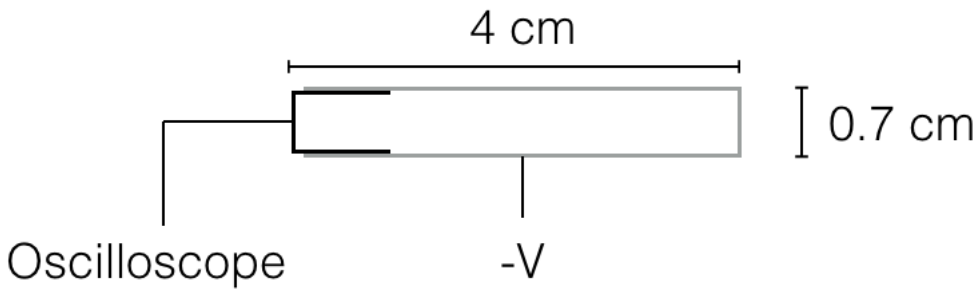

Figure 3.39: *Schema of Faraday cup of spectrometer*

First we perform an experiments without magnetic field for the determination of natural angular distribution of plasma. In Fig.3.40 there is a schema for shows the position of FCs used respect the plasma propagation. Because there isn't the magnetic field we choise to use a configuration that permits to analyse angles from $-45°$ up to $+45°$. Using the experimental setup shown in the Fig.3.40 have been performed time of flight measurements with all FC and for all was recorder the value of yield and energy. Plotting the yield as a function of FC (each position corrispond to an angle) it is possible to make a plot of angular distribution of plasma yield. This is reported in Fig.3.41 for Ta and for Al. Like is showed for Al we have an angular aperture of $\pm$ 10° while for Ta $\pm$ 8°. The results shown, like reported in literature [49]-[50], the plasma produced by high atomic number target are very narrow in angle distribution [51], instead low atomic number target produces larger distribution.

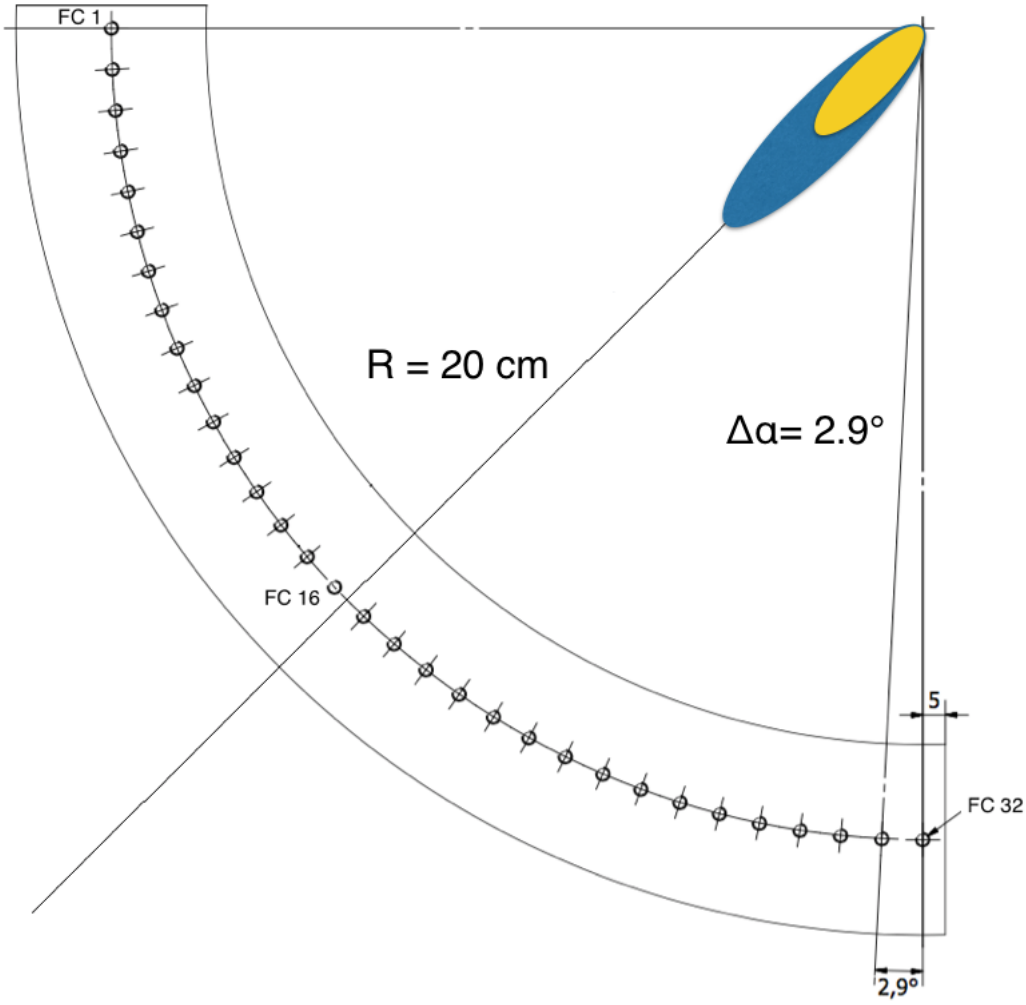

Figure 3.40: *Experimental setup used for angular distribution measurement without magnetic field*

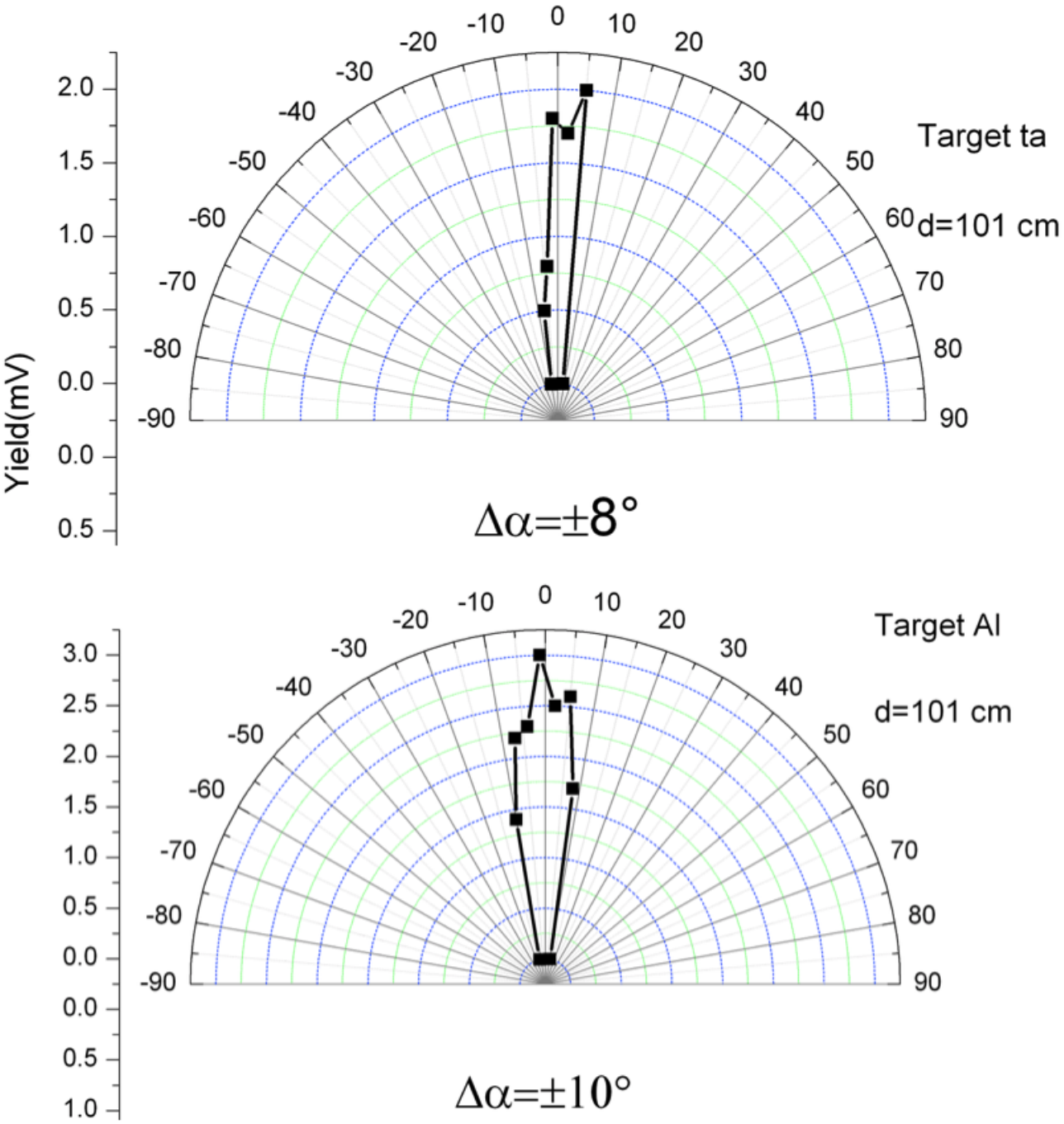

Figure 3.41: *Angular distribution for a plasma produced irradiating Ta target with* $10^9 W/cm^2$ *laser intensity*

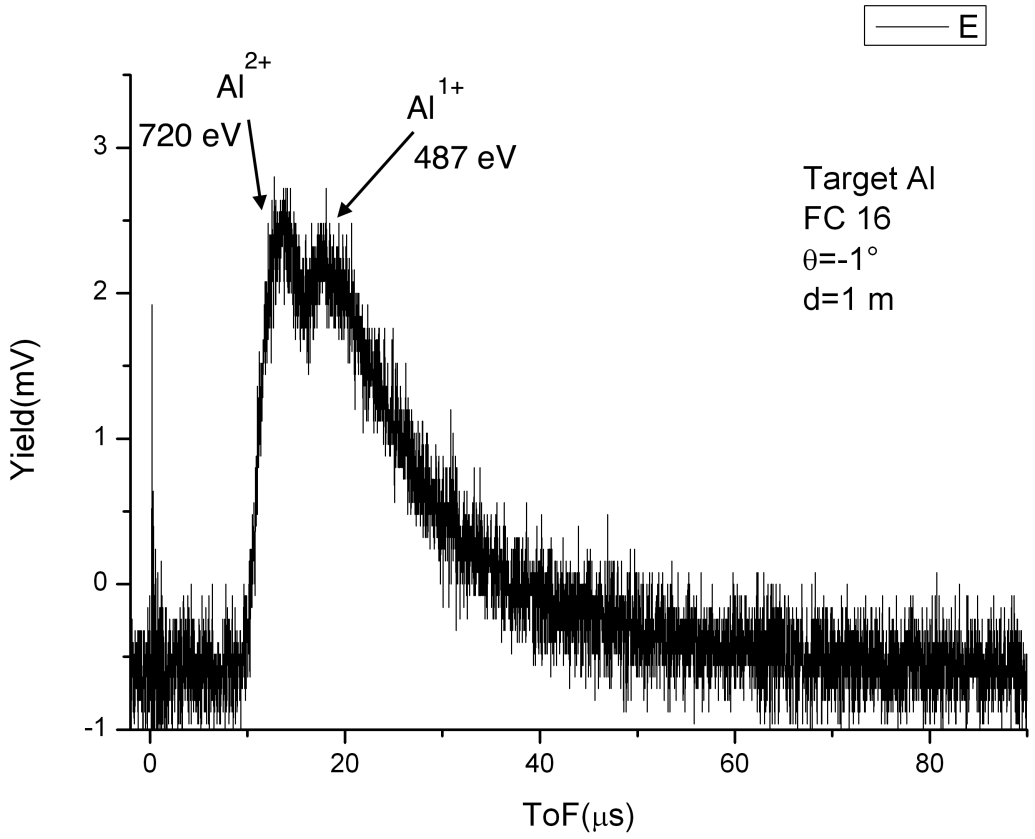

Figure 3.42: *ToF spectra along the normal direction*

The graph shown in Fig.3.42 represent one of the time of flight spectra used for making the angular distribution of plasma. In particular this is the spectra obtained in normal direction and we obtained a yield value of 2.4 mV. The plasma yield should be measured up to the signal of FC become zero like in Fig.3.43.

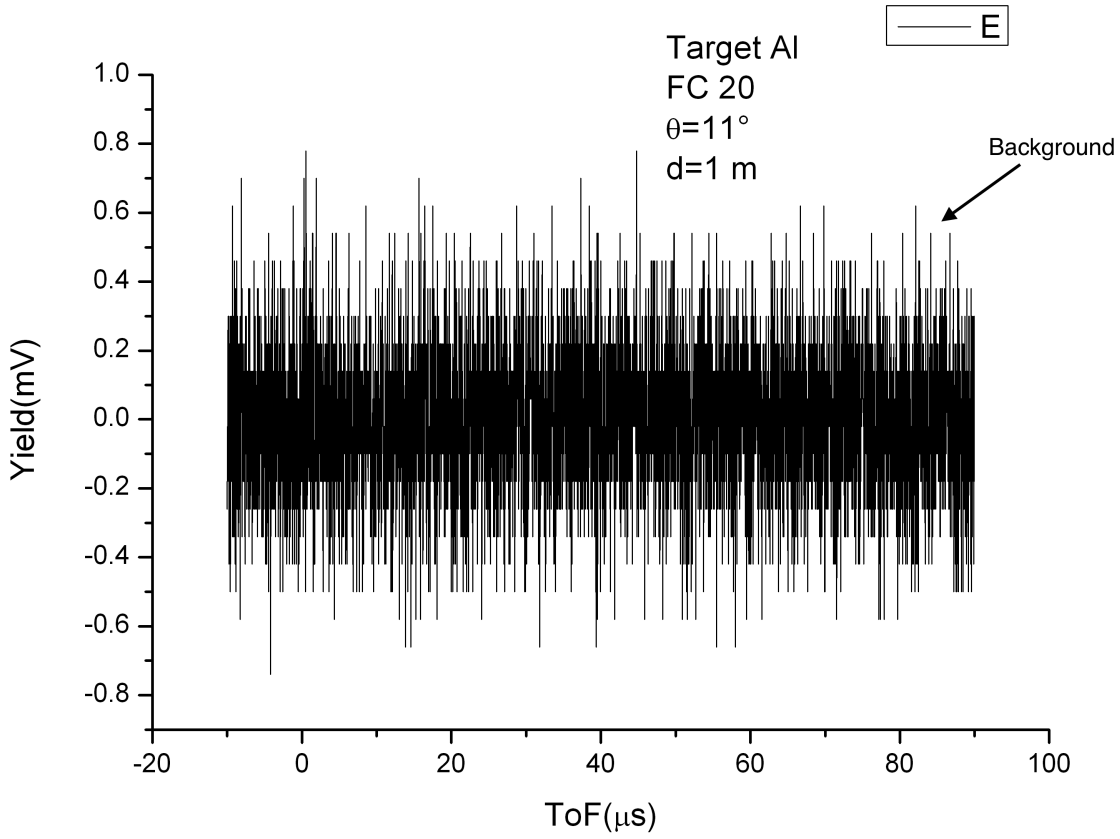

Figure 3.43: *ToF spectra show the background signal at* 11°

After these measurements were performed the experiments using the magnetic field for ion deflection. With the insertion of the magnet the first thing that can be observe is that the signal is present up to 50° for Al and up to 35° for Ta. This is because the field allows at high charge state ions to be deflected at very high angles. To confirm this were performed measurements also at symmetric angles in order to verify the absence of signals. In both graphs for Al and Ta it is possible to observe the presence of peaks at particular positions that corrispond to the center of the single distribution for each charge state.

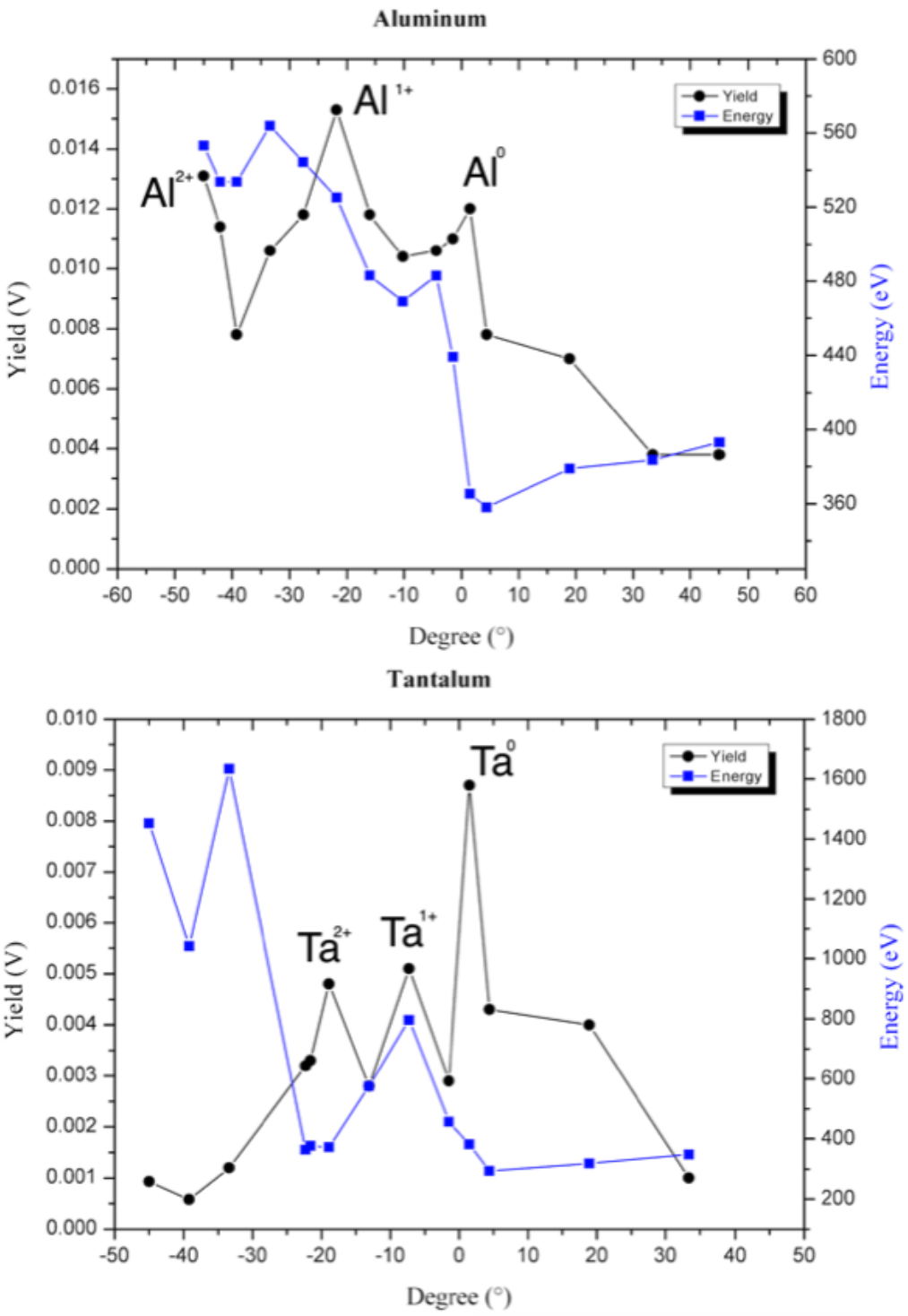

Figure 3.44: *Angular Distribution results*

Chapter 4

Coated Targets investigation with IEA

When an high intensity laser interacts with a target and take place the laser ablation, the material isn't totaly converted in plasma, a part can become low temperature plasma or neutralize and become vapor. In order to investigate phenomena like the plasma production and the characteristics of produced plasma, we studied the production of plasma irradiating Al target covered with different thicknesses of Au, in this way we can studied the properties of plasma as a function of gold thickness. In addition we used different laser intensities irradiating the targets with Nd:YAG lasers of 10^{12} and $10^{10} W/cm^2$ in Brookhaven National Laboratory (BNL) and in Laser-Plasma laboratory of University of Messina, respectively. In this way we can observe the differences in the results like a function of laser intensity. The main emploied diagnostics were the Ion Energy Analyser and Faraday Cup described in previous chapters.

4.1 Au coated Al targets

The targets consist of Al pure bulk with 1 mm in thickness, on whose surface the gold was evaporated to obtain a thin film. To make evaporation we inserts aluminum into a holder placed on a melting pot at 29 cm of distance from target. The gold will be evaporated thanks to the heating produced by an electric current of 165 A. The thickness is

measured using a quartz detector that vibrates at the frequency of 5 MHz. The deposited gold on the sensor surface changes the frequency of vibration and a calibrated system we can read the thickness in Å. The key concept behind this type of measurement and control is that an oscillator crystal can be suitably mounted inside the vacuum chamber to receive deposition in real time and be affected by it in a measurable way. Specifically the oscillation frequency will drop as the crystal's mass is increased by the material being deposited on it. To complete the measurement system, an electronic instrument continuously reads the frequency and performs appropriate mathematical functions to convert that frequency data to thickness data, both instantaneous rate and cumulated thickness. All system are placed in vacuum at the pressure of $3 \cdot 10^{-6} mbar$. The prepared targets have thicknesses of 125 nm, 250 nm, 400 nm, 500 nm and 750 nm.

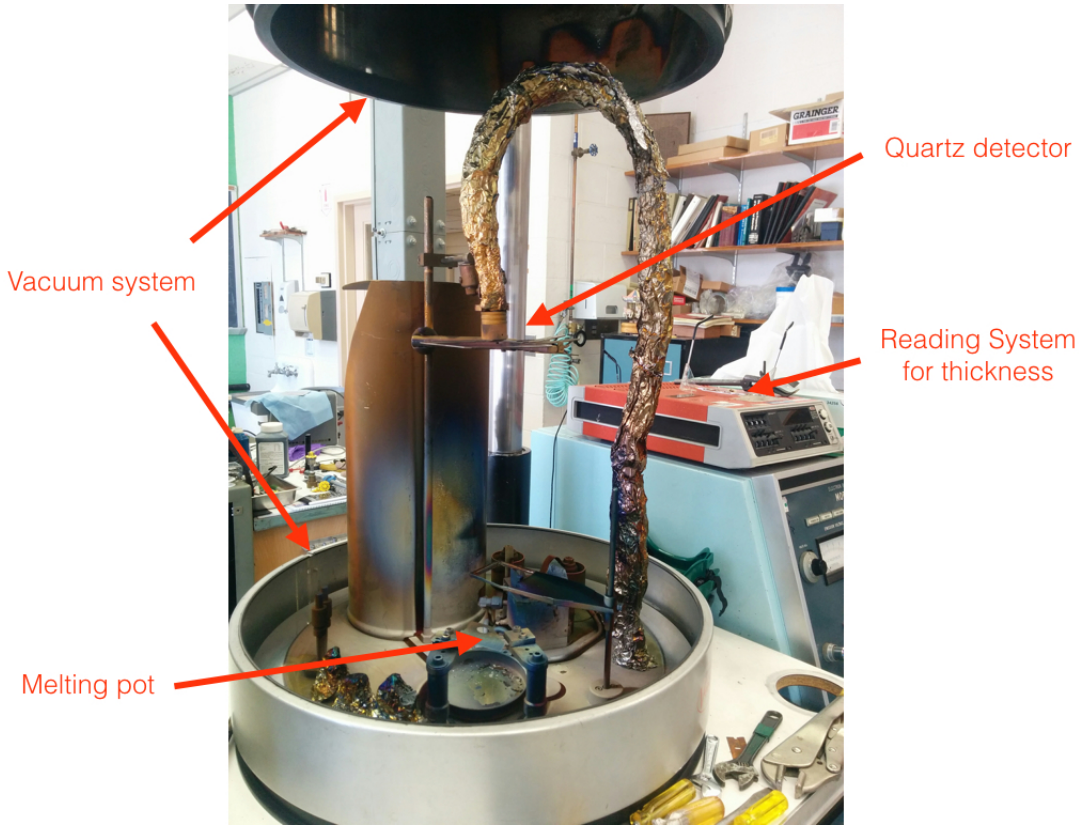

Figure 4.1: *Evaporator for target preparation*

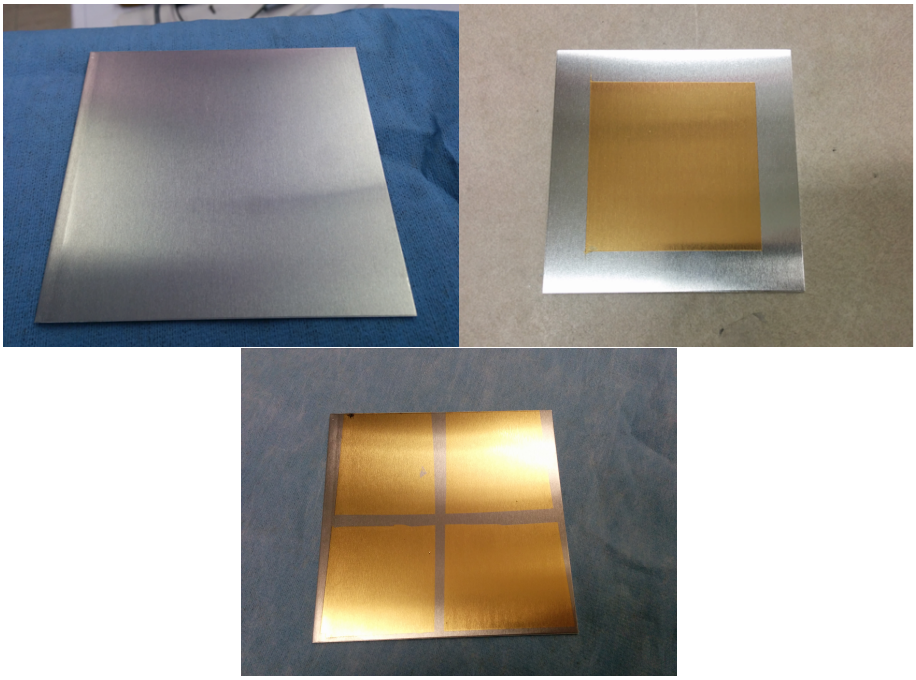

Figure 4.2: *Investigated targets, left side pure Al target, right side target with a film of gold, bottom side 4 different thicknesses on the same target*

In Fig4.2 we can see the target before the evaporation and after the film deposition. It is possible to have or the same film thickness on the target or different zones each with different thicknesses. The choise to use a bulk of 1 mm in thickness is due to that is enough to absorb all laser energy even if we use high energy and intensity. We choise to use gold film to cover the bulk for the large range of application of gold beam in accelerator field. In order to analyse more the target surface we performed Rutherford Backscattering Spectroscopy (RBS) to confirm the thicknesses of target. Generally the RBS technique is used to found elements in the bulk due to the impurity or due to implantation, in this case we can use the RBS to understand the thickness of gold film on the surface. Observing the two gold peaks in Fig4.3 we can see that the width of the signal produced by 125 nm of gold is about 50 channels while the width of signals of 250 nm is 100 channels, this confirm that the second target present a gold film double in thickness.

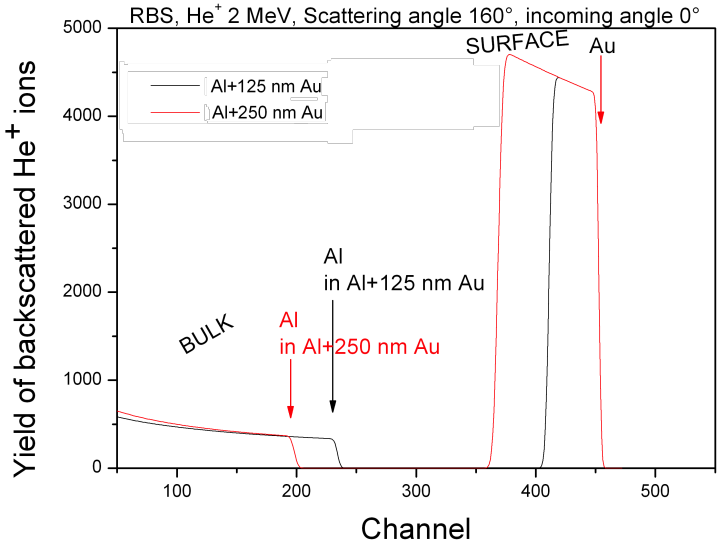

Figure 4.3: *Results of RBS analysis performed on 125 nm and 250 nm of Au on Al targets*

4.2 Brookhaven's Experimental setups

The experimental setup used in BNL is reported in Fig.4.4. The shown setup is very simple, the laser beam is focalized on target inside the vacuum chamber and the produced plasma travels along the normal direction up to the FC diagnostic and IEA [26]. The laser ablation plasma generated by a laser shot was expanded adiabatically normal to the surface. The Faraday cup was placed at 2.4 m far from target to measure plasma total current which had an aperture of 10 mm diameter and a mesh of which transmission was 85 % with a bias voltage of -2.5 kV to suppress secondary electron and extract ions from plasma. The charge state distribution was measured using a cylindrical 90 degrees ion energy analyzer (IEA) and a secondary electron multiplier (SEM) located at 1.4 m far to the FC. SEM was biased - 3.5 kV. Ion signal from each charge state was obtained by scanning IEA applied voltage until ion signal disappeared. The signal was enhanced and detected by the SEM of which multiplicity was different from ion energy, charge state and ion species.

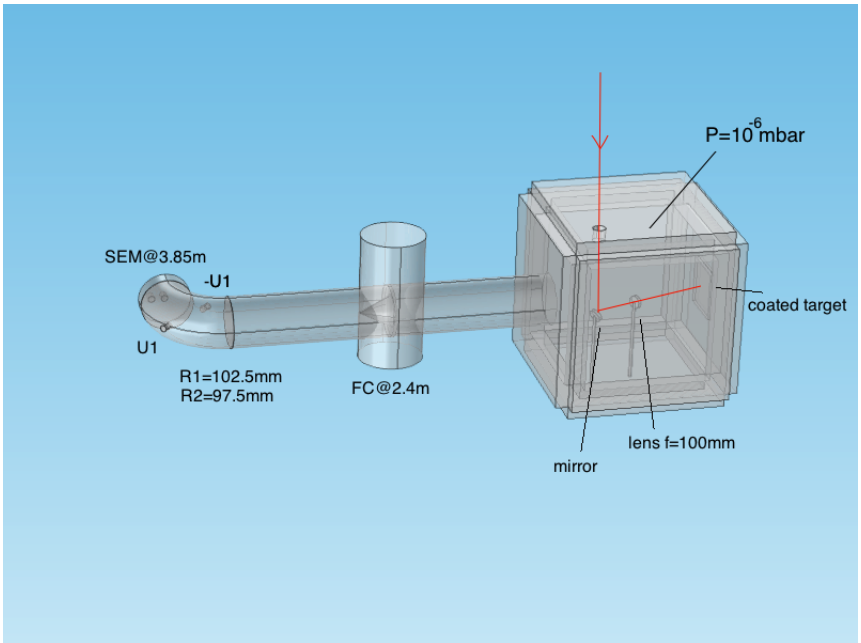

Figure 4.4: *Scheme of experimental setup in BNL laboratory*

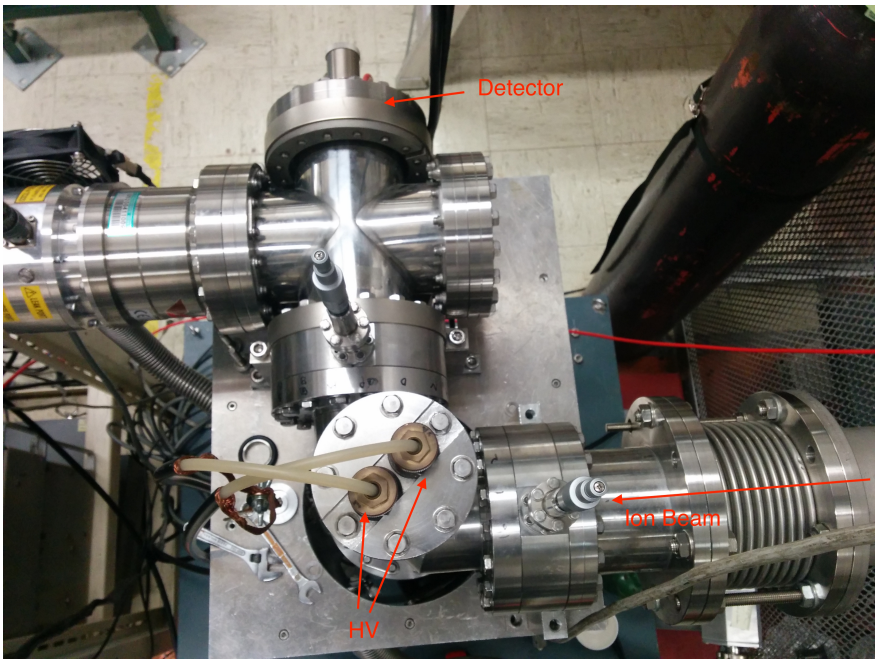

Figure 4.5: *Ion Energy Analyzer of BNL*

In Fig.4.5 is shown a picture of IEA of BNL, it is present an additional pump system in order to increase the vacuum level close to the detector.

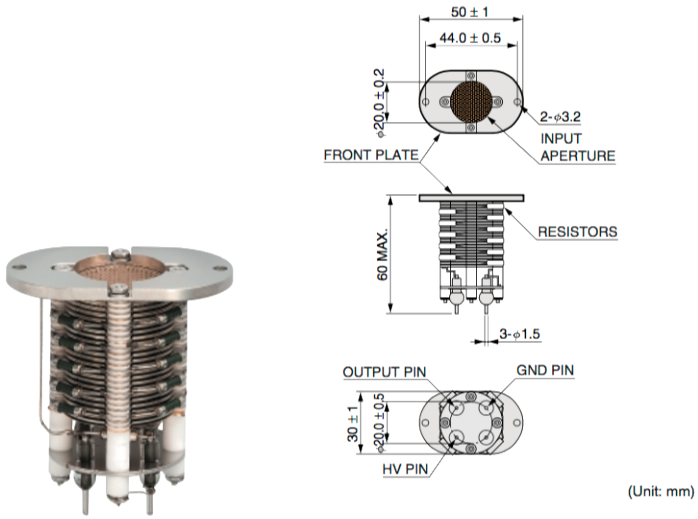

Figure 4.6: *Secondary Electron Multipliers used like detector*

Like detector we used an Hamamatsu R2362 Second Electron Multipliers. Electron multipliers are mainly used as positive/negative ion detectors. Hamamatsu electron multipliers have a high gain (multiplication factor) yet low dark current, allowing operation in photon counting mode to detect and measure extremely small incoming particles and their energy. In Fig.4.6 is shown the scheme of R2362, it is possible to observe a wide detection zone with diameter of 20 mm and the mounting plate that goes into high negative voltage. In Fig.4.7 is reported the electron emission ratio of SEM as a function of Ion acceleration voltage (egual to energy of particles). This calibration is very useful to understand how read and convert the experimental yields, for example if we consider an energy of 1 keV and we obtained an experimental peak of 100 mV, the Electron Emission Ratio is 3 and in this case the real peak yield is 300 mV. If we consider instead an energy of 100 eV for the same peak of 100 mV the real yeld is 60 mV.

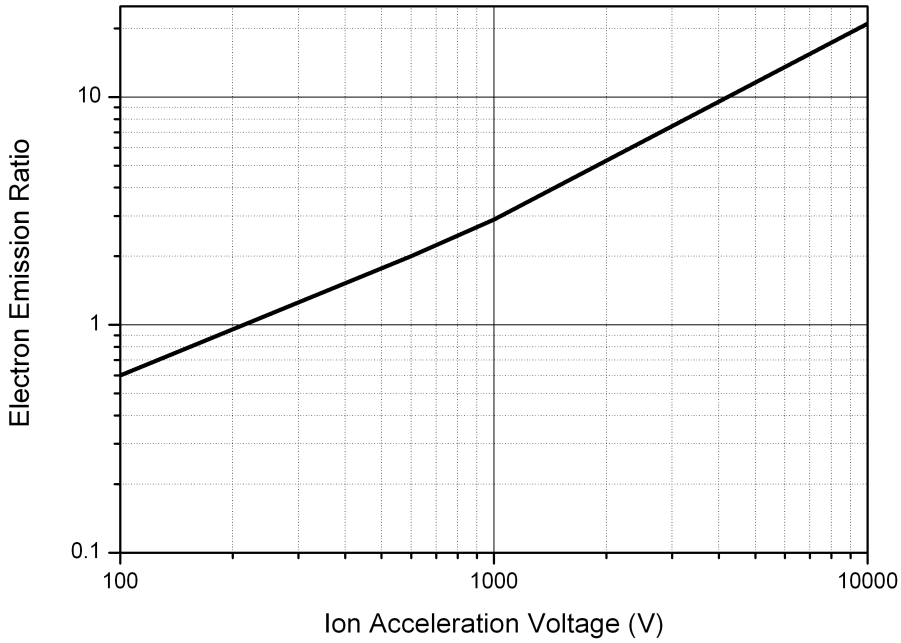

Figure 4.7: *Gain of SEM as a function of particle energy*

The employed laser was a Thales Laser System of 6 ns of pulse duration and energy up to 2.3 J. For our experiments we used a laser energy measured on the target surface of 1.094 J. A picture of laser system is in Fig.4.8. The laser is focalized on target using a lens with focal lenght of 100 mm. The laser spot is about 100 μm in diameter, this permits to obtain a laser intensity of $2.3 \cdot 10^{12} W/cm^2$. Like target-holder we used a stage linked with a motion controller "Newport model ESP301" with sensibility of $0.1 \mu m$. If z os the normal direction to the target, the stage has the possibility to move in x and y direction with sensibility of $0.1 \mu m$ for each direction. The employed oscilloscope was a Tektronix DPO4054 500 MHz and 2.5 Gs/s.

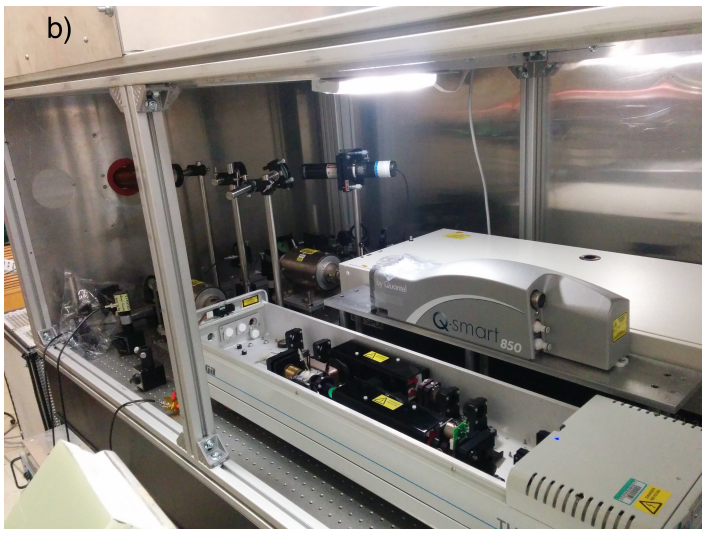

Figure 4.8: *Laser energy of Thales System as a function of shutter delay (upper side), picture of Thales Laser (bottom)*

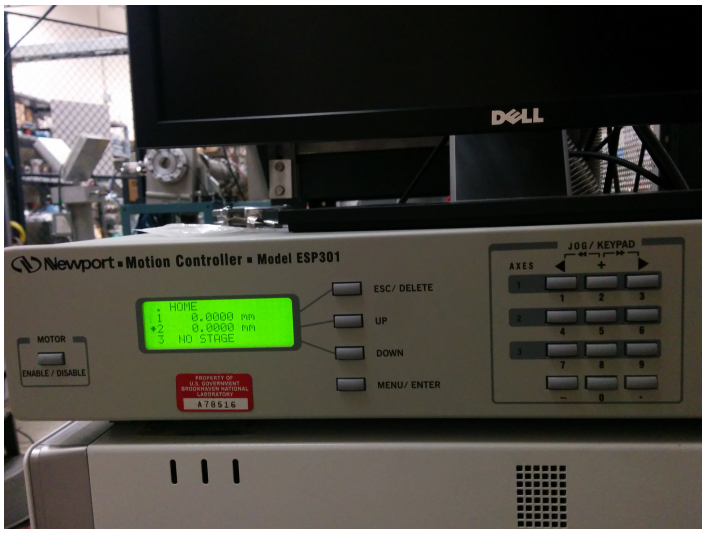

Figure 4.9: *Motion Controller for x-y stage target holder*

The Fig.4.10a shows the internal part of interaction chamber, last mirror and the lens are covered by a metallic mask that permitt to reduce the deposition of plasma on the optical surface. In Fig.4.10b is showed the holder, thank the use of the screws the target

are fixed on the holder and it does not allow the target to move during and after the laser interaction.

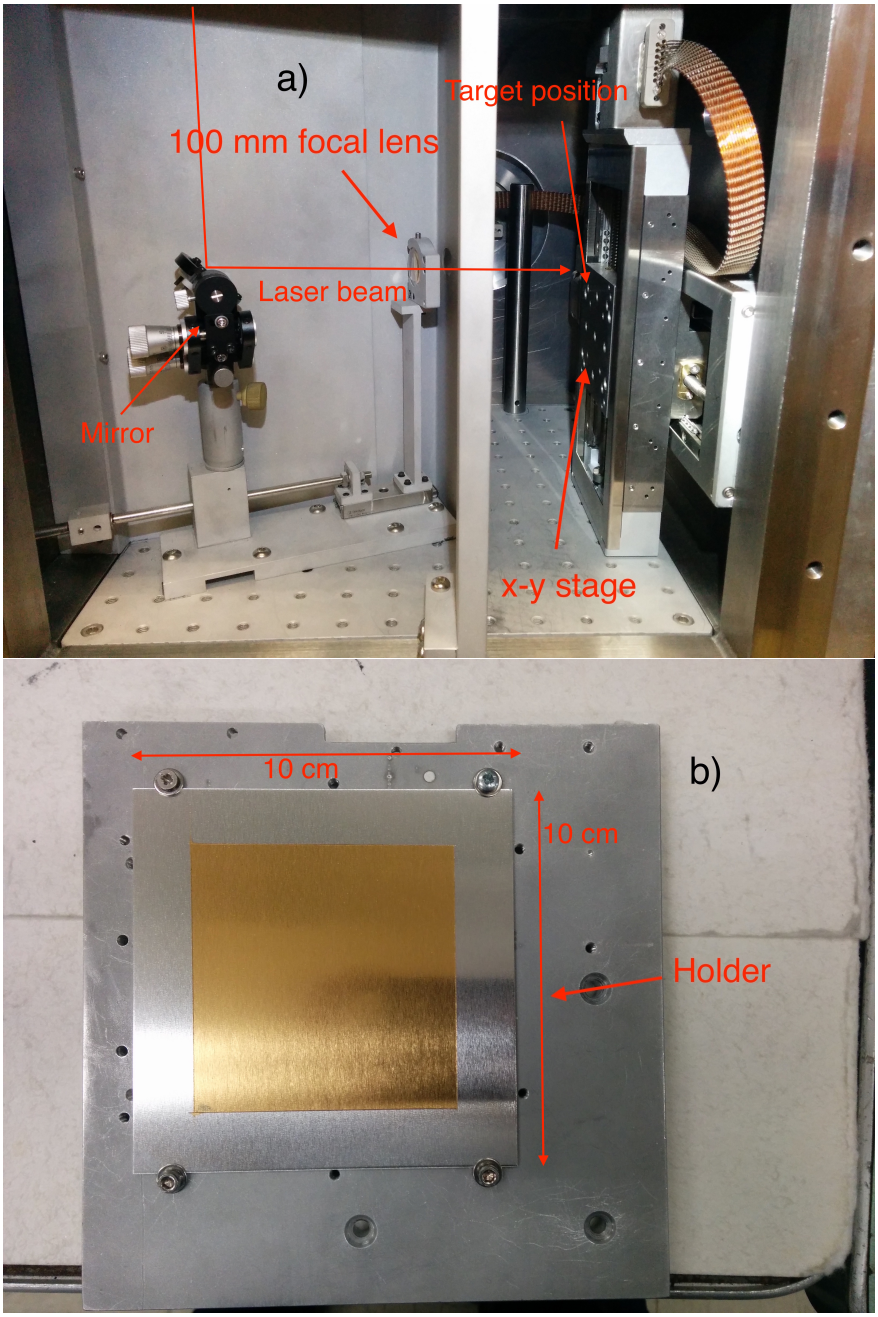

Figure 4.10: *Internal part of vacuum chamber (upper side), Target assembled on target holde (bottom)*

4.3 BNL's results

In the BNL investigated targets had thicknesses of 250 nm, 400 nm, 500 nm, 750 nm in addition to the Al pure target. The first investigation consist of Time of Flight measurements with Faraday Cup. Like said above the FC was placed at 2.4 m from the target along the normal direction. The results in Fig.4.11 shows that with the increase of the gold quantitive, the TOF increase from 5.76 μs for Al pure up to 14.8 μs for 750 nm of gold. Similar discussion for the plasma yield that instead decrease from 121 mV up to 5 mV, these results show that there is a some kind of trand. In figure we can see the overlap of ToF spectra obtained in the same experimental conditions and an insert that shows a zoom of the zone where there are the spectra of 500 nm and 750 nm of gold, without zoom it is to difficult to see the signals for the very low yield of about 5 mV, even if the signals are very small they are clear.

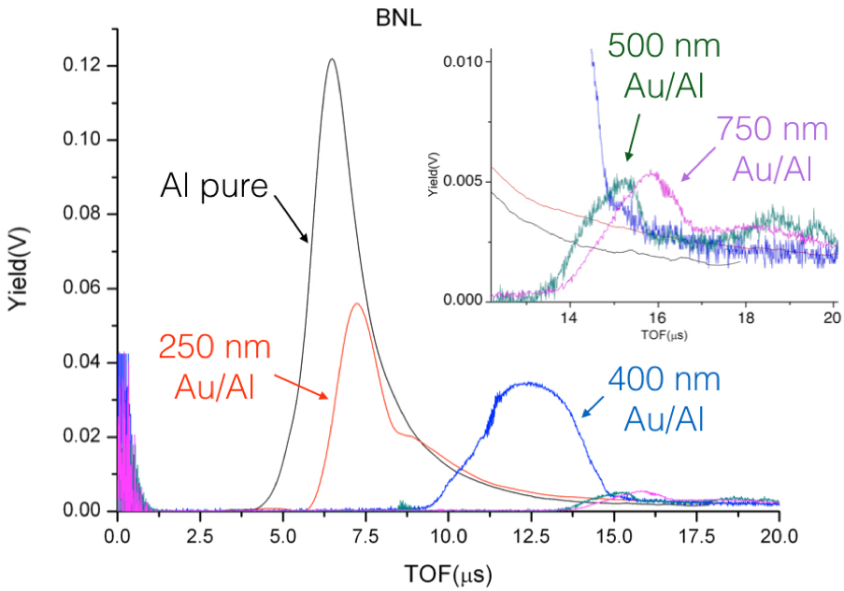

Figure 4.11: *Time of Flight results obtained irradiating Al pure and Au coated Al targets, in the insert the zoom for 500 and 750 nm of gold.*

Table 4.1: Resume of values for ToF (at half height) and the yield (maximum value) for BNL

Target	**TOF(μs)**	**Yield(mV)**
Al pure	5.76	121
250 nm	6.55	55
400 nm	10.83	37
500 nm	14.13	5
750 nm	14.8	5

After the ToF measurements we used a Ion Energy Analyser for the study of charge states inside of plasma with their distribution. We can observe in Fig.4.12 the charge distributions for the Al target.

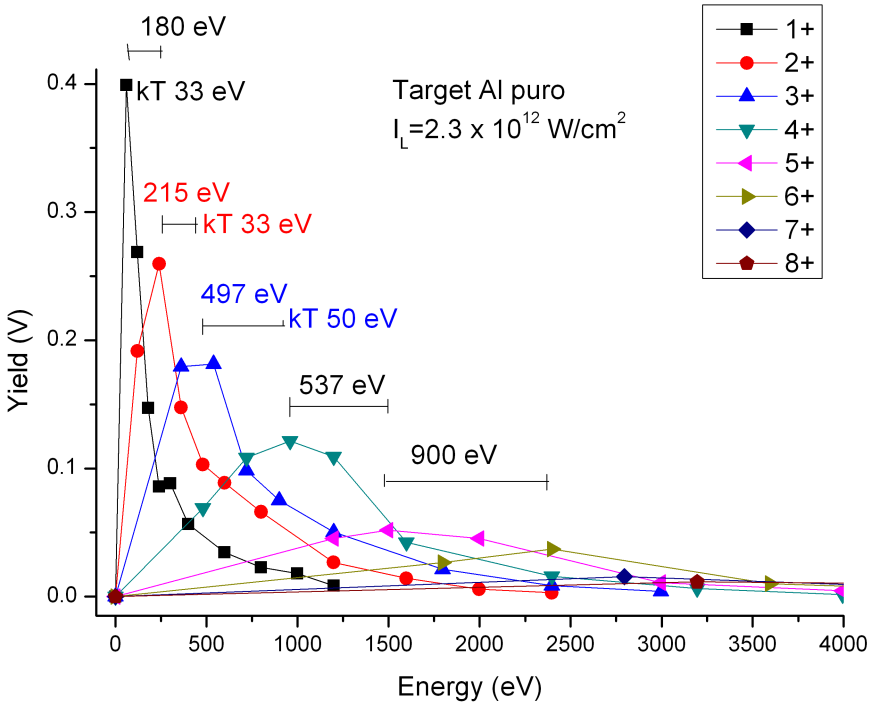

Figure 4.12: *Ion Energy Distribution for 8 charge state of Al obtained scanning the voltage of IEA plates irradiating Al pure target*

Thanks to all measures we obtained information about the max charge state produced from laser target ineraction, the max charge states are reported in the follow table:

Table 4.2: Resume of charge state produced by interaction laser with coated targets

Target	**Max Charge state (Al)**	**Max Charge state (Au)**
Al pure	8	-
250 nm	8	-
400 nm	8	8
500 nm	8	10
750 nm	-	14

In Fig.4.12 are shown the distribution with the energetic gap beetwen each charge state and relative temperature calculated thanks to CBS function [20]. How it is reported, the energetic gap increase with the charge state from a value of 180 eV reaching values above 1 keV for Al pure target. Instead the temperature are the almost the same for all charge state.

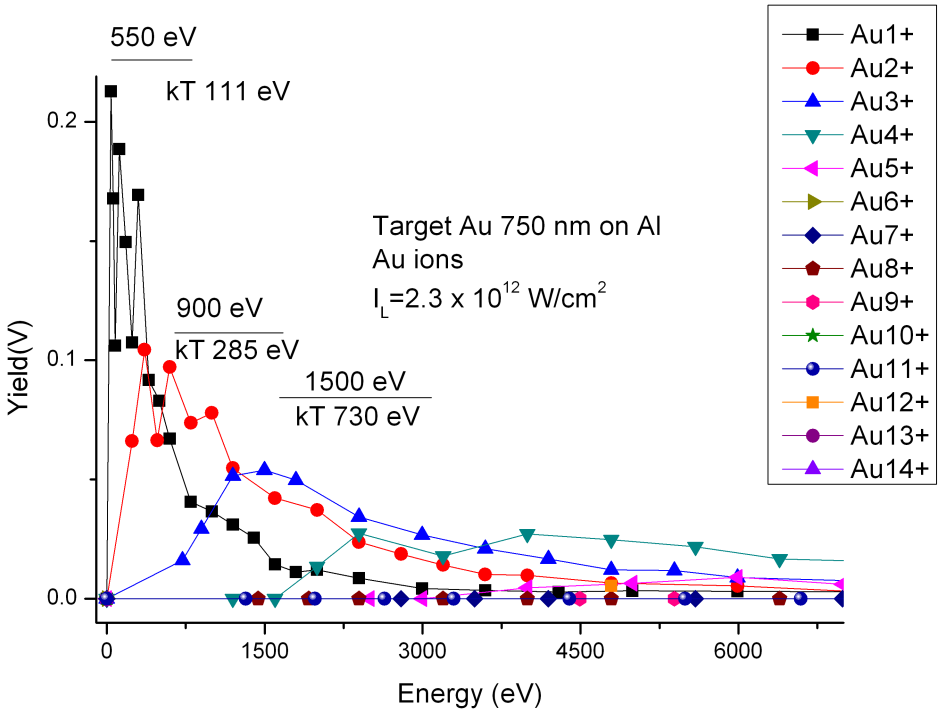

Figure 4.13: *Ion Energy Distribution for 8 charge state of Al obtained scanning the voltage of IEA plates irradiating Al + 750 nm Au target*

If we analyse the results for 750 nm of gold in Fig.4.13 there is the same increase for the energetic gap, but also the temperature increase with the charge state. A very interesting result is that using 750 nm of gold we don't observe any trace of Al ions in the plasma, this means that is a thickness that permits to obtain a pure gold plasma without the use of a gold bulk. Also in this case the energetic separation and also the temperature increase with the charge state.

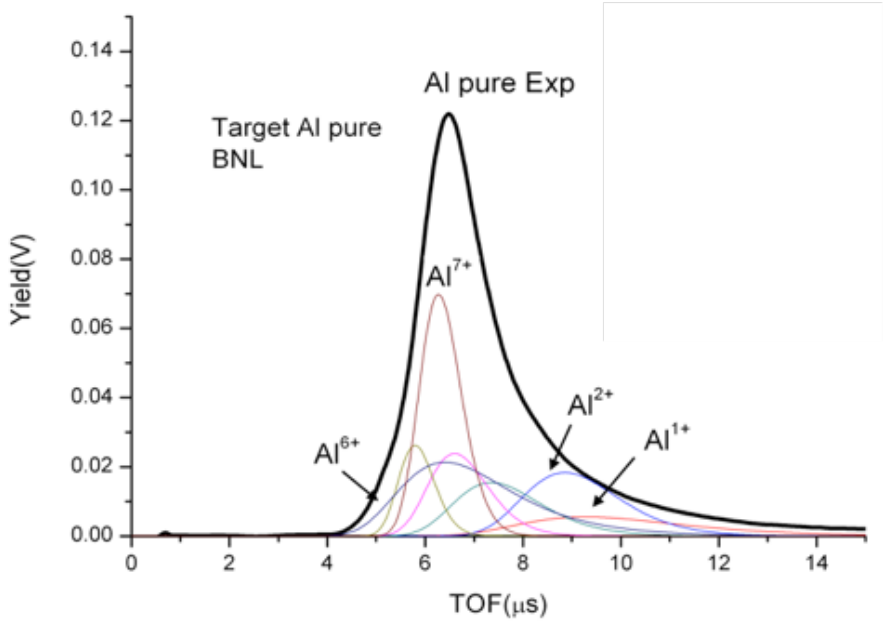

Figure 4.14: *Deconvolution of ToF spectra of Al bulk*

The use of the IEA permits to obtaine the useful informations for to make the deconvolution with the use of CBS function [20]. In the example reported in the Fig.4.14 I did the deconvolution of Al ToF spectra with 7 charge state of the Al in the case of Al pure target with 1+ and 2+ the slowest population, while 6+ and 7+ the faster with a yield peak very high for 7+. After this process it is possible to calculate the maximum energy of the chemical species that there are inside on plasma, like reported in Fig.4.15. This kind of behavior for Al ions can be explained considering that in front to the Al bulk there is an Au film. The Au ions are slowly compared with Al ions and for this we can imaginate the Au cloud like a sheel that keep slow the Al ions. Increasing the gold thickness this effect increase and for this reason the Al energy has this trend. For the Au energy instead we can immaginate the opposite situation, when there is not a contribute from Al ions, 500 and 750 nm, we observe a behavior like gold bulk, instead for 400 nm we have the Al cloud that push on the Au cloud increasing is velocity.

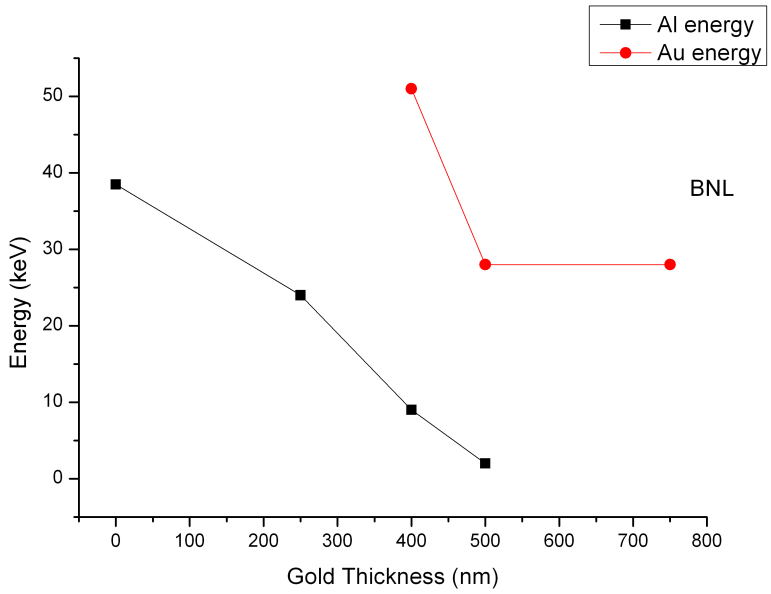

Figure 4.15: *Energy as a function of gold thickness*

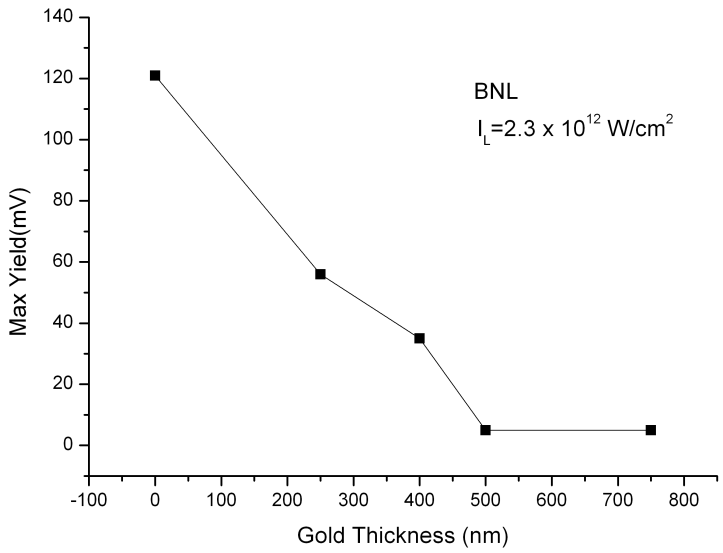

Figure 4.16: *Plasma Yield obtained from ToF spectra*

The graph reported in Fig.4.15 shown an important information obtained during the measures, only the targets with 400 nm and 500 nm of gold film are a mix of atomic species. The 750 nm gold film target has only gold ions behave like a bulk pure target, instead the 250 nm of gold produce Al ions but slowed down from the presence of Au, the Au ions didn't reach the detector. In addition the energy decrease with the gold thickness, like the maximum yield (Fig.4.16).

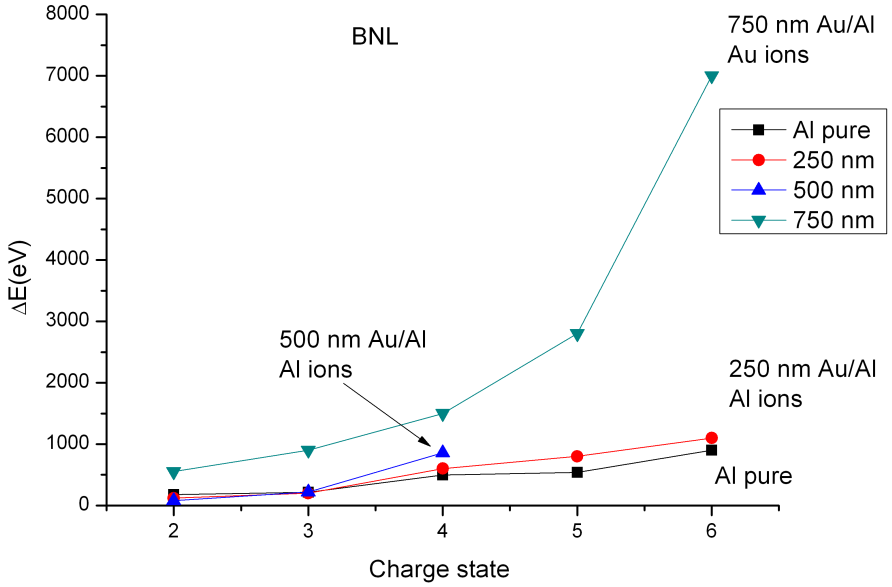

Figure 4.17: *Energy separation between the charge state*

Other informations can be obtained from the study of the IEA spectra like for example the ΔE per charge state and the plasma temperature. In Fig.4.17 is reported the trand of the ΔE for the investigated targets, we can observe like for Al pure and 250 nm of gols the values are almost constant, under the value of 1 keV. For other targets the energy increase with the charge state reaching values of 8 keV for 750 nm of gold. ΔE represent the energy of acceleration per charge state, then when there is a big quantitive of gold inside the plasma the ion acceleration energy increse.

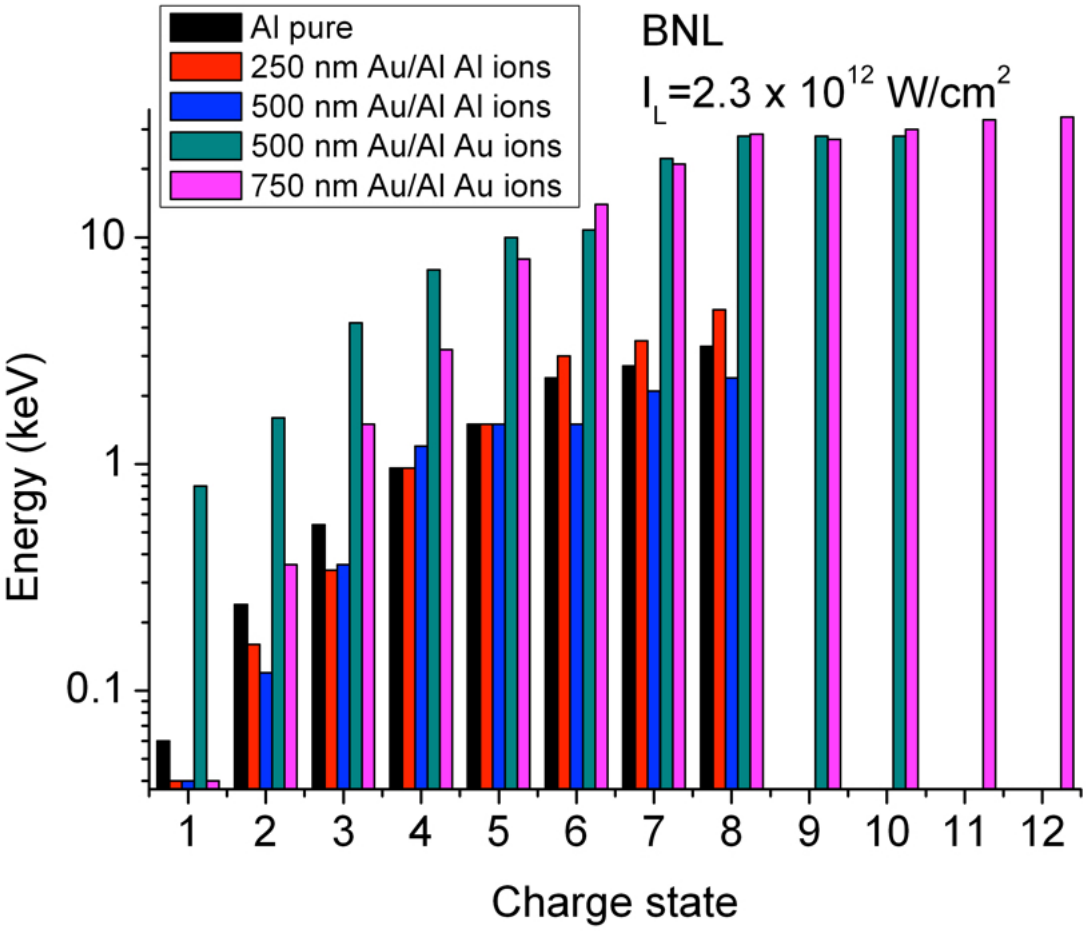

Figure 4.18: *Value of average energy per charge state*

In Fig.4.18 a resume graph shown the energy values per charge state, it is possible to see an increment of energy but a tendence to become constant at high charge state. Then big thicknesses of Au allow to obtain ions of high energy ($\sim 1 \div 2\ keV/z$) and so Au^{8+} of about $\sim 8 \div 16\ keV/z$

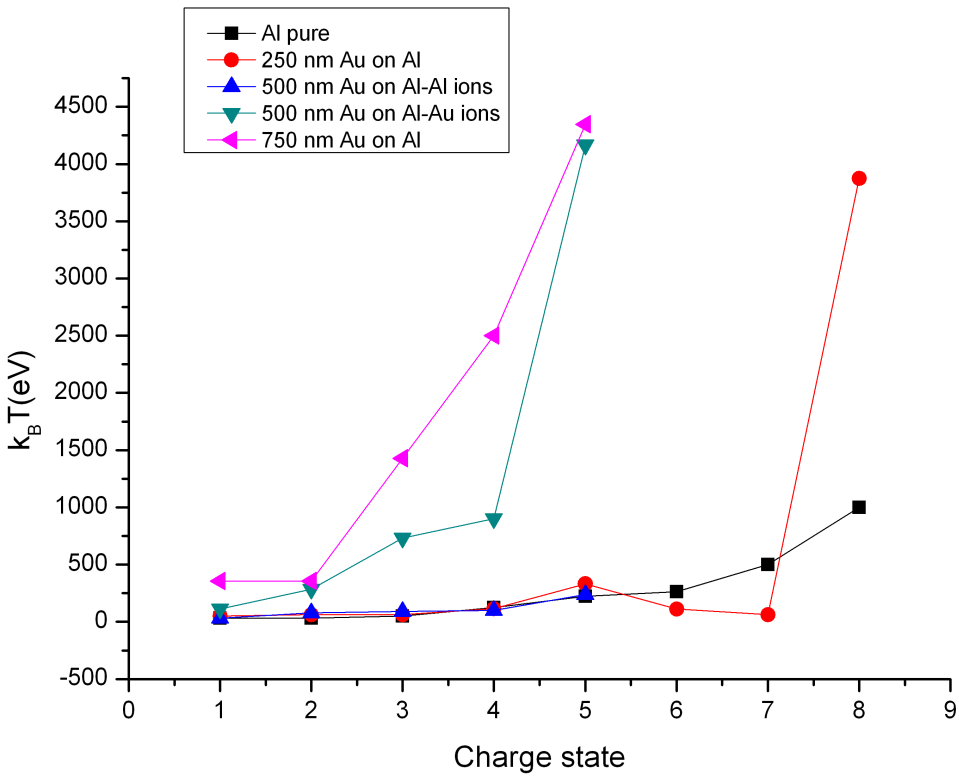

Figure 4.19: *Plasma Temperature obtained with CBS deconvolution*

It is possible to speak about particular considerations for plasma temperature. We can resume saying that there are two situations. The first is the one in which the plasma is very rich of Al ions and in this case the plasma has a temperature lower and indipendent from the charge state. The second one is when the plasma increase its quantitive of gold, in this situation the plasma temperature is higher and increase with the charge state very quickly. This dependence can be explained by an increase in the concentration of hot electrons generated in a plasma, which is proportional to $\sqrt{Z}$, and the plasma temperature is proportional to the electron density [52].

4.4 Messina's Experiment

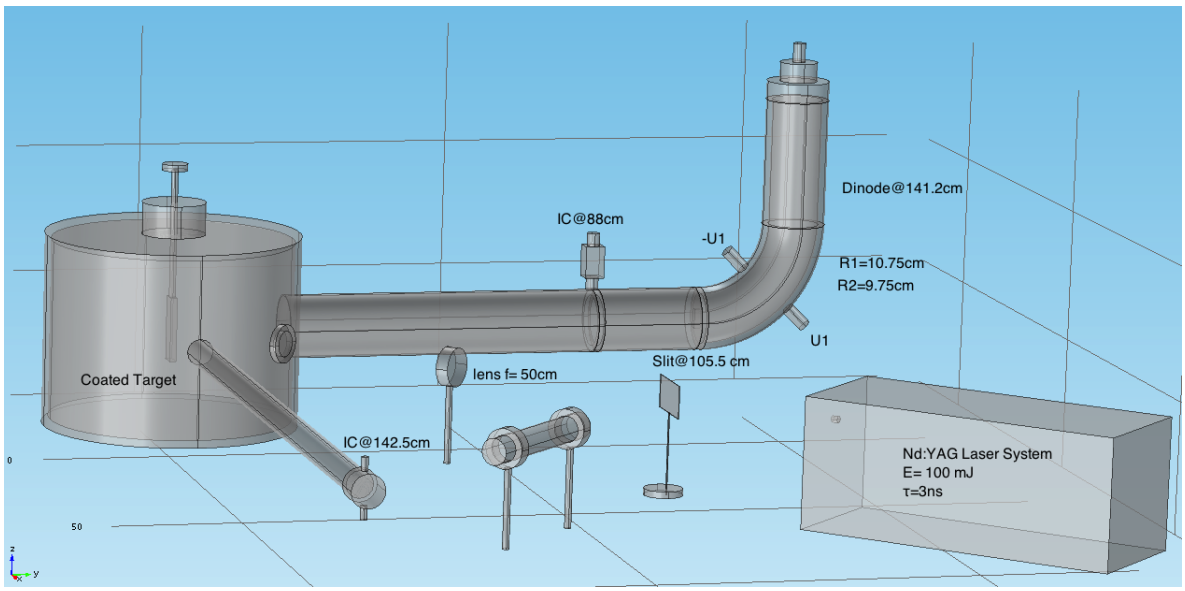

Figure 4.20: *Messina Setup for IEA measurements*

In Messina the experiments were performed in similar condition using the setup shown in Fig.4.20. The laser beam was focalized inside the vacuum chamber where interacting with the target produces the plasma that travel in vacuum condition up to reach the Ion Collector Ring placet at 88 cm of distance. ICR has a bias voltage of -100 V to suppress secondary electron emission. Also in this case the ion energy distributions were measured using a cylindrical 90 degree ion energy analyzer placed at the total distance from the target of 1.45 m. The detector is still a SEM with -3.0 kV of bias. Scanning the voltage applied to the plates we obtained the energy distributions that will be described below. The employed laser is a New Wave Tempest 300 with maximum pulse energy of 300 mJ and pulse duration of 3 ns. For our experiments we used an energy of 100 mJ focalized with a lens with focal length of 50 cm, obtaining a focal spot of 1 mm in diameter. With this setup we can obtain a laser intisity of $10^9 W/cm^2$. The employed oscilloscope used for monitoring the results was a Tektronix TDS 5104B 1GHz and 5Gs/s.

4.5 Messina's Results

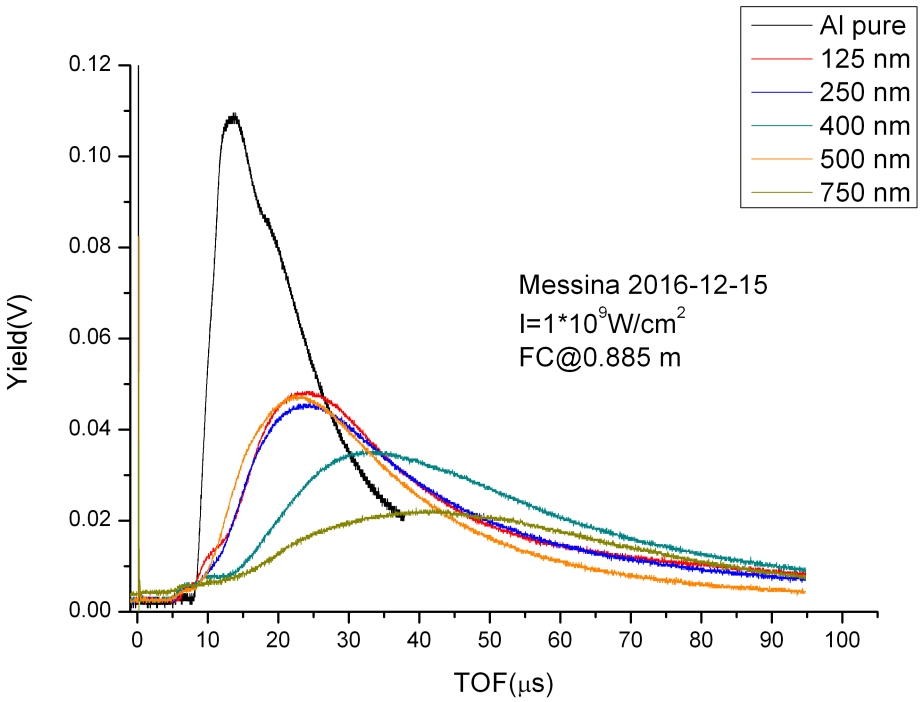

Figure 4.21: *ToF results for Au coated targets irradiated in Messina*

Also in this case the first information that we can obtaine is the time of flight spectra. In Fig.4.21 is shown an overlap of tof values for all our targets. In Messina we investigated all target with the thicknesses from 125 nm up to 750 nm.

Table 4.3: Resume of values for ToF (at half height) and the yield (maximum value) for ME

Target	**TOF(μs)**	**Yield(mV)**
Al pure	10.02	108
125	13.6	47
250 nm	15.0	46
400 nm	19.1	34.8
500 nm	15.2	45
750 nm	20.06	21.9

The ToF results show that with the increase of gold presence , the time of flight increase from 10 μs up to 20 μs, moreover it is possible to observe 3 different kind of behaviors, the first one is for plasma rich in Al ions with a very high yield and fast particles, the second for gold plasma with lower signals and lower velocity, and the third is the plasma with both ions mixed, in this case the behavior is intermediate between Au and Al plasma, all target with intermediate thicknesses present this kind of behavior.

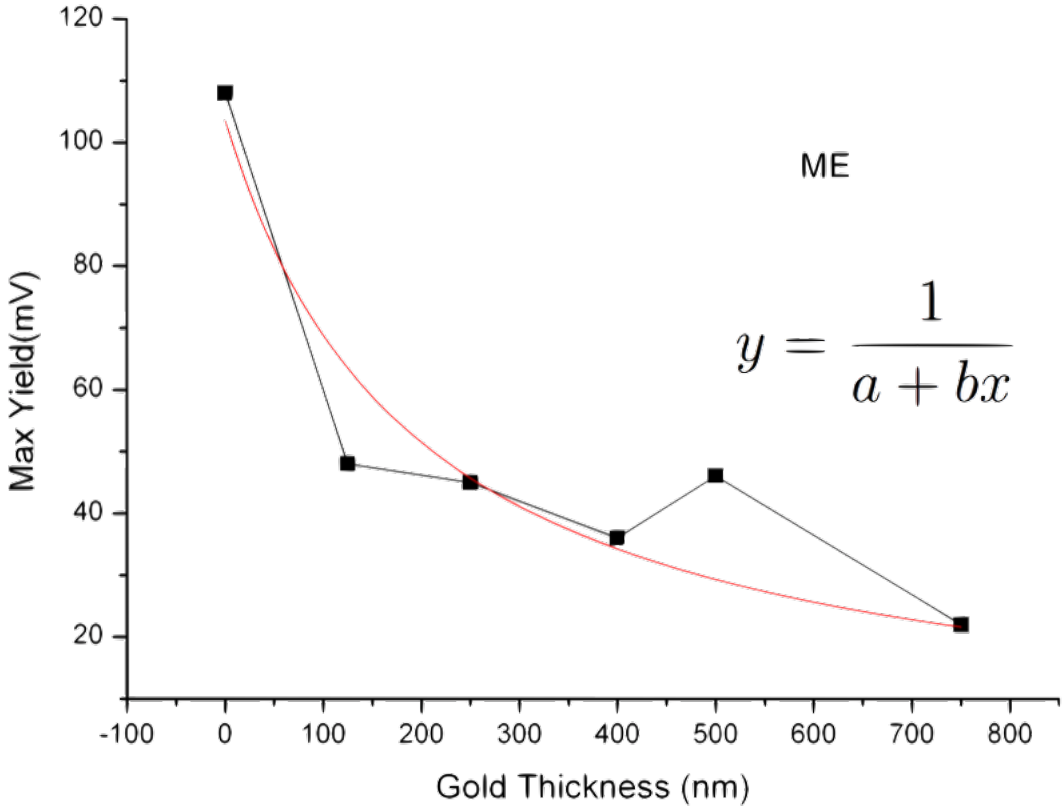

Figure 4.22: *Plasma yield emitted from targets irradiated in Messina as a function of gold thicknesses*

Like said above the yield follow a trend with the gold thickness, it reduce its value from 109 mV for Al pure up to 20 mV for 750 nm of gold. Other targets present values of around 40 mV similar for all. Probably the difference between these behaviors is in the depth of laser penetration into the target. For example, the target of 750 nm absorbs all energy and does not involve bulk in the interaction, but for the other targets the thickness of gold is insufficient and the plasma is greatly influenced by the presence of Al ions from the bulk produced by the ablation .

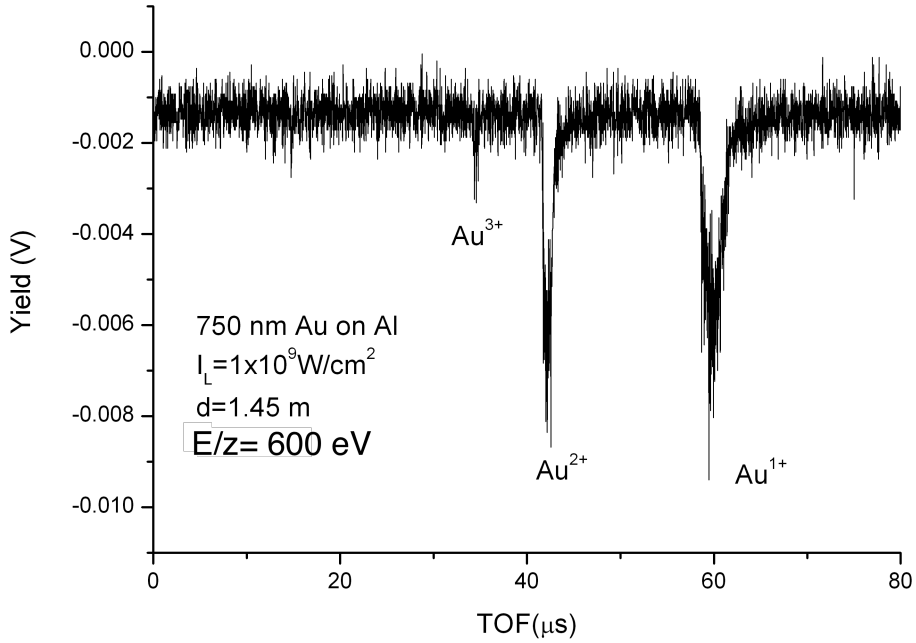

Figure 4.23: *Typical IEA spectra obtained in Messina*

Using $10^{12} W/cm^2$ laser intensity we obtained 8 charge state for Al and 14 for Au. Now using less intensity of course we will see less number of charge state. In fact irradiating the bigger thickness of gold we obtained only 3 charge state of gold, and the same number of charge state also for Al pure target like showed in Fig.4.23 and Fig.4.24. Other targets shown a good mix of the two ions species. Both graphs shown an $E/z = 600eV$, in these cases are present 3 charge state for Al ions in Al bulk and 3 charge state for Au in 750 nm of Au on Al. In both there is a very low signal of charge state 3+ compared with 2+ and 1+, this means that the energy is very close to the threshold for the production of 3+. For example in Fig.4.25 are shown the ion energy distributions obtained irradiating the target with 250 nm of gold, in this case in the first part of the spectra it is possible to see the smaller peaks due to the Al contribution with energy separation of 600 eV and approximately the same yield of few mV, while the Au peaks are bigger with an

energy separation of 1600 eV. If we increase the gold thickness we can reach the situation in which there are only gold ions thank to the thicnkess of 750 nm. This is shown in Fig.4.26, where we can see the energy distributions of three charge states of gold. After the IEA results, making a fit operation on the peak using CBS function, we obtained the plasma temperature for each target and per charge state. In this case the situation is different compared with the higher laser intensity because the plasma temperature remain constant with the charge state and increase only with the gold thickness thank to the increase of electron density.

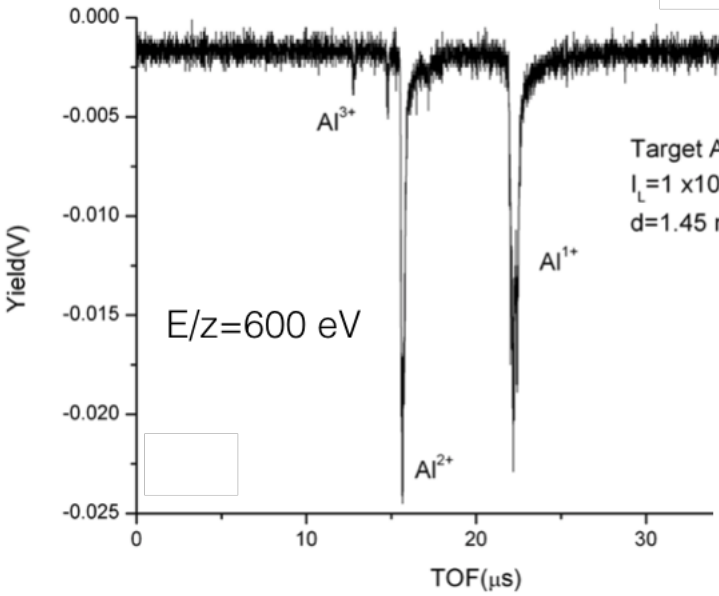

Figure 4.24: *Typical IEA spectra obtained in Messina irradiating Al pure bulk*

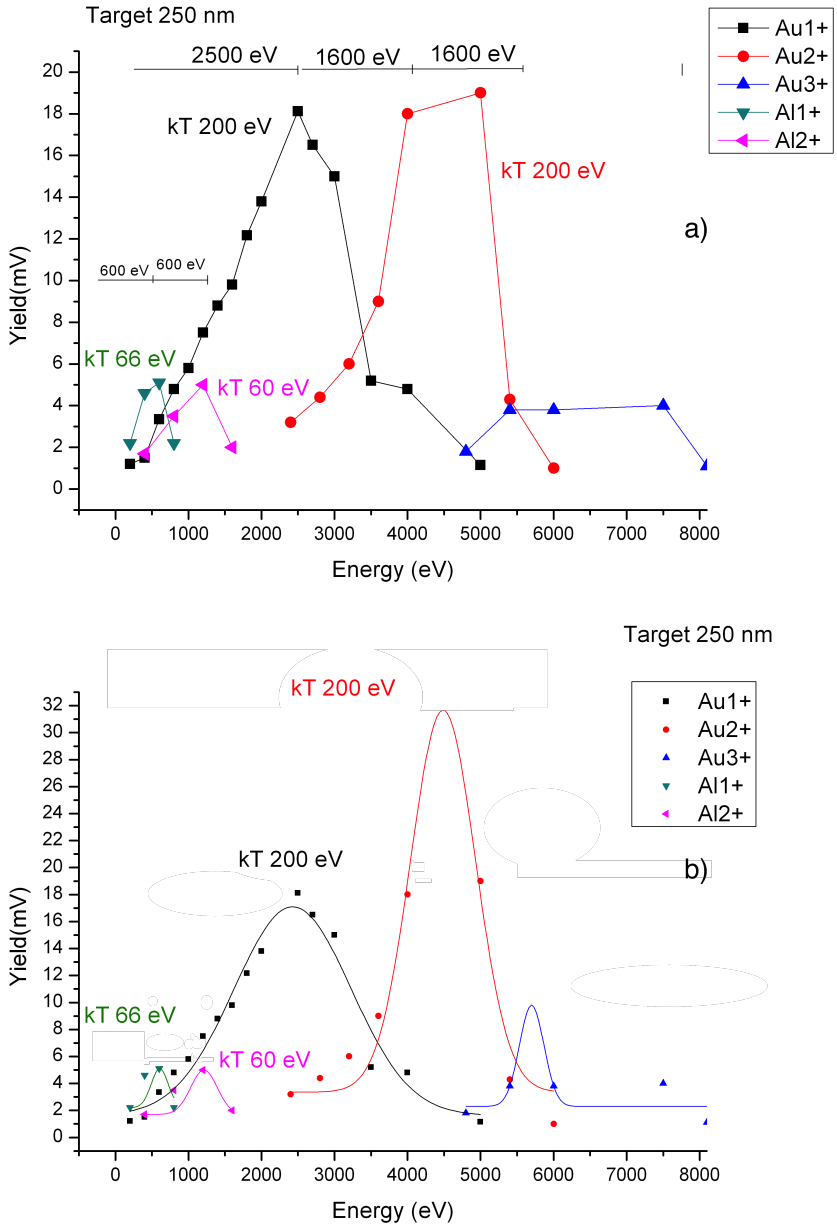

Figure 4.25: *a)Experimental Ion energy distribution for 250 nm of gold on Al bulk b) simulated CBS distribution for the charge state present in a) using the parameter obtained in the experiments.*

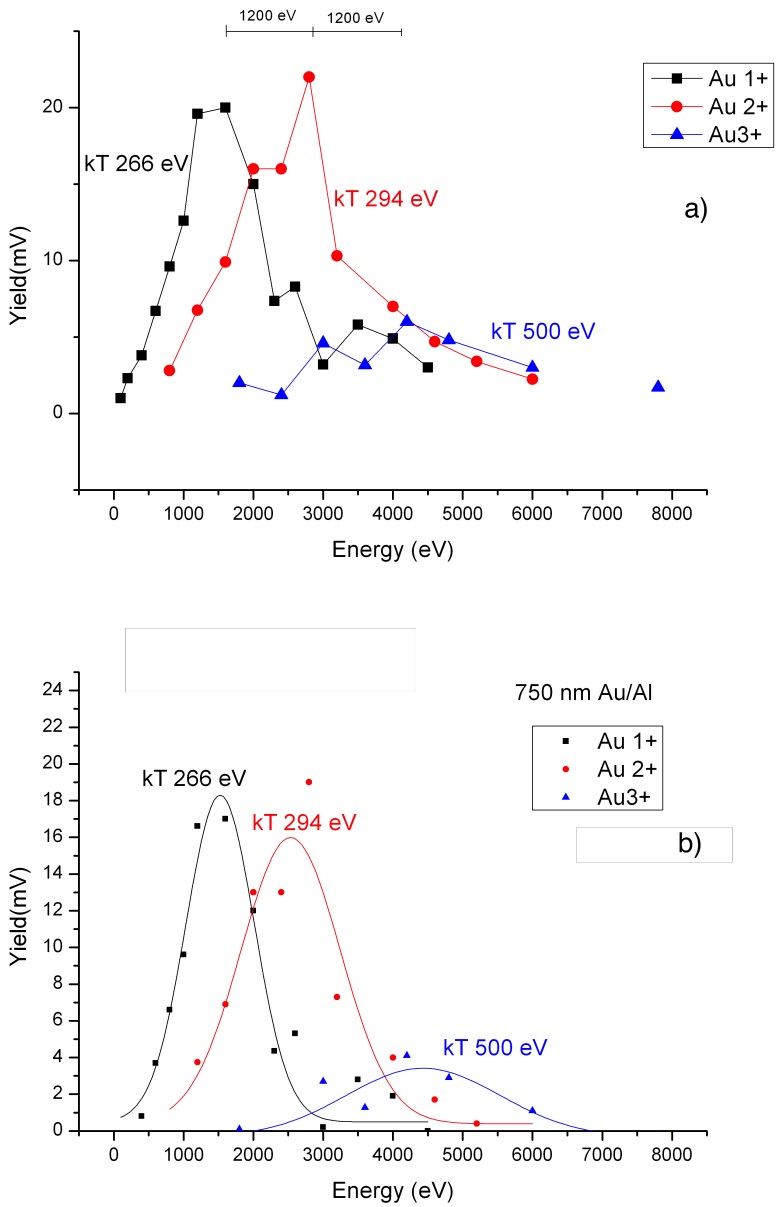

Figure 4.26: *a) Experimental Ion energy distribution for 750 nm of gold on Al bulk b) simulated CBS distribution for the charge state present in a) using the parameter obtained in the experiments.*

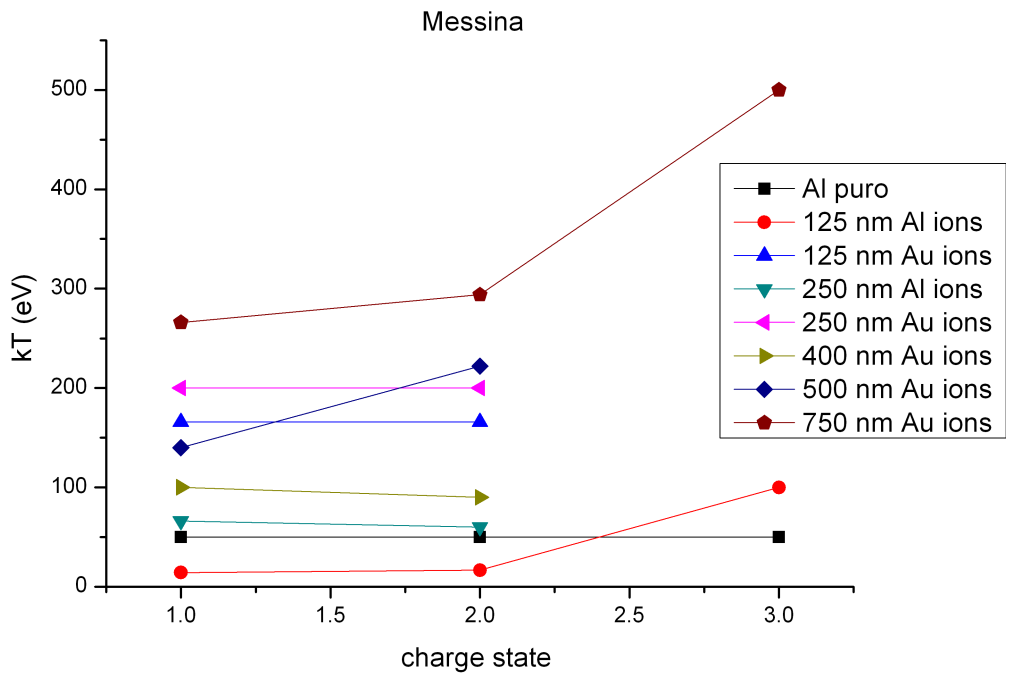

Figure 4.27: *Plasma Temperature per charge state and different targets*

Using the $10^{12} W/cm^2$ the temperature of plasma depended strongly from the quantitive of gold, in particular in the dependence from the charge state. In this case of $10^{10} W/cm^2$ instead we have that the temperature don't depend from the charge state and increase only thanks to the gold presence, because the temperature (like others parameters) depend strongly from the electron density of plasma, a gold plasma is very rich of electrons due to the high atomic number.

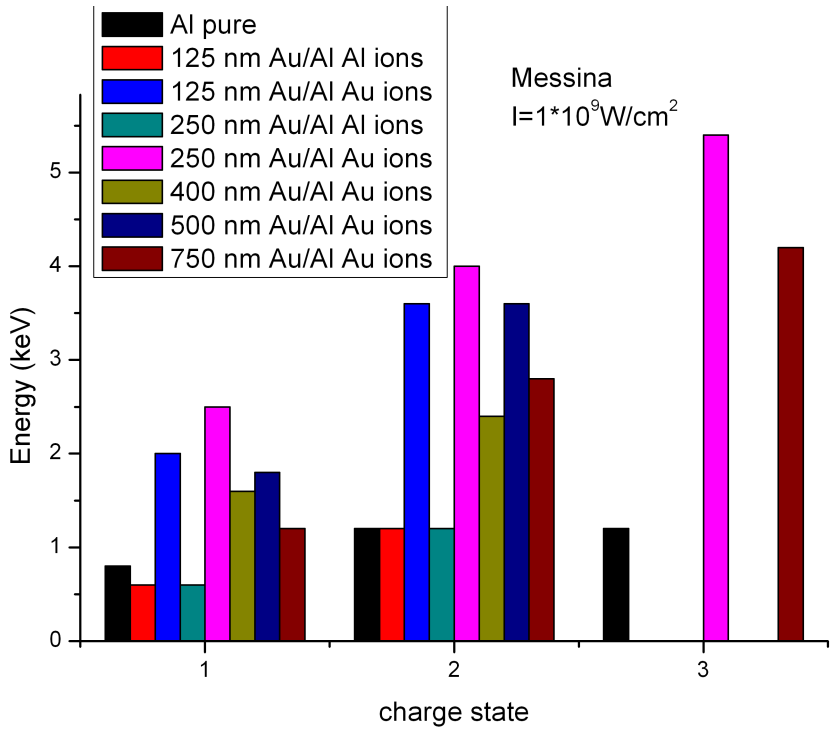

Figure 4.28: *Average Energy per charge state and for all targets*

In this graph are resume the values of energies obtained in this experiments with the lower intensities. It is possible to observe that there is a strong dependence from the energy and the charge state. In the following graphs we can observe the max charge state per each target for the two experiments performed in BNL and in Messina. Can be useful observe the results resumed in this way to understand quickly what happens in plasma formation. For example in Fig.4.29 it is simple to observe that in BNL the Al plasma has the same charge state for all targets except for 750 nm, this because with this thickness we didn't produce Al ions, while in Messina the ionization of aluminum plasma is reduced using even just 250 nm of gold, up to reach 0 with 400 nm, this because the deep of penetration of laser is less compared with BNL laser.

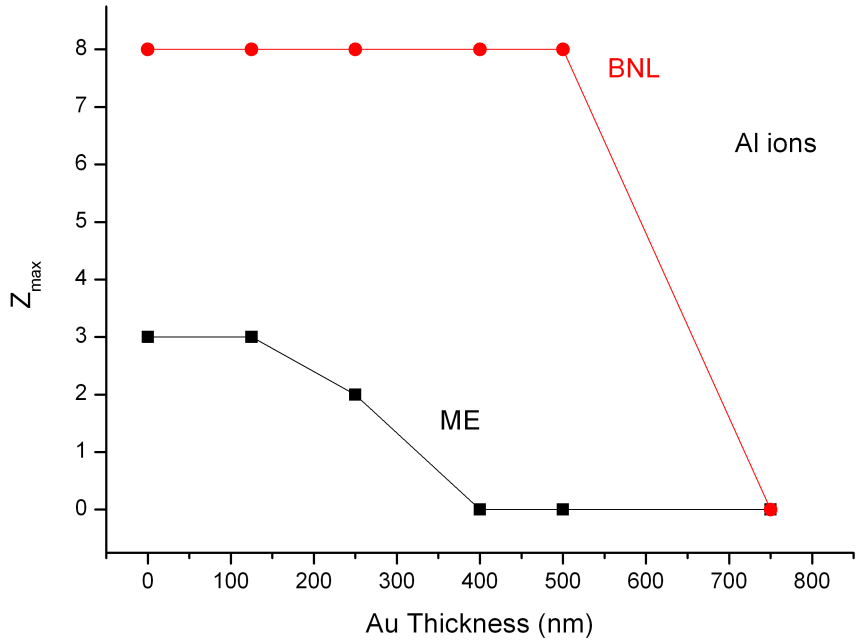

Figure 4.29: *Max charge state of Al ions for all targets*

If we consider the same resumed graph making for Au ions, Fig.4.30, we can see opposite situation. In Messina simply increasing the gold thickness the laser interacts most with the gold film depositing its energy in Au without reach Al bulk and for this reason increase the charge state. In BNL for the 125 and 250 nm we didn't observe charge state of Au may be because the Al cloud remove Au ions from the beam, but reaching the 400 nm of gold the production of Au in the plasma increase and the high temperature allows to reach 14 charge states.

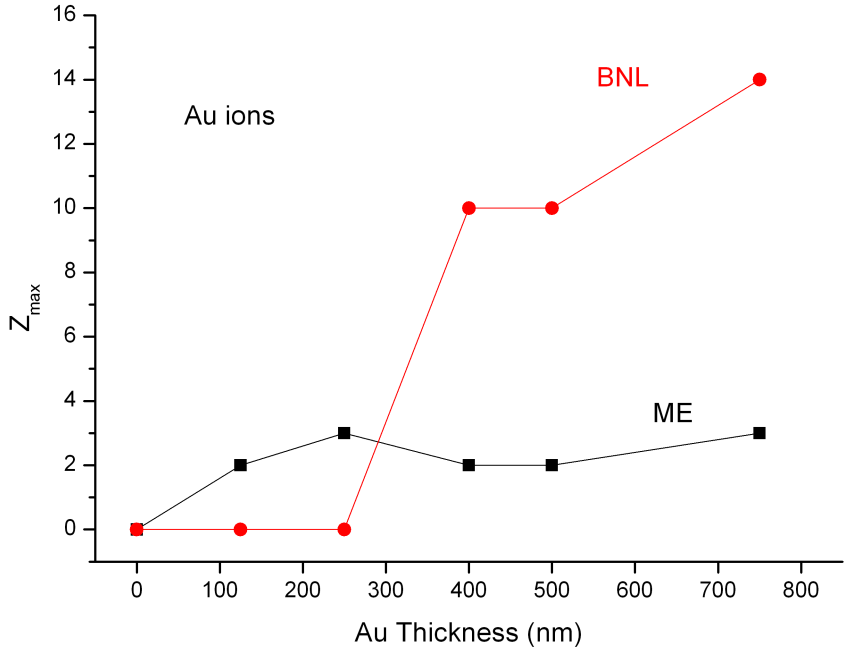

Figure 4.30: *Max charge state of Au ions for all targets*

Chapter 5

Applications of Plasma Source in Ion acceleration

The possible applications of laser-generated plasmas are extensive, from microelectronics [53] to thermonuclear fusion power [54], from magnetically confined plasmas to medicine [55]. One of these applications is the research field of particles acceleration. Accelerators are essential for science and society, they are in use in high energy physics, nuclear physics and life science. They are important to industry, the development of new materials, energy and can be applied in many other fields. For understand the importance of accelerators it is enough to think that the beam particles produced from they is usefull for medical treatments in hospitals and the role in very important experiments for understand the nature of our universe. There are many methods for produce a beam of particles with high energy and good quality using like source laser-matter interaction. For example these methods can be the use of Radio Frequency Quadrupole Linac coupled with a Laser Ion Source, or the injection inside a Superconducting Cyclotrone, Post Acceleration system using electrostatic field or using very high laser intensity in TNSA regime for the ion acceleration. All of these technique are characterized by different experimental configuration and in this chapter will be show the characteristics and principle of operation of these devices and techniques for obtain the best results in Ion Acceleration.

5.1 Radio Frequency Quadrupole

Radio-Frequency Quadrupole (RFQ) linacs are efficient, compact, low- energy ion structures, which have found numerous applications [56]. They use electrical RF focusing and can capture, bunch, and transmit high-current ion beams. Injectors are combinations of an ion source, a Low-Energy Beam Transport (LEBT) system, an electrostatic pre-accelerator or an RFQ, and an intermediate section that matches the beam to a following structure. The development of the RFQ structure with its ability to bunch and accelerate low-energy, high- current ion beams opens new parameter possibilities for accelerator designs. The variety of RFQ accelerators covers the full ion mass range from hydrogen to uranium, in the 5–500 MHz frequency range and duty factors up to 100%. The physics of the transport and acceleration of high-current ion beams in RFQs has been solved to such an extent that high-brilliance and high-current beams produced by ion sources and tranported in an LEBT can be captured, bunched, and transmitted with very small emittance growth by RFQs. Basically the RFQ is a homogeneous transport channel with additional acceleration. The mechanical modulation of the electrodes as indicated in Fig.5.1 adds an accelerating axial field component, resulting in a linac structure that accelerates and focuses with the same RF fields.

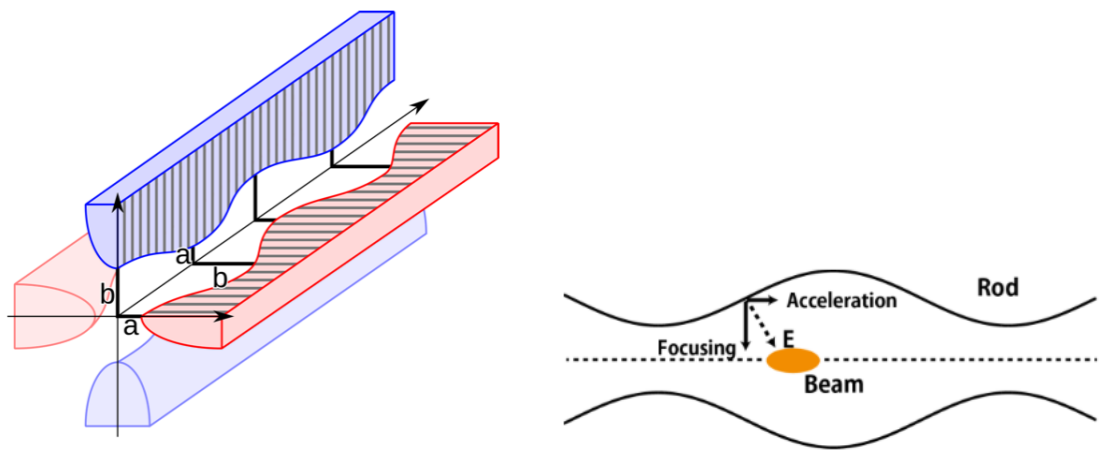

Figure 5.1: *Scheme of Radio Frequency Quadrupole*

The longitudinal field profile is almost independent of the transverse quadupole focusing field and is established by the modulations along the vane tip. The RFQ accelerator uses a transverse electrostatic field to focus the ions, and a longitudinal electrostatic field to accelerate the ions. The transverse alternating- gradient focusing results from the changing polarity of the RF field as the ion travels down the axis. The ripples on the vane tip generate a longitudinal accelerating field and have only a small effect on the transverse focusing field. When shaping the electrodes periodically in z-direction an additional longitudinal field component (in expense of the transverse ones) is obtained, thus forming a focusing and accelerating structure. The longitudinal field on the axis of the RFQ is of the form [56]:

$$E_z = E_0 \sin(kz - \omega t) \tag{5.1.1}$$

where $k = 2\pi/\beta\lambda$ (β is the normalized ion velocity and λ the free-space wavelength corresponding to frequency f $= \omega/2\pi$). The fundamental focusing period length β/λ is the distance an ion of normalized velocity $\beta = v/c$ travels in one rf period. If we indicate with E the total energy of particle, the incremental energy in rfq is:

$$\frac{dE}{dz} = qeE_z cos\phi_s \tag{5.1.2}$$

where q is the number of charges e on the ion, and the energy E, is that of a synchronous particle which travels along the traveling wave at a synchronous phase ϕ_s, below the peak value of the accelerating field E_z. As will be seen, a negative ϕ_s, produces a net longitudinal restoring force for particles around the synchronous particle.

5.1.1 Injection in RFQ

It is difficult to transport and inject an intense heavy ion beam to a radio frequency quadrupole linac because of a space charge effect. The beam transportation problem was completely overcome by a direct plasma injection scheme (DPIS) proposed in 2000. Laser ion source with DPIS is a promising candidate for a pre-injector of a high-brightness accelerator [57] [58]. In this scheme, ions are transported in neutralized plasma state to avoid

beam loss issue at low energy beam transport line (LEBT). It was verified experimentally that more than 10 mA of fully stripped carbon beam can be accelerated with this scheme [59] [60]. In DPIS, high current ion beam is extracted from laser plasma at the entrance of an RFQ linac. Then the beam is captured by the RFQ electric field, and is accelerated efficiently.[61].

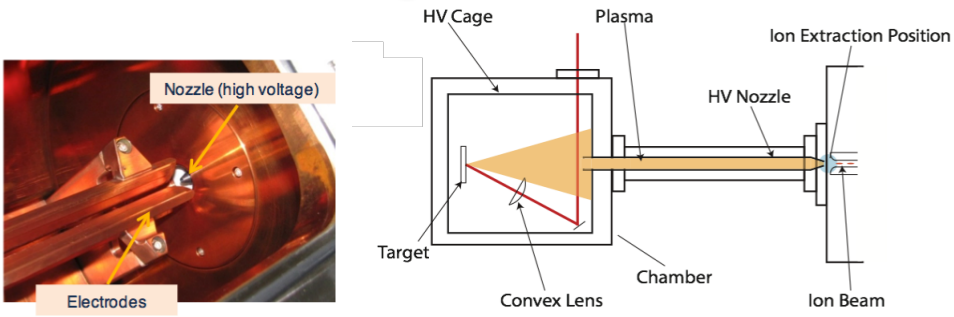

Figure 5.2: *Injection zone of RFQ with view on the electrodes*

The ions injected into RFQ have different kinetic energies depending on their own charge states, because they are extracted from same electric field. Therefore, ions whose charge state is enough lower than designed charge-to-mass ratio would not captured and just drift to the exit of RFQ tank, because the electric force is too small for an ion to be captured in an RF bucket, which might be absent entirely. However, ions whose charge states are higher or comparable with the designed charge to mass ratio would be captured by RF bucket and accelerated in RFQ [62]-[63].

5.1.2 Extractor system

The extractor takes the plasma flux $J \propto qnv$ and forms a beam with energy $E = q(V_{source} - V_{gnd})$ transporting it to the following step.

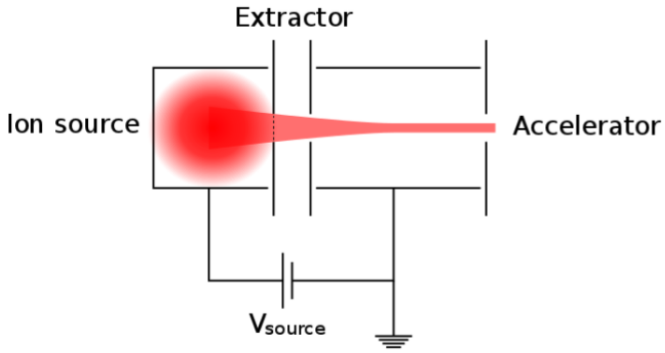

Figure 5.3: *Extractor schema*

The plasma expands through the drift region, free of external fields, before the ions are extracted. This is to allow the plasma density to fall to a value at which ions can be extracted with voltages of about 20 kV. In DPIS scheme, ion beam is extracted at the entrance of the RFQ electrode region and the extracted beam is immediately captured by a *rf* quadrupole electric field. In the DPIS with beam extraction in the RFQ cavity (DPIS-BERC), ion beam is extracted at the entrance of the acceleration electrode region and the extracted beam is immediately captured by RFQ electric field [64].

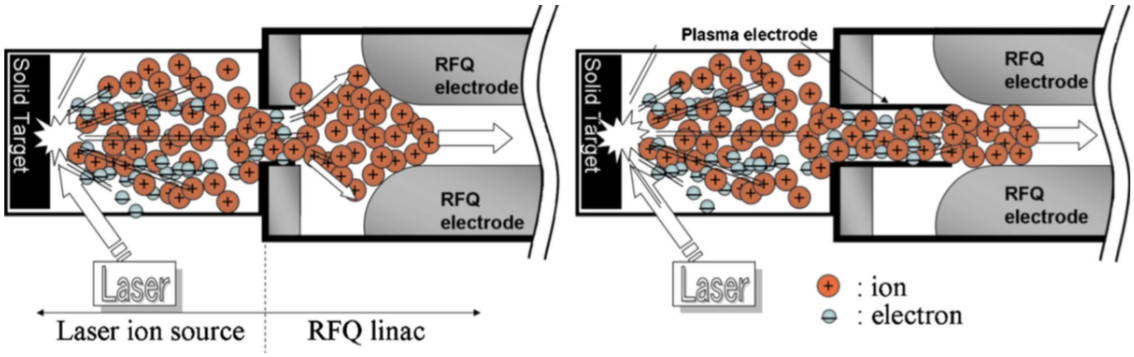

Figure 5.4: *The concept of the DPIS a) and DPIS with beam extraction in the RFQ cavity DPIS-BERC b) .*

The concept of the conventional DPIS a and the DPIS-BERC is shown in Fig.5.4. The basic configurations of both DPISs are similar, that is, the laser ion source is directly

connected to the RFQ linac without low energy beam transport line. An ion beam is extracted after a laser plasma generated in a laser ion source is transported to the edge of a plasma electrode, keeping plasma state. In the RFQ linac, ion beam is transversely focused by rf electric-quadrupole fields that are generated by four equally spaced conducting electrodes, placed symmetrically about the beam axis. In the conventional scheme Fig.5.4a the beam is extracted at the edge of the cavity at which the rf fields are weak. Since the beam travels to the entrance of RFQ electrodes without focusing effect, the beam is diverged due to space charge effect and extracted angle of each ion. Thereby, large beam loss takes place in the linac because of mismatch between the injected beam emittance and the RFQ acceptance. In the DPIS-BERC Fig.5.4b the plasma electrode is inserted in the RFQ linac cavity. The ion beam is extracted at the entrance of the RFQ electrode region. The beam experiences the focusing force immediately after extraction. Therefore, the problem in the conventional DPIS is avoided.

5.1.3 Experiments with RFQ in BNL

To evaluate the multi-charge effect, in Brookhaven National Laboratory, a Nd:YAG (1064nm) laser was set to provide 1.0J per shot on a carbon target for the trial. The laser beam was focused on the target by a plano-convex lens and the laser power density on the target was about 10^{10} W/cm^2. The high voltage applied to ion extraction form the plasma was 25kV which is fit to the injection energy of carbon 4+ beam. Fig.5.5 shows the signal of the accelerated beam. The RF input power is 23.4kW. The peak current is 6 mA, and the pulse length is $2\mu s$. As seen in the figure, the beam was clearly bunched and this indicated the ion beam was accelerated. The ions were captuerd by longitudinal buckets. Fig.5.6 is the result with 19.7kW RF input power and 25kV extraction voltage. The carbon 4+ ions are completely accelerated, and the other charge state ions were not accelerated.

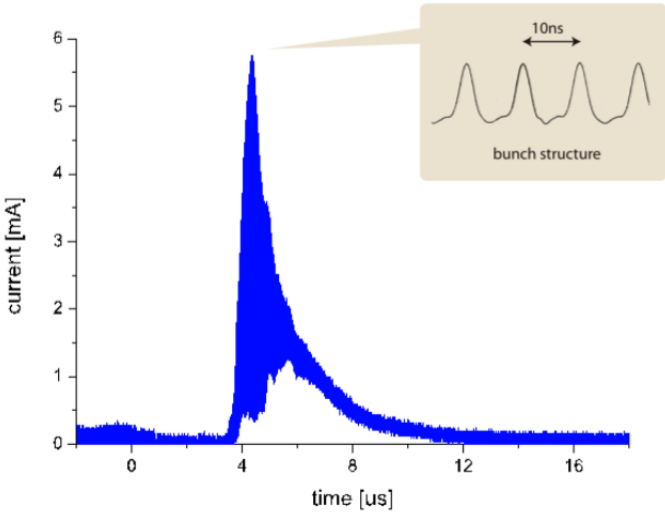

Figure 5.5: *Carbon beam signal and the bunch structure*

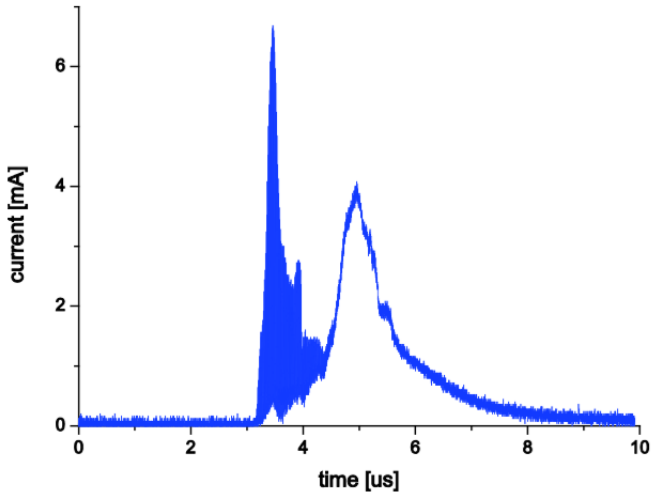

Figure 5.6: *Accelerated and Non-Accelerated Beam*

The RFQ parameters we used in this experiment are shown in Table [65]:

Table 5.1: Parameters of RFQ LINAC

Parameter	**Value**
RFQ Type	4 rods
Charge to Mass Ratio [q/A]	1/7.19
Length [m]	2.0
Input Energy [keV/u]	8.26
Output Energy [keV/u]	270
RF Frequency [MHz]	100
Acceptance [π mm mrad]	1.7
Input Emittance[π mm mrad]	0.35
Output Emittance (trans) [π mm mrad]	0.375
Output Emittance (longit) [π mm mrad]	33.6

The acceptance of the RFQ in the BNL design is comfortable, at 1.7 π mm mrad (norm.), with an aperture radius of 5 mm.

In some heavy-ion accelerator systems, for example, Electron Beam Ion Source (EBIS) Project at Brookhaven National Laboratory (BNL) and Direct Plasma Injection Scheme (DPIS), ions, which have close charge to mass ratio, are simultaneously injected into an RFQ linac with desired species [66]-[67]. In the EBIS-based pre-injector for Relativistic Heavy Ion Collider (RHIC) at BNL, which consists of EBIS, RFQ and Inter-digital H mode Drift Tube Linac (IH-DTL), the designed ion is Au^{32+}. The LION source is a new laser ion source (LIS), which was installed and commissioned at BNL for low charge state heavy ion production as an external source of primary ions for RHIC-EBIS. This system is equipped with two identical Q-switched Nd:YAG laser oscillators (850 mJ/6 ns at FWHM, 1064 nm wavelength). A built-in laser combiner merges the two laser beam into one laser path to aim at the same position. The laser is focused on a solid state target plate.The laser spot size on the target is 5 mm in diameter. The different laser energy of 500 - 700 mJ is used depending on the species to achieve singly charged ions. A 3-m-long solenoid

magnet guides laser-produced plasma to an extraction chamber, Fig.5.7. The solenoid magnet is used to reduce the diverging angle of expanding plasma. Typical magnetic field to be used is a few Gauss. With this drift length, ion beam with pulse width of a few hundreds of microseconds is achieved. Ions are extracted at the extraction chamber, and transported to EBIS, Fig.5.8 [68]-[69].

Table 5.2: Beam parameters for different charge states of Au at the exit of RFQ

Ions	**Energy (MeV)**	**Current (mA)**	**Transmission (%)**
Au^{32+}	62.00	10	91
Au^{31+}	61.08	10	86
Au^{30+}	62.08	10	55
Au^{33+}	61.87	10	58

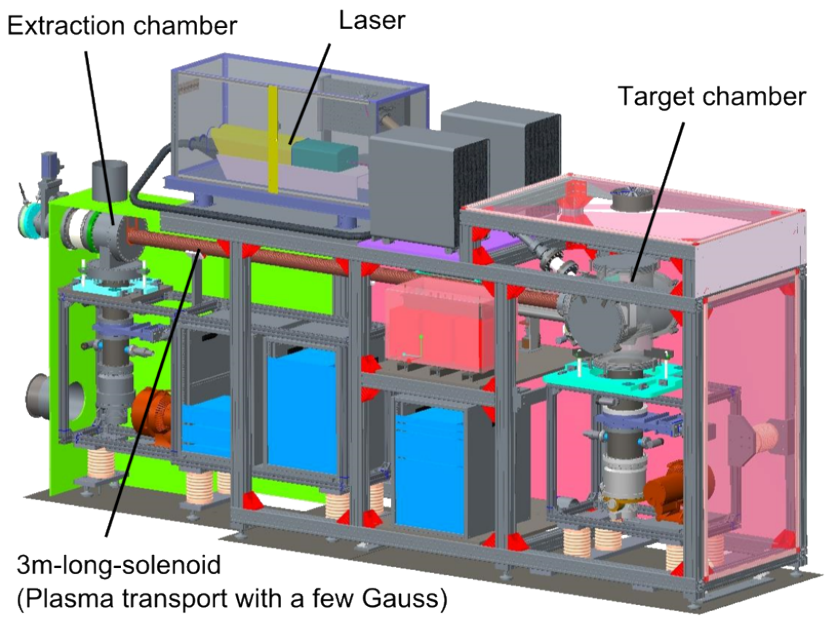

Figure 5.7: *LION Laser Ion Source of Brookhaven National Laboratory*

Laser

This laser is equipped with two identical Q-switched Nd:YAG laser oscillators (850 mJ/6 ns at FWHM, 1064 nm wavelength). A built-in laser combiner merges the two laser beam into one laser path to aim at the same position. The laser is focused on a solid state target plate. The laser spot size on the target is 5 mm in diameter. The different laser energy of 500 $\sim$ 700 mJ is used depending on the species to achieve singly charged ions.

Target Chamber

In the target chamber, several targets are held on a tungsten target holder. Figure 2 shows the target holder with Au, C, Fe, and Ta targets from right. The target holder is mounted on a x-y linear stage, which has the maximum travel range of 250 mm and 50 mm in horizontal and vertical direction, respectively. The x-y stage allows the laser to hit different target materials.

Plasma Transport Line and Extraction Chamber

A 3-m-long solenoid magnet guides laser-produced plasma to an extraction chamber. The solenoid magnet is used to reduce the diverging angle of expanding plasma. Typical magnetic field to be used is a few Gauss [70]. With this drift length, ion beam with pulse width of a few hundreds of microseconds is achieved. Ions are extracted at the extraction chamber, and transported to following applications.

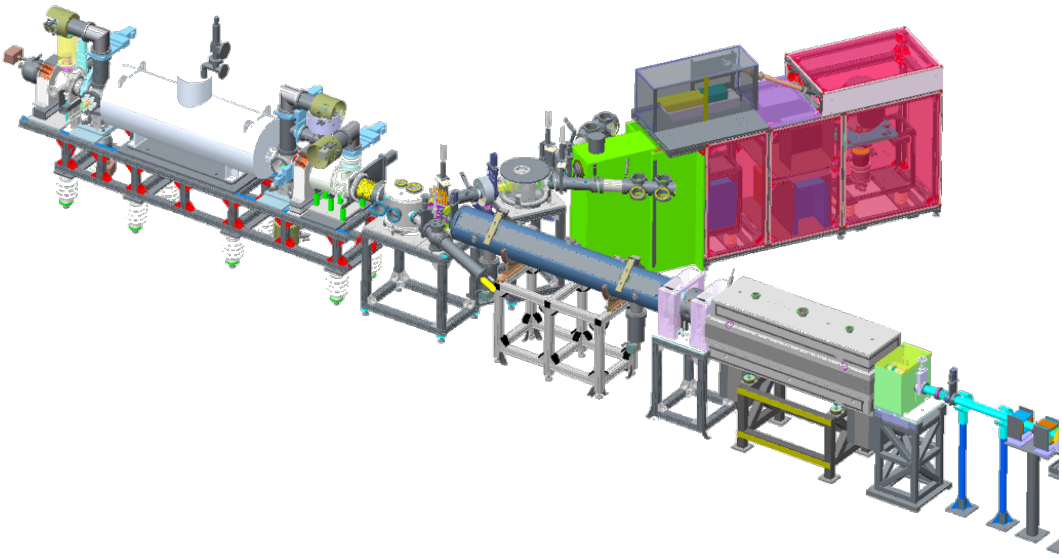

Figure 5.8: *View of Laser Ion Source LION with EBIS system*

The Laser Ion Source of BNL is setted to produce Au^{1+} and thank the use of EBIS system obtain Au^{32+}. Using higher laser intensity should be possible to obtain the beam with good properties to be injected directly in RFQ LINAC. The study in the previous chapter may be suitable for this application. It has been seen, for example, that using laser intensity from $10^9 W/cm^2$ up to $10^{12} W/cm^2$ and targets covered with gold film of 750 nm, was produced a plasma of only gold with charge states up to 14+ using higher intensity. Using lower thicknesses should be possible to obtain a cocktail beam with a mix of Al and Au ions with the same charge state for lower intensity. Further studies may be carried out to determine the best Laser-target combination to obtain a system that bypass the use of EBIS and inject direct ion within the RFQ.

5.2 Superconducting Cyclotron

A cyclotron is a circular accelerator with a constant magnetic field magnitude and constant RF frequency. Cyclotrons have large-area magnetic fields to allow acceleration from low energy near the centre to the output energy near the outer edge of the cyclotron. The field bends the particle trajectory into a circular path, allowing many accelerations from the same accelerating gap. Synchronisation between the oscillating accelerating fields and the revolution frequency of the particles can be achieved as long as the particle velocity is low enough that relativistic effects are negligible. For a non-relativistic particle in a uniform vertical magnetic field, the balance of the centrifugal force with the magnetic force gives

$$qvB = \frac{mv^2}{r} \tag{5.2.1}$$

$$\omega = \frac{v}{r} = \frac{qB}{m} \tag{5.2.2}$$

such that the angular frequency ω is independent of the particle energy. As the particles accelerate and v increases, the radius r increases proportionally because the cyclotron frequency is constant. This means that ions at different energies travel at different radii in the cyclotron, therefore extraction at a fixed point in the structure necessarily means extraction at a fixed energy. The ions are accelerated in the gap between two electrodes, which are known as dees because of their traditional D-shape. One or both dees are connected to a resonator tuned to oscillate at the cyclotron frequency defined in Equation5.2.2. Fig.5.9 shows dees for a cyclotron and the particle orbits relative to each, in the case where both dees are connected to the RF generator.

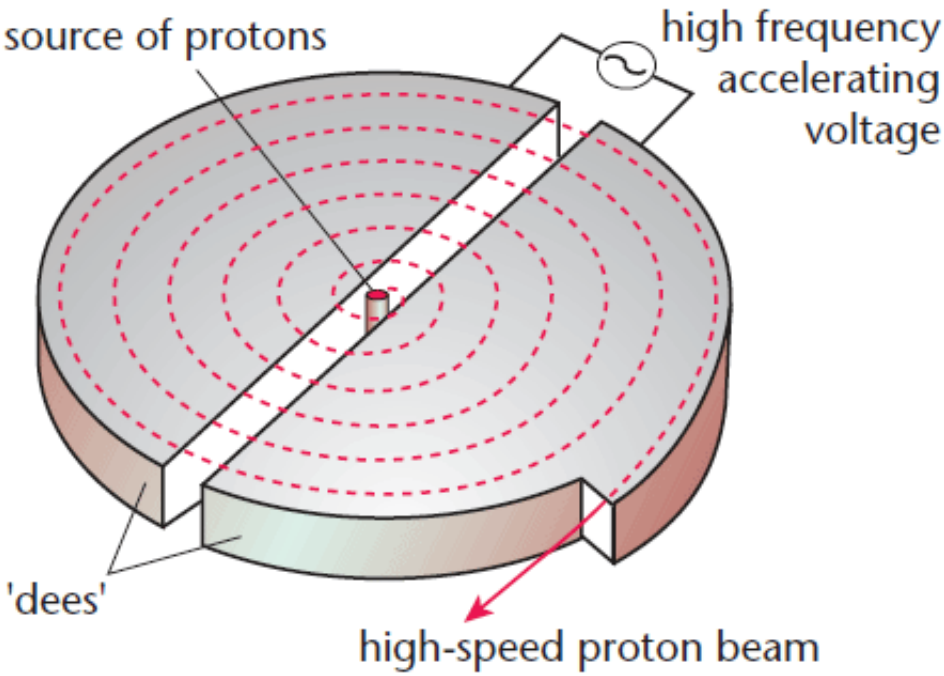

Figure 5.9: *Scheme of a Cyclotron*

As an ion leaves the source near the centre of the cyclotron, it is accelerated by the voltage between the dees—the field at this time is polarised to apply a force in the direction of travel of the particle. As particle energy increases, however, the frequency change since the relativistic increase in the mass beyond a certain energy value for relatively heavy particles is no longer negligible. To maintain the synchronism between the RF and the motion of the accelerating particle, the magnetic field must be varied according to the radius of the orbit.

5.2.1 Orbit stability

The major problem in accelerators is not to accelerate the ions, but to keep the ions on their equilibrium orbit, i.e. the problem of focusing or orbit stability. Ions, guided by the magnetic field, travel a long distance before reaching their final energy. If the ions once hit the dees or vacuum chamber wall, they are lost. Therefore corrective steering forces

must be applied. This force should be automatic for all ions, as it is not possible to steer individual ions. Moreover, the force should be proportional to the deviation. Finally the force should correct both up-down and left-right deviations. Orbit stability is related to the magnetic induction as a function of the radius. This function is described (at least for small variations) by the field index n [71].

$$B(r) = \frac{1}{r^n} \tag{5.2.3}$$

Radial orbit stability is obtained for a field index lower than unity (Fig.5.10)

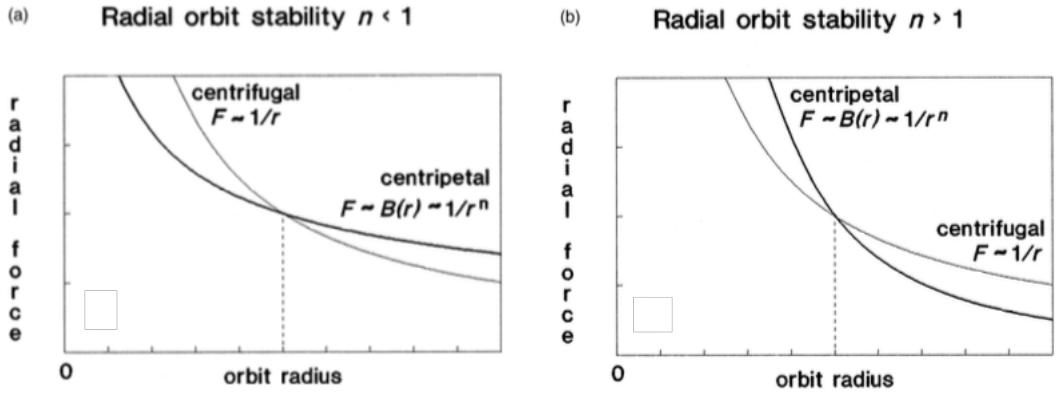

Figure 5.10: *Radial orbit stability (a) and instability (b) for* $n < 1$ *respectively* $n > 1$

The centripetal force F_p, i.e. the Lorentz force, is proportional to the magnetic induction B, and its dependence on the radius r is described by the field index n . The centrifugal force Ff is proportional to the inverse value of the radius r. Both radial forces are balanced for the equilibrium orbit radius. For ions leaving the equilibrium orbit in the mid-plane to the center of the cyclotron ($r = 0$) the centrifugal force overrules the centripetal force. The ions are thus forced to the equilibrium radius again. Reasoning in the same way, ions leaving the equilibrium orbit away from the cyclotron center experience a net centripetal force. Repeating the reasoning for a field index higher than unity, one observes radially unstable orbits. The condition for both axial and radial orbit stability is a field index between zero and unity. It is now clear that the condition for isochronism,

i.e. the magnetic induction increasing with the radius to compensate the relativistic mass increase ($n < 0$) can not be fulfilled in a classic cyclotron. Consequently, the maximum energy of a classic cyclotron is limited.

5.2.2 Isochronous cyclotron

In an isochronous cyclotron a negative field index is applied to compensate the relativistic mass increase. The axial orbit instability, such a magnetic field causes, is overcompensated by strong axially focusing forces. These Thomas forces originate from the particular shape of the magnet poles (Fig.5.11) [71].

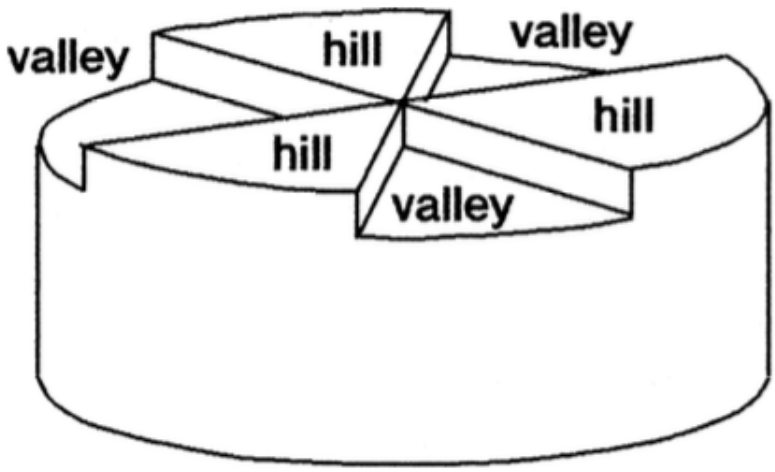

Figure 5.11: *Magnet pole of an isochronous cyclotron, i.e. a sector focussed or AVF (azimuthally varying field) cyclotron plane*

Removing radial sectors (at least 3) from the magnet poles 'hills' and 'valleys' are created. Ions experience a strong magnetic field in the hills (because the N and S pole are closer than for the valleys) and a weak magnetic field in the valleys. In the azimuthal direction, i.e. perpendicular to the radius, along the equilibrium orbit, ions experience an azimuthally varying field, hence an 'AVF cyclotron'.

Figure 5.12: *3-sector superconducting cyclotron of INFN-LNS*

This kind of setup allows to focalize the beam and make stable the orbit.

5.2.3 ECRIS Source

Generally a source of particle for the cyclotron is a plasma obtained from evaporation in ovens, or thanks to microwaves in Electron cyclotron resonance ion source (ECRIS). In a vacuum chamber is maked a vacuum of about 10^{-4} *mbar* in which a magnetic field B is present, microwaves are supplied with a frequency of 2.45 GHz (although recent technologies use frequencies up to 45 GHz). Because of the microwaves there will be some ionization in the gas. These charged charges, due to the magnetic field, will start circular trajectories with frequency equal to that of cyclotron. The matching between the frequency of the microwaves and the cyclotron frequency causes there to be an electron-wave auxiliary ionization effect. In Catania at LNS laboratory are present two ECRIS sources following is reported in Tab the characteristics of CAESAR Source:

Table 5.3: Parameters of RFQ LINAC

Parameter	**Value**
Operating frequency	14 and 18 GHz
Maximum radial field on the wall	1.1 T
Maximum axial field (injection)	1.58 T
Maximum axial field (extraction)	1.35 T
Minimum axial field	0.4 T
Extraction	Accel-Dec, 30kV/12kV Max

The ECRIS source allow to obtain plasma for the accelerator but have a limit, it is not possible to obtain all kind of particles. For example it is impossible to obtain a gas of Ta for the very high melting point, and for this reason it is possible to think to use the Laser Ion Source for Cyclotron.

5.2.4 ECLISSE Project for Cyclotron of INFN-LNS

In Catania at INFN-LNS laboratory is present a superconducting cyclotron employed mainly in charged particle therapy. The cyclotron is a compact three-sector cyclic accelerator that can accelerate ion bands from uranium up to protons to energies up to 80 MeV / A. The pole has a radius of 90 cm and the magnetic field inside it can reach the value of 4.8 T. To obtain such intense magnetic field values, the superconductor cyclotron is equipped with two sets of superconducting coils immersed in the Nb-Ti in a liquid helium bath , at a working temperature of 4.2K. The possibility to produce intense metal ion beams, pulsed or dc mode, by means of an hybrid source, consisting of a Laser Ion Source (LIS) as the 1st stage and of an Electron Cyclotron Resonance Ion Source (ECRIS) as the 2nd stage, was under study at the Laboratori Nazionali del Sud (LNS) [72]. The aim of the experiments at LNS consisted of the minimization of the energy of multiply charged ions, of the maximization of the emitted ion current and of the study of etching rates

at high repetition rates of the laser, the name of project was ECLISSE (ECR ion source Coupled to a Laser Ion Source for charge State Enhancement).

Experiments with Laser Ion Source in INFN-LNS

A 900 mJ/ 9 ns Nd:YAG laser was used in our experiments; single pulse regime and 30 Hz repetition rate regime were used. Unfortunately during the most recent series of tests the maximum laser energy was not higher than about 300 mJ, but yet sufficient to study the low energy, low charge states production regime in which we are interested.

The assembly of the hybrid ion source will be carried out in 2002 with the support of the Nd:YAg laser [72]. In Fig.5.13 a cross section of the plasma chamber (called SERSE) is shown with the metal target placed on a rotating rod in the injection side of the chamber. The laser beam was injected into the beamline from the 0° port of the 90° analysis magnet, on-axis with the extracted beam (the interaction between the laser beam and the beam of highly charged ions extracted from the source is negligible). In Fig.5.14 the cross section of the SERSE plasma chamber is shown with the metal target placed on a rotating rod in the microwave injection side of the chamber. The Nd:YAG laser has been aligned along the normal to the target surface, by means of a He-Ne laser. A focusing lens (4 m focal distance) is placed in air at about 20 cm from the window placed on the 0° flange of the magnet, and a circular beam spot dimension variable from 1 to 3 mm^2 is obtained on the target. Generally, the employed laser repetition rate was 30 Hz or 1 Hz. The optical path of the laser beam was about 8 m and the free path after the lens about 4 m, passing through many beamline elements (slits and extractor electrodes) to hit the target, slightly off-centered, so that its rotation may permit to launch the laser beam over an annular shape.

The rotating rod could be also manually displaced along the source axis (the automatic displacement system was not yet available at that time). The target diameter was 20 mm. It was connected to a -3 kV power supply placed on the high voltage insulated box, so that it can be biased with respect to the source at a voltage variable between 0 and -3

kV. The reason of biasing the target is the following: as there is a narrow window of ion energy distribution which contains ions that can be caught by the ECR plasma, the presence of a retarding potential permits us to adapt the most intense part of the ion energy distribution to that window. In other words, by decelerating ions we may increase the number of ions that can be caught by the ECR plasma. Anyway a large amount of ions are not captured by the plasma, which reflects negatively on the source performance as it makes the chamber pressure higher. We estimated that the ionization efficiency of SERSE was about one order of magnitude lower than for the ionization of gases or oven-evaporated materials, it means conversely that large margins for the improvement of the hybrid ion source are still present. As a matter of fact, the focusing of the laser beam was quite poor, because of the long distance between the lens and the target, then the amount of ablated material could not be minimized, thus generating a large gas load. We have also verified that an adequate laser beam focusing can permit us to get the same amount of ions from the LIS but a lower number of neutrals extracted from the target.

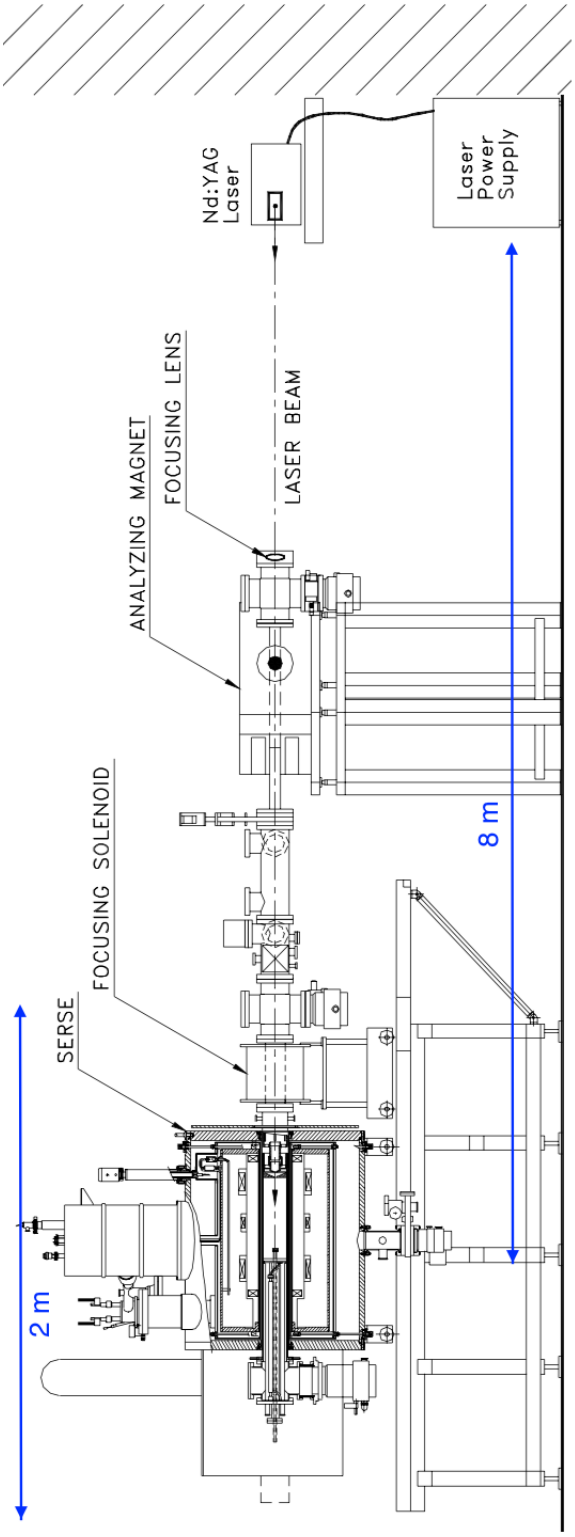

Figure 5.13: *Lateral view of SERSE installation*

5.2.5 Principle of operation of ECLISSE Source

The laser shot travels through the vacuum chamber and hit the target like show in Fig.5.14, the low charge state plasma produced in the interaction expands inside a plasma produced by microwaves (generally O_2, N or Ar). The expansion inside this plasma allows laser generated plasma to increase its charge state several times. At the exit of microwave chamber there is a magnetic 90° selector that allows to study the produced charge states and the beam current.

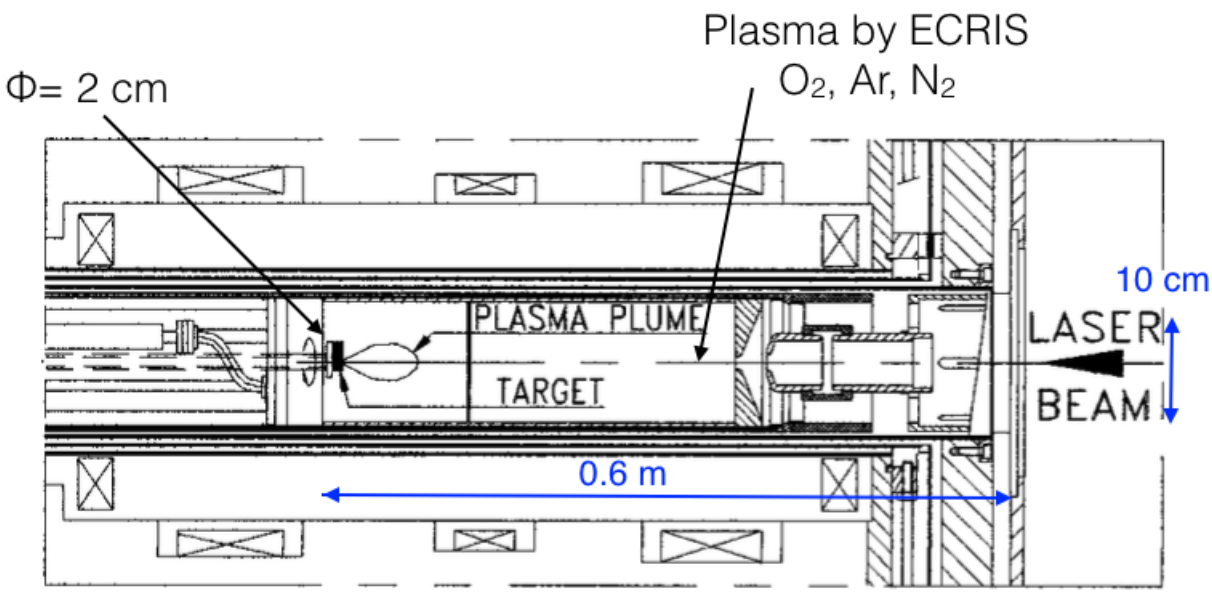

Figure 5.14: *A cross section of the plasma chamber*

Results with gold targets

The first series of results [73] was obtained with a low laser power and a low oxygen gas pressure, about 1 μA of Au^{34+}. A better result was obtained after one day of continuous operation, about 1 μA of Au^{38+} and some Au^{41+} was clearly observed (Fig.5.15) using 20 kV of extraction potential.

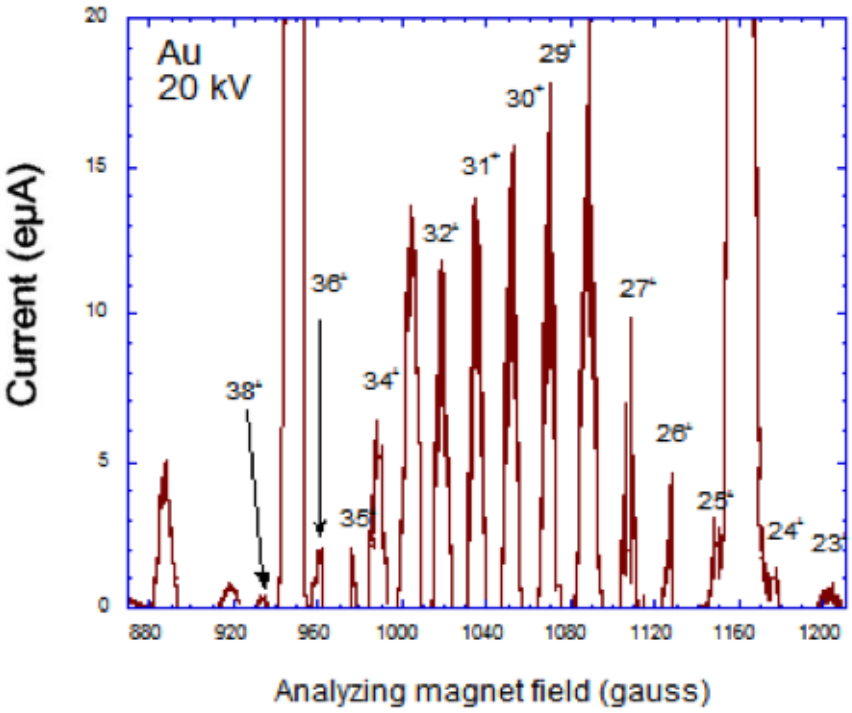

Figure 5.15: *Gold charge state distribution after magnetic selector*

Results with Tantalum targets

The Ta target has a very important role in this discussion, the Ta beam is one of the beam that is impossible to obtain without the use of Laser Ion Source, this difficult is due to the very high melting point of Ta. Using the setup described above we were able to get 40 μA Ta^{25+} and Ta^{26+}, 12 μA of Ta^{31+}, 1 μA of Ta^{33+} (Fig.5.16).

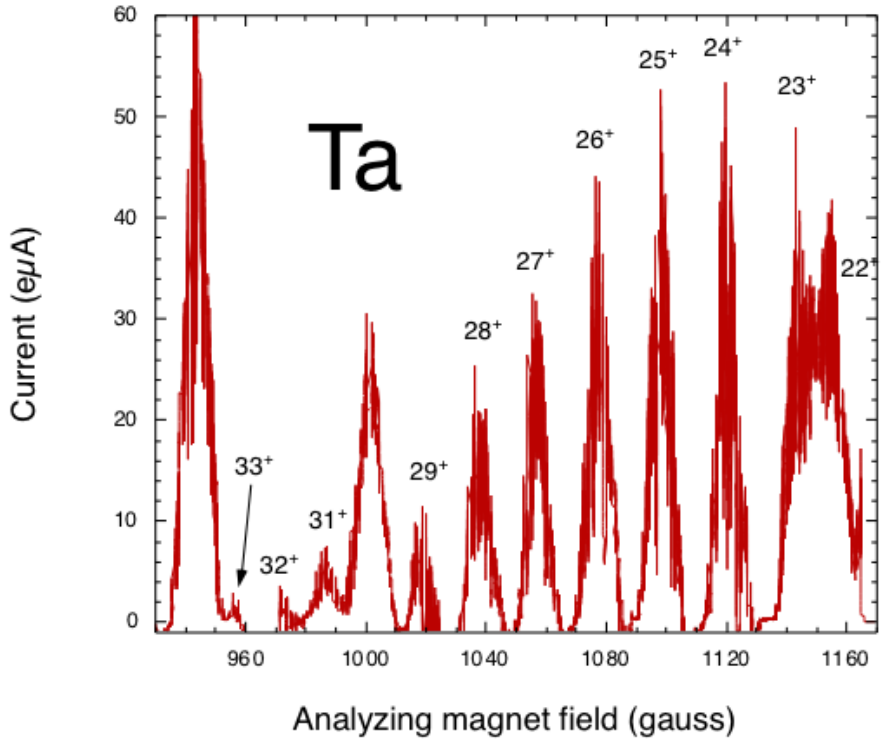

Figure 5.16: *Tantalum charge state distribution after magnetic selector*

These results show that a much higher current can be obtained by means of the ECLISSE method and some additional changes are to be done in order to be rid of the existing limit.

5.2.6 Advantages of Laser Ion Source

Many advantages to use Laser Ion Source for accelerator facility [61]. The first one is that the structure of a laser ion source is simple and permits to exchange very quickly the ion species in use. The Laser allows to produces purer ion beams. The old ion source used neon gas to charge the ions, which meant that neon ions were also present in the ion beam. The beam can consist of ion that should be impossible to produce with traditional source for the high melting point, and in this way can be possible to obtain and accelerate ion of radioactive species.

5.3 Post Acceleration System

The non equilibrium processes inside the plasma are responsible of the non uniform charge distribution and energy spread. To increase the ion energy post acceleration systems can be employed, in addition to the energy the system can increase the focalization of beam.

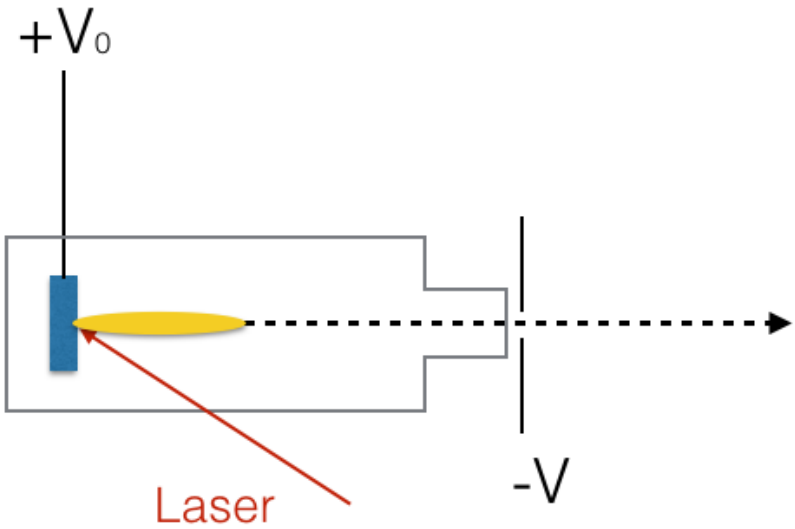

Figure 5.17: *Scheme of a post-acceleration system*

Like we can see, a post acceleration system consist of mainly of a positive bias on target surface and a negative voltage (generally high voltage) in front to the plasma in order to accelerate the positive ion produced by laser-matter interaction [74]. After extraction, ions are accelerated by the intense electric field between the electrodes. If the applied potential difference is V, one would expect that ions reach an energy roughly equal to $Z_i eV$ [75].

5.3.1 Post Acceleration of INFN-LNS

In INFN-LNS of Catania was developed a post-acceleration system in order to accelerate the ions emitted from a plasma obtained by irradiating a solid target with a Nd:YAg laser. It treats of an extraction chamber placed inside the vacuum chamber, the base of this

extractor is placed on an insulator (polymeric material) to insulate the extractor from the vacuum chamber. The extraction chamber is made in aluminium with the shape of parallelepiped 26 cm long and qith 11 cm side. The target is irradiating thanks to the presence of a windows that allows to the laser to go inside the extractor. The target and the expansion chamber are placed at the same electrical potential, that can be set between 0 and +100 kV by a power high voltage supply. The frontal side respect the target are totally open and in front of it, 12 discs 2 mm tick and 10 cm diameter, are aligned to the axe of chamber. Each disc has a central hole of 8 mm in diameter and are all connected on the other one by a resistor of 10 MΩ, in this way the first disc is connected directly with the high voltage and the last one with the ground.

Several experiments [76] were performed in order to study the acceleration of ions using this system. A typical experimental setup is shown in Fig.5.19. A Q-switched Nd:YAG pulsed laser operating with 1064 nm wavelength, 9 ns pulse width and 200 mJ pulse energy (maximum energy selectable up to 900 mJ), in single shot mode, was employed to irradiate Ge and Ti targets in vacuum chamber. The laser beam was focused through a convergent lens on a target placed inside a vacuum chamber. The incidence angle, the spot size and the maximum laser intensity were 45° , 0.5 mm^2 and 10^{10} W/cm^2, respectively.

In the experiment, a ring ion collector (ICR), an annular cup with an inner hole diameter of 15 mm and an external diameter of 25 mm, with a surface of about 314 mm^2, is placed along the normal to the target surface (the direction of maximum ion acceleration) at a target distance of 100 cm. TOF technique is employed by using as a start signal a trigger photodiode induced by the laser shot, and as a stop signal a signal from the ICR ions detectors. Signals are recorded on a fast Tektronics storage oscilloscope with 500 MHz frequency, 2 Gs/s sampling velocity and 50 Ω input resistance.

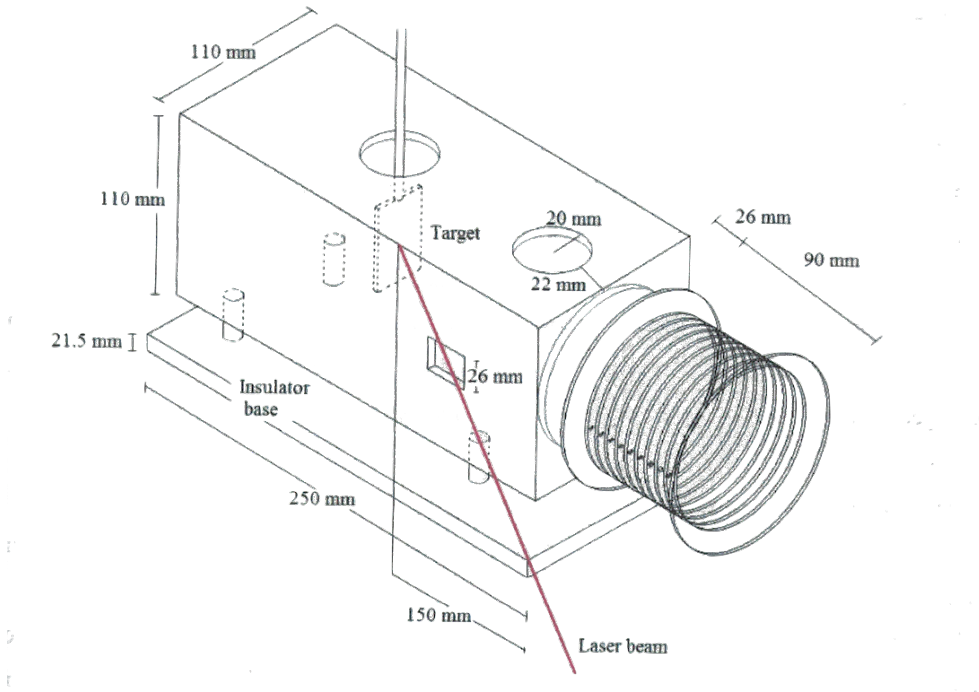

Figure 5.18: *Design plot of post acceleration system of INFN-LNS*

An electrostatic ion energy analyzer (IEA) is used to measure the energy-to-charge ratio of the detected particles emitted from the plasma along the normal to the target surface. IEA spectrometer electro-statically deflects the ions by 90°, so that they are detected by a windowless electron multiplier (WEM). The target-first WEM dynode is 160 cm from the target, and TOF technique is employed for the ion energy measurements. Ion charge states and ion energy distributions were investigated with IEA, which permits to select the energy-to-charge ratio, E/z.

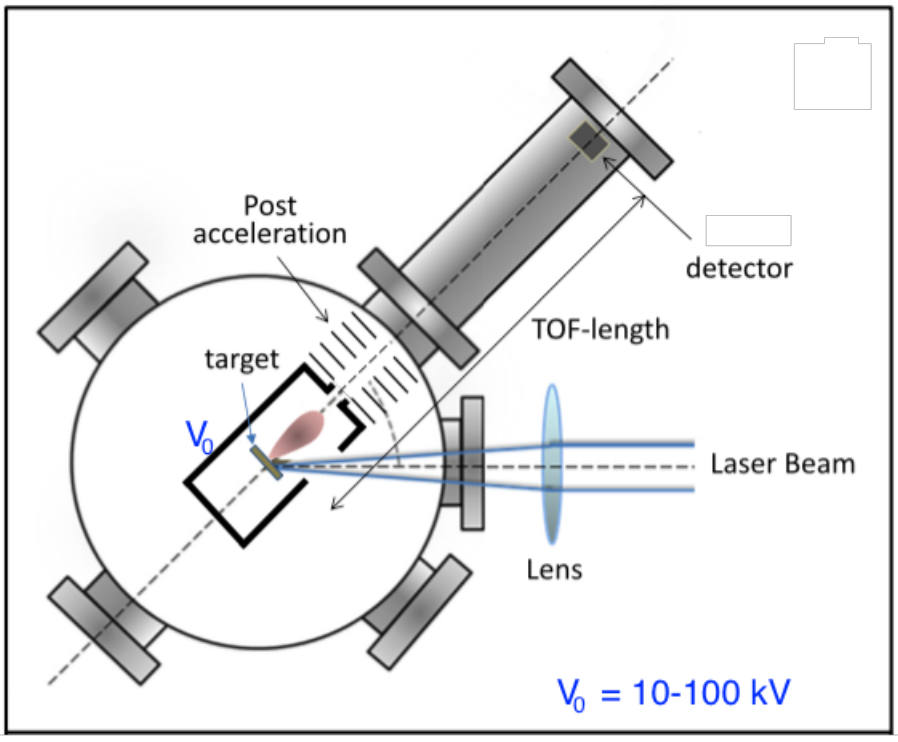

Figure 5.19: *Scheme of experimental setup with post-acceleration system*

Fig.5.20 shows the ICR-TOF spectra for Ge and Ti ion detection without post-acceleration voltage (HV = 0 kV) (a and b) and with the post-acceleration voltage application (HV = 30 kV) (c and d)[76]. When the extraction–acceleration voltage increases, the ICR ion peaks shift towards lower TOF times, indicating that ions are suc- cessfully accelerated by the extraction electric field. In particular, Fig.5.20a and b represents the detected integral ions coming directly from the plasma producing a TOF peak time at about 22 μs and 20 μs for Ge and Ti ion species, respectively. The maximum TOF spectrum peak corresponds to an ion velocity of about $4.5 \cdot 10^4$ m/s for Ge and $5 \cdot 10^4$ m/s for Ti ions. Such velocities indicate a mean kinetic energy of about 765 eV for Ge and 623 eV for Ti ions. Assuming the target-first acceleration disc to be 16 cm, during which the ions are not substantially accelerated by the external electric field, at these energies the Ge and Ti ions spend about 3.6 μs (drift time) and 3.2 μs, respectively, to reach the effective

acceleration zone from the target surface. For comparison, Fig.5.20c and d reports the spectrum obtained by using a voltage acceleration of 30 kV. In this case, the TOF peak is detected at about 7.5 μs and 6 μs for Ge and Ti, respectively. By considering the maximum peak position and by subtracting the drift time, i.e. by considering the real extraction–ICR distance of about 84 cm, it is possible to calculate the new ion velocity due to the post-ion acceleration system. The corresponding average ion energy of about 18 keV and 22 keV is calculable for Ge and Ti ions, respectively. The distributions show a long tail indicating the presence of many ions at lower velocity and a sharp front indicating the presence of faster ions. The evaluation of the initial position of the ion spectra is not simple because of the intense background signals due to photons and electrons hitting the collector. The ion energy corresponding to the maximum half height of the front TOF ion peak is about 90 keV both for Ge and Ti ions, a value corresponding to the 30kV ion acceleration applied to three times ionized atomic species. This last result, indicating the possible presence of three charge state of atomic ionization, finds confirmation in the IEA measure- ments at the incident laser fluence of 34 J/cm^2 hitting Ge and Ti targets. A fourth charge state is also present both for Ge and Ti atoms but its contribution is negligible with respect to the other charge states.

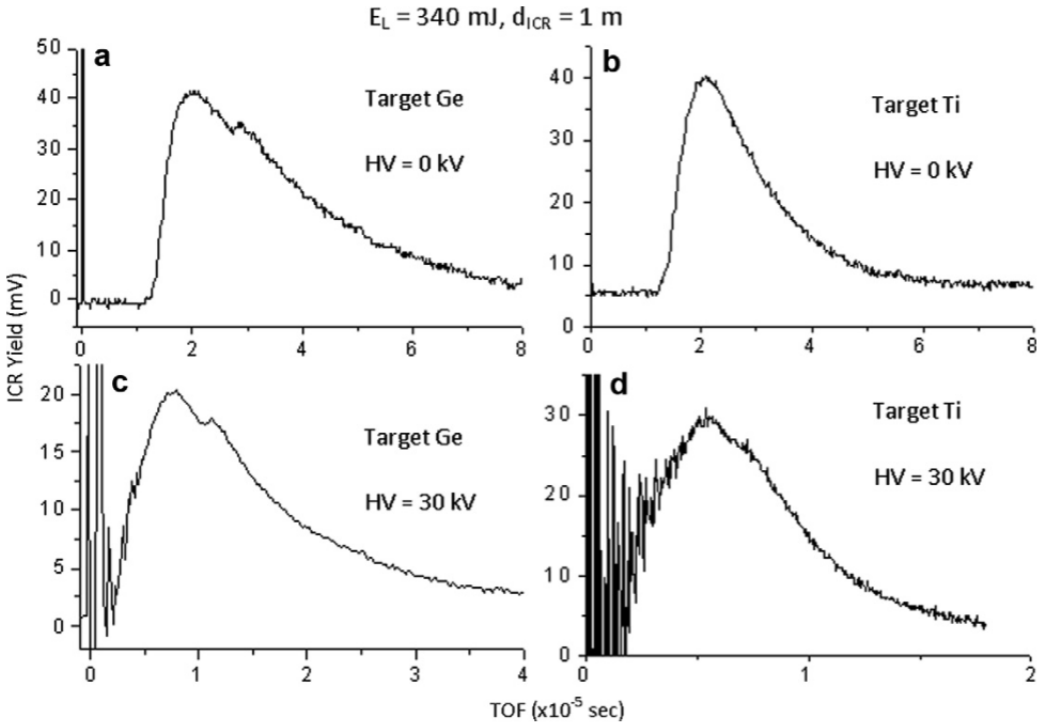

Figure 5.20: *ToF results with and without post acceleration*

The ion energy distributions, obtained by varying the IEA deflection bias, indicate that the ions follow a Boltzmann distribution but it is different for each charge state three charge states. The mean ion energy is about 400 eV, 800 eV and 1200 eV for Ge^{1+}, Ge^{2+} and Ge^{3+}, respectively, as reported in the energy distributions of Fig.5.21a. Similar ion energy distributions are measured for Ti ions. In this case the mean energy is about 360 eV, 720 eV and 1080 eV for Ti^{1+}, Ti^{2+} and Ti^{3+}, respectively, as reported in the energy distributions of Fig.5.21b.

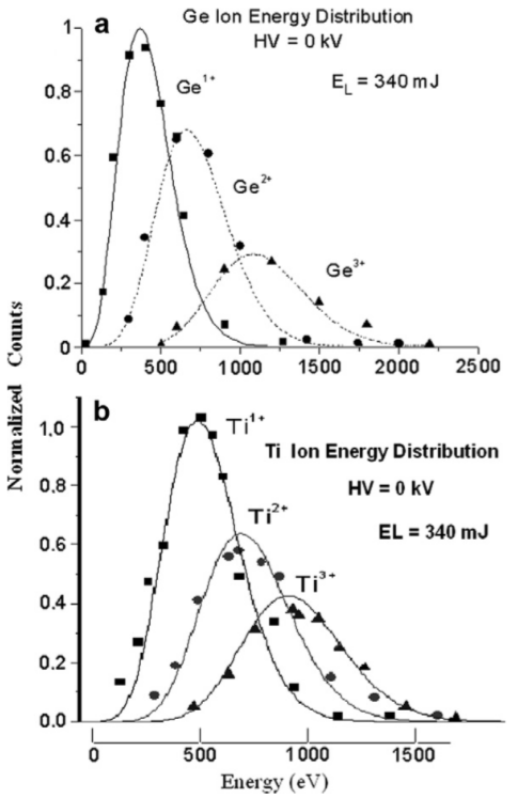

Figure 5.21: *Charge state distribution without post acceleration*

By using the 30 kV acceleration voltage, the IEA ion energy distributions of the post-accelerated ions have been acquired by changing the E/z ratios around the mean energy of 30keV, 60 keV and 90 keV for the three charge states of the two ion species. Three typical IEA spectra, obtained analyzing the post-accelerated Ge ions, are reported in Fig.5.22. The experimental post-accelerated ion energy distributions appear very narrow with a full width half maximum (FWHM) of about 0.8 keV, 1.7 keV and 2.3 keV, for Ge^{1+}, Ge^{2+} and Ge^{3+}, corresponding to an energy resolution $\Delta E/E$ of 2.7%, 2.8% and 2.6%, respectively. In the case of Ti post-acceleration the distribution FWHM is 4.5 keV, 3 keV and 2.5 keV, for Ti^{1+}, Ti^{2+} and Ti^{3+}, corresponding to an energy resolution of 15%, 5% and 2.8%, respectively [77].

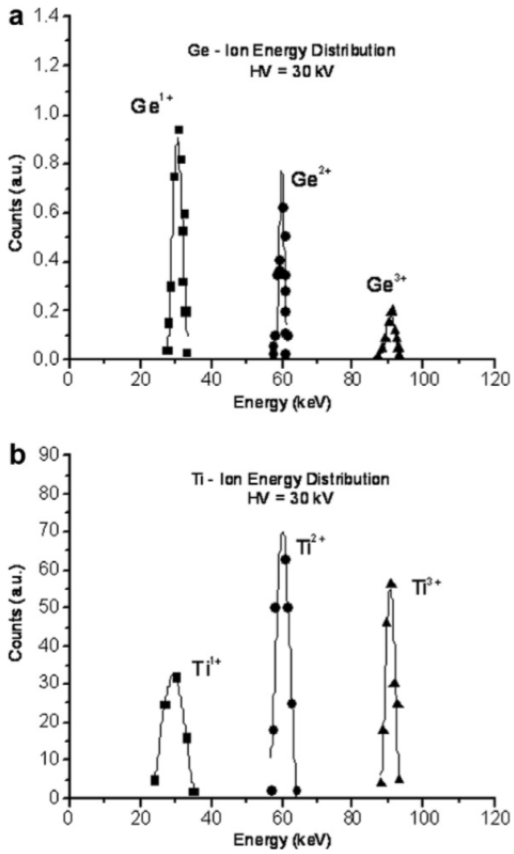

Figure 5.22: *Charge state distribution with 30 kV of post acceleration*

5.3.2 Ion implantation by post acceleration and RBS measurements

The post acceleration system can be used in several applications like for example the ion implantation. Ge ions at energies of 30, 60, and 90 keV were implanted into 50-nm-thick SiO_2 films grown on Si wafers by oxidation in a dry-oxygen ambient at a temperature of 1000 °C. In order to evaluate the deposition and implantation of Ge atoms as well as their position in the SiO_2 layer covering a Si substrate, the Rutherford Backscattering Spectroscopy (RBS) surface analysis is applied. The Stopping and Range of Ions on Matter (SRIM) code (Ziegler, 2010) makes it possible to calculate in SiO_2 the range of

Ge-implanted ions of 26, 46, and 63 nm for 30, 60, and 90 keV, respectively. Fig.5.23 reports a typical RBS spectrum relative to Ge-atom deposition on the SiO_2-substrate surface [77]. It has been obtained using the atoms and neutral species produced by the laser-generated plasma and deposited, without post-acceleration, on the substrate surface.

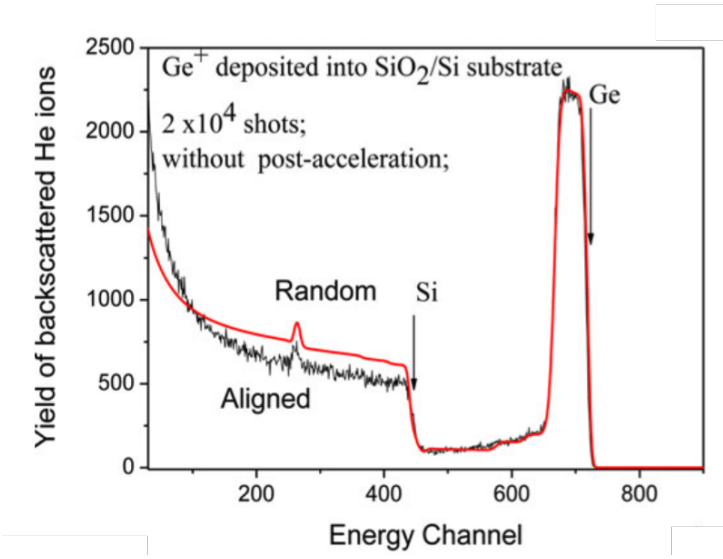

Figure 5.23: *The RBS spectra, 2 MeV α particlesa at* 165° *backscattering, of SiO2/Si substrates deposited by Ge atoms (20,000 laser shots)*

Fig.5.24 and Fig.5.25 report the RBS spectra relative to the Ge ion depth penetration up to 30 nm (Fig.5.24) and 51 nm (Fig.5.25), respectively. The RBS spectra are relative to the deposition of Ge ions produced after 2×10^4 laser shots Fig.5.23, and implantations after 1×10^4 laser shots (Fig.5.24) and 5×10^4 laser shots (Fig.5.25). Moreover, RBS analyses are performed on a randomly oriented substrate (random spectrum) and under the conditions of ion channeling (aligned spectrum). The energy of emitted Ge ions is sufficient to produce a slight damage to the crystalline structure of the substrate due to the high nuclear stopping power of the low-energy Ge ions. A comparison between the reported spectra shows that the peak of the implanted species does not decrease in yield, demonstrating that the interstitial defect and surface amorphization occur as a result of Ge-ion implantation. The little scattering at shallow depths in a near-perfect crystal

is exhibited due to the low thickness of the germanium film deposited on the substrate surface.

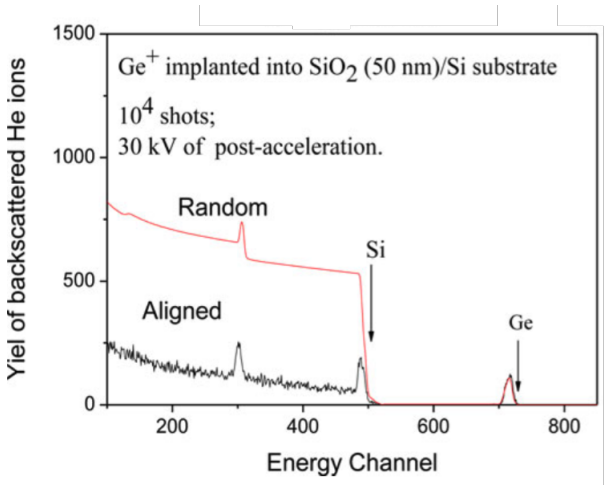

Figure 5.24: *The RBS spectra of SiO2/Si substrates deposited by Ge implantation after 10000 shots*

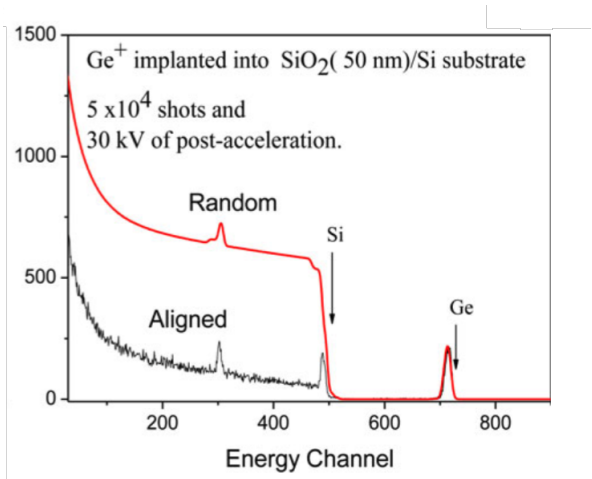

Figure 5.25: *The RBS spectra of SiO2/Si substrates deposited by Ge implantation after 50000 shots*

This study demonstrates that the multi-ion implantation produced by the post-ion acceleration of laser-generated plasma is effective, useful, and promising. The results of

the investigated surface treatment show that the post-acceleration system can be more efficient and cheaper than the conventional methods using ion implanters.

5.3.3 SRIM simulation of Ge implantation

The multi energetic ion implantation in different materials can be followed by using the SRIM simulation program, which allows to determine the range and the straggling of ion implanted as a function of the ion energy. In this case an example of Ge ions in SiO_2 substrate in order to observe a simulated results that can be ontained during an experiment. The Ge ions were consireded emitted from a plasma with maximum charge state 3+, using a post acceleration of 30 kV the ions will have energy 30 keV, 60 keV and 90 keV. The results of simulations are overlapped and shown in Fig.5.26.

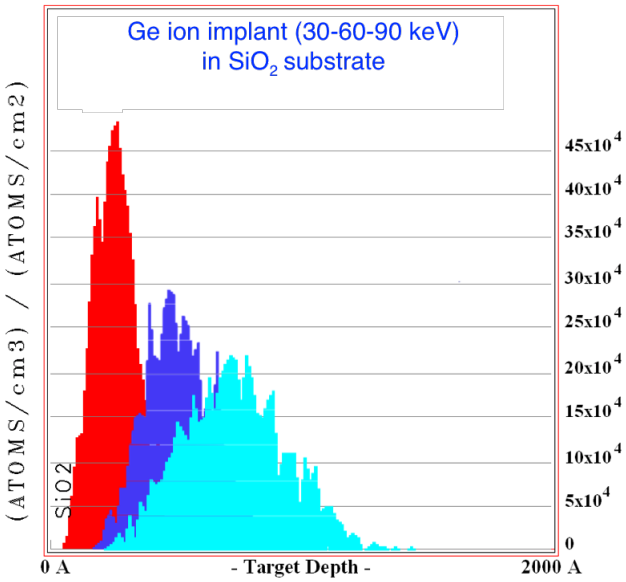

Figure 5.26: *SRIM simulation relatively to the ion implantation of* Ge^{1+} *of 30 keV,* Ge^{2+} *of 60 keV,* Ge^{3+} *of 90 keV*

From these simulation it is possible also to evaluate the maximum depth of implantation that in this case is 120 nm due to the Ge^{3+} of 90 keV.

5.4 Laser Ion Acceleration

5.4.1 Target Normal Sheath Acceleration

A high ion acceleration can be produced by the interaction between high intensity pulsed lasers and thin metallic foils. The high energy electrons, generated on the front surface of a thin foil, penetrate into the target, cross the target-vacuum back interface, and generate perpendicularly to the rear side of the positively charged target a high electric field. This field, with strength of the order of 10^{12} V/m, accelerates the ions emitted from the rear face up to kinetic energies of the order of tens of MeVs [78]. This process is one of the most investigated mechanisms of ion acceleration, and it is well-known as target normal sheath acceleration (TNSA) regime. The properties of the laser-generated plasma and the charge separation responsible of the ion driving acceleration strongly depend on the laser parameters, irradiation conditions, and target properties.

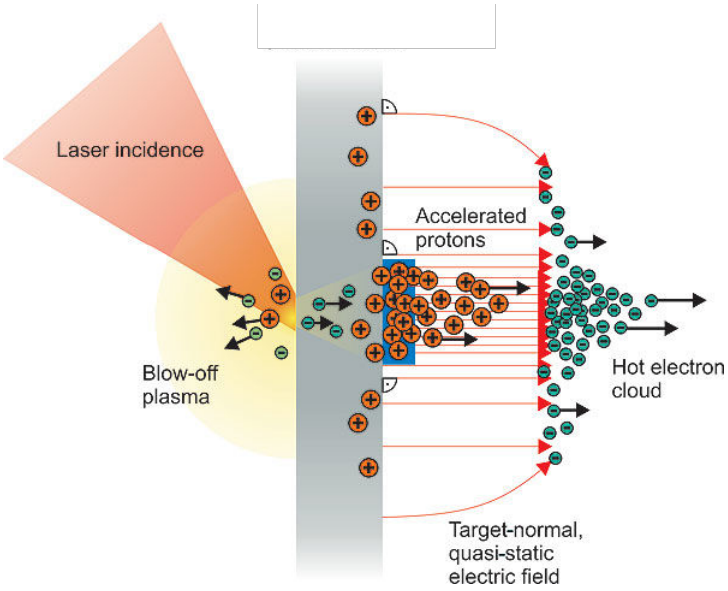

Figure 5.27: *TNSA scheme of interaction*

The characterization of energetic ions is important to clarify the basic mechanism of the interaction and, moreover, to determine future development of table-top low–cost

sources of high energetic particles such as fs lasers able to reach a high intensity (10^{18-19} W/cm^2) by mean the concentration of moderate energies (100 mJ) in ultra-short pulses (20–50 fs) TNSA regime uses foils with a thickness ranging between 1 and 30 microns and generally permits to accelerate ions, in direction normal to the target surface, above 1 MeV per charge state [22]. The parameters of the laser-generated plasma depends strongly on the kind of used laser, enhancing the electron temperature and density with the $I\lambda^2$ factor, where I is the laser intensity and λ the laser wavelength. Moreover, the irradiation conditions control the plasma parameters, for example the laser focal point (LFP) is crucial to develop high electric field of ion acceleration in the rear foil so as the use of p-polarized light (P-PL) can be employed to excite plasma waves enhancing the laser absorption in the plasma or not, depending on the incident angle of the laser light. In this context, the use of nanoparticles and nanostructures in a thin foil may play an important role on the first instants of laser-matter interaction, enhancing the laser absorption coefficient and inducing resonant absorption effects.

5.4.2 Experiments in High Laser Intensity facilities

Fig.5.28 shows a comparison between two spectra obtained irradiating Au foils and Au foil+ Foam using the Laser Eclipse a Ti:Sapphire TW Laser System present at Centre Laser Intenses et Applications (CELIA) laboratory in France. The experiment was carried out using 39 fs pulse duration, 800 nm wavelength, 10^{13} W/cm^2 pedestal intensity, $9.5\mu m$ focal spot diameter, 10^{18} W/cm^2 intensity. The pedestal duration is about 7 ps, while the high laser pulse exhibits duration of 39 fs. The laser is focused by f/3 off-axis parabolic metal mirror and hits p-polarized onto the target with an angle selectable between 0° and 60° . Measurements were usually performed using pulse energy 120 mJ.

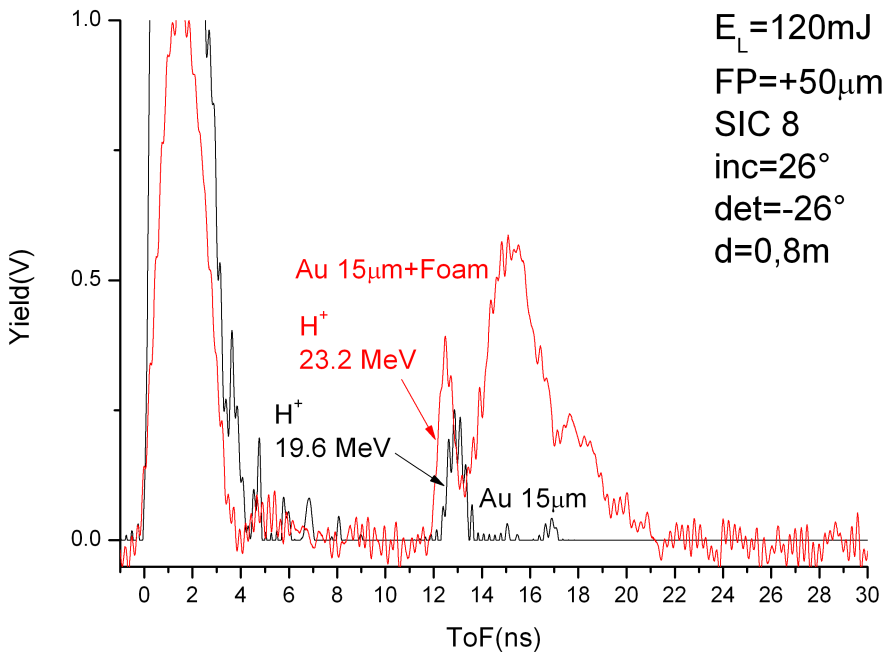

Figure 5.28: *Comparison between two spectra obtained at* $10^{18} W/cm^2$ *laser intensity, targets of Au and Au+ foam*

Like said above, also the irradiation conditions control the plasma parameters are very important. Fig.5.29 shows four typical SiC-TOF spectra relative to the forward plasma emission obtained in condition of optimal ion acceleration irradiating Au targets at 0 incidence angle by 111 mJ and different focal positions: 25 μm, 50 μm, 75 μm, and 100 μm [79]. It is possible to observe that very different spectra are obtained using different focal positions with respect to the target surface and in particular conditions optimal ion acceleration is obtained. Using FP $= 0$ μm, the ion peaks are under the minimum limit of detection or are comparable with the background signal. Using FP $= 25$ μm, the proton peak is well detectable at 15 ns, corresponding to a kinetic energy of 15.5 MeV, with 66mV yield, using FP$= 50$ μm, the spectrum appears similar to the previous: proton peak is detectable to 14.9 ns, corresponding to a kinetic energy of 15.7 MeV, with 73mV yield, with

FP=75μm, the proton peak grows at a value higher than the photopeak, corresponding to 400mV yield and at last FP=100 μm, the proton peak decreases in energy and yield, in fact it appears slightly detectable at 18.2 ns, corresponding to 10.5 Me V, with 3.9 mV yield and extending up to low energies.

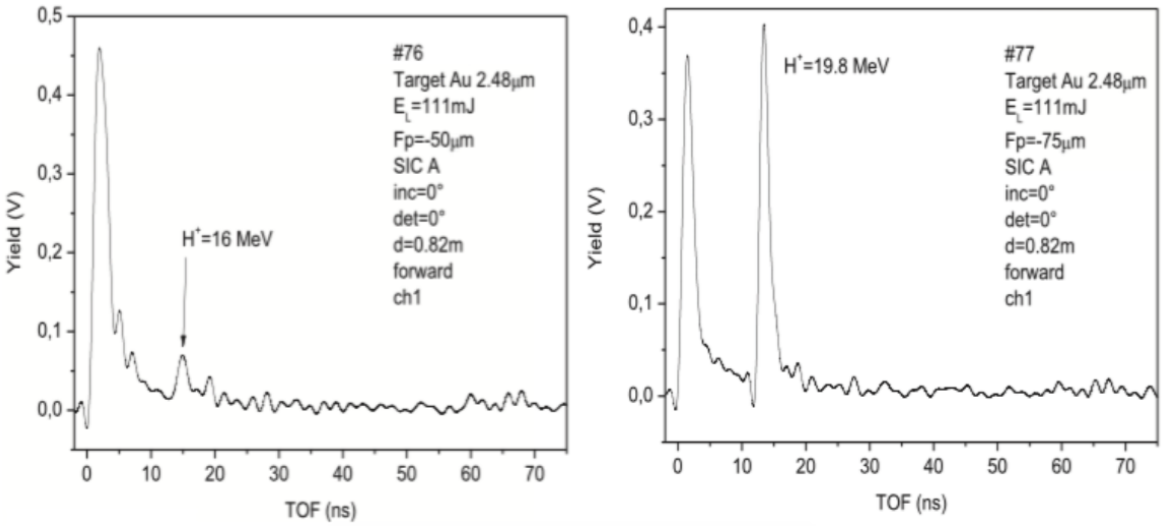

Figure 5.29: *SiC-TOF spectra relative to the forward plasma emission at 0 of 2.48 lm Au foils at different focal distances of -50μm and -75 μm.*

Fig.5.30 shows a comparison between two spectra obtained irradiating pure PE and PE + Au NP using the PALS iodine laser operating at 10^{16} W/cm^2, 1315 nm wavelength, 300 ps pulse duration, and 75 μm spot diameter [80]. In this case, TOF spectra are acquired using the SiC detector placed along the normal to the target surface at 60 cm distance from the target. The maximum proton energy, calculable from the front of the ion yield, is 1.0 MeV and 4.68 MeV for pure PE and for the polymer with Au NP embedded, respectively. Thus the ion acceleration is strongly increased in the second target because probably Surface Plasmon Resonance (SPR) absorption effects occur in the laser-matter interaction enhancing the plasma temperature and density. The result of 4.68 MeV for protons is one of the more energetic ion acceleration obtained using this laser at the optimal focal condition of –100 μm, i.e. 100 μm in front of the target surface. From the

point of view of the ion yield, it seems that the yield remains approximately the same in the two different plasmas.

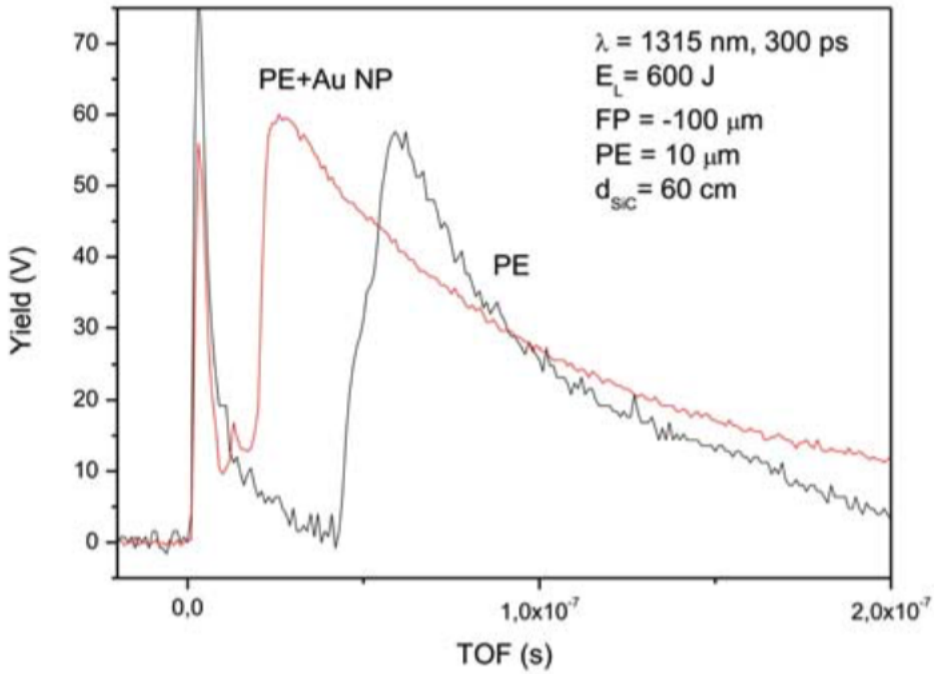

Figure 5.30: *TOF spectra comparison of ions accelerated at high laser intensity (*10^{16} *W/cm*^{2}*, 300 ps) irradiating pure PE and PE+Au NP and detecting in TNSA regime*

5.4.3 Advantages to use advanced targets

Thus, observing the literature data reporting the trend of the ion acceleration value as a function of the $I\lambda^2$ parameter, our measurements demonstrate that nonlinear effects induced by "advanced" targets can ensue the increasing of about two orders of magnitude the expected acceleration values. Fig.5.31 shows the law scale for ion acceleration, for comparison, our measurements, obtained by varying the laser pulse energy between 550 and 600 J, the focal position between 0 and -100 μm and using "advanced targets" with thickness ranging between 10 and 15 micron. The comparison indicates that the use of special advanced high absorbent targets increases the ion acceleration of about one order

of magnitude [81], i.e., to values normally expected only using fs lasers at intensity higher than 10^{18} W/cm^2 [82], [83], [84].

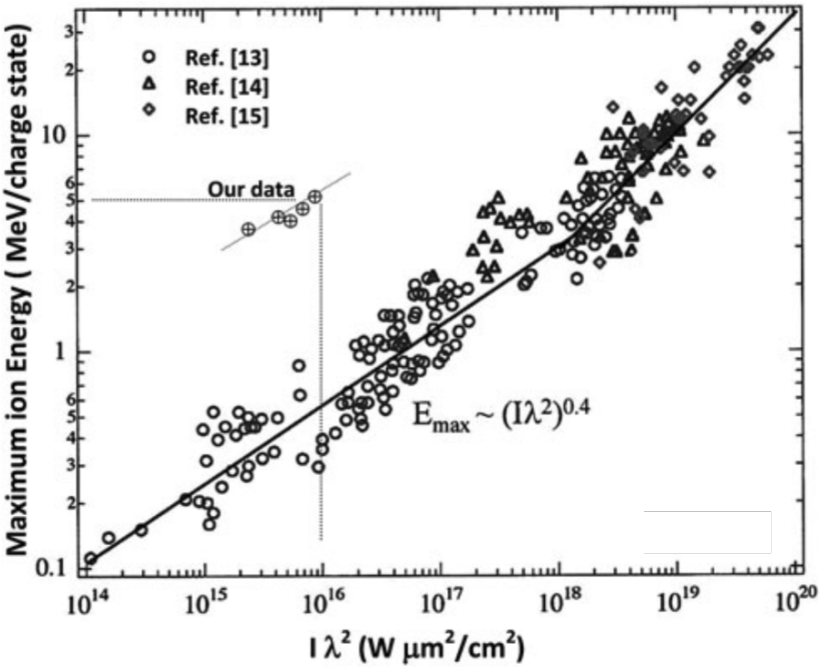

Figure 5.31: *Comparison between the law scale plot by Spencer et al. (2001) and our measurements obtained using "advanced" targets irradiated at* 10^{16} W/cm^2 *laser intensity.*

Conclusions

This thesis was focalized on the study of the non equilibrium plasma produced by pulsed laser interaction with solid target in vacuum condition. The work was performed in several laboratories, mainly in Messina plasma laboratory and in Brookhaven National Laboratory. Were described a series of possible diagnostics that can be employed in plasma study, in chapter 4 for the study of coated target were performed mainly measurements using Ion Collector and Ion Energy Analyzer in time of flight configuration for the study of ion energy distributions. It is possible to found several applications of plasma producing by laser matter interaction. The first application is the Laser Ion Source (LIS) that results very interesting to replace the traditional sources. They work in different ways to produce useful ion beams. For example the commonest are the Electron Cyclotron Resonance Ion Source (ECRIS), Electron Beam Ion Source (EBIS), RF or Microwave plasma ion source and others. All these source have their advantages and disadvantages. A LIS can be employed replacing these Ion Source because present many advantages. A very important one is the possibility to obtain high current ion beam, several order of magnitude higher compared with old sources. The possibility to obtain any kind of ion beam without limitation like the melting point of some metals. The structure of a laser ion source is simple and another advantage of LIS is that it produces purer ion beams. The old ion source used neon gas to charge the ions, which meant that neon ions were also present in the ion beam.

Possible application is the new system for the ion acceleration. By using of new laser system with intensity of 10^{20} W/cm^2 it is also possible to accelerate ions up to several

MeV per charge state. Irradiating thin target of the order on some μm it is possible to produce a plasma in forward direction (to the respect the laser beam) and to reach energy for protons of the order of 10 or more MeV. The energy of protons (or generally heavy ions) is an important research because the future of many fields of the Physics can be improved by using this new laser ion source. For example in the Nuclear Research field a proton beam or other adrons can be used for the study of nuclear reaction or in medicine high energy protons (or Carbon for example) can be employed for cancer terapy.

Other possible application is the ion implantation, the ion emitted from plasma laser-generated can be used in order to implant ions in materials. The implantation is a very interesting application, the possibility to work in repetition rate permits to obtain a beam of ion that can be create a layer of deposited nmaterial at several depths. The main advantage is that, the ion beams are multi-energetic with a big energetic spread, this means that the ions can be implanted at differents depths inside the substrate, this is different from traditional implantes where the ion beam is monoenergetic and if you want obtain different depth we have to change the setup after any treatment.

Development and optimization of laser systems and the study of advanced targets is very important to improve the applications described above. The improvements at these applications should be useful to reach new discoveries in many research fields and in industrial and medical applications, for example. Another improvement that should be reach is the optimization of diagnostic techniques in order to obtain systems able to analyze very quickly energetic plasma composed of several charge states and atomic species.

Bibliography

[1] Claudio Chiuderi and Marco Velli. *Fisica del Plasma: Fondamenti e applicazioni astrofisiche*. Springer Science & Business Media, 2012.

[2] Wolfgang Lotz. An empirical formula for the electron-impact ionization cross-section. *Zeitschrift für Physik A Hadrons and Nuclei*, 206(2):205–211, 1967.

[3] Wolfgang Lotz. Electron binding energies in free atoms. *JOSA*, 60(2):206–210, 1970.

[4] Grigory D Shirkov and Günter Zschornack. *Electron impact ion sources for charged heavy ions*. Springer Science & Business Media, 2013.

[5] Danilo Giulietti and Leonida A Gizzi. X-ray emission from laser-produced plasmas. *La Rivista del Nuovo Cimento (1978-1999)*, 21(10):1–93, 1998.

[6] Gianluca Pucella and Sergio E Segre. *Fisica dei plasmi*. Zanichelli, 2010.

[7] Richard O Dendy. *Plasma physics: an introductory course*. Cambridge University Press, 1995.

[8] Isak I Beilis. Metallic plasma production by laser ablation. *Radiation Effects & Defects in Solids*, 163(4-6):317–324, 2008.

[9] Chantal Boulmer-Leborgne, Joerg Hermann, and Bernard Dubreuil. Plasma formation resulting from the interaction of a laser beam with a solid metal target in an ambient gas. *Plasma Sources Science and Technology*, 2(3):219, 1993.

[10] II Beilis. Mechanism of laser plasma production and of plasma interaction with a target. *Applied physics letters*, 89(9):091503, 2006.

[11] Claus Emmelmann, Marc Kirchhoff, and Nikolai Petri. Development of plasma-laser-hybrid welding process. *Physics Procedia*, 12:194–200, 2011.

[12] Yanyan Zheng, Chengdong Xiong, Zhecun Wang, Xiaoyu Li, and Lifang Zhang. A combination of co_2 laser and plasma surface modification of poly (etheretherketone) to enhance osteoblast response. *Applied Surface Science*, 344:79–88, 2015.

[13] Shyjumon Ibrahimkutty, Philipp Wagener, Tomy dos Santos Rolo, Dmitry Karpov, Andreas Menzel, Tilo Baumbach, Stephan Barcikowski, and Anton Plech. A hierarchical view on material formation during pulsed-laser synthesis of nanoparticles in liquid. *Scientific reports*, 5, 2015.

[14] Boris Sharkov and Richard Scrivens. Laser ion sources. *IEEE Transactions on plasma science*, 33(6):1778–1785, 2005.

[15] IN Zavestovskaya, OA Glazov, NN Demchenko, and NA Menkova. Threshold characteristics of ultrashort laser pulse ablation of metals. In *Frontiers of plasma physics and technology. Proceedings of an international conference*, 2008.

[16] L Torrisi, A Borrielli, and D Margarone. Study on the ablation threshold induced by pulsed lasers at different wavelengths. *Nuclear Instruments and Methods in Physics Research Section B: Beam Interactions with Materials and Atoms*, 255(2):373–379, 2007.

[17] L Torrisi, A Picciotto, L Andó, S Gammino, D Margarone, L Láska, M Pfeifer, and J Krása. Pulsed laser ablation of gold at 1064 nm and 532 nm. *Czechoslovak Journal of Physics*, 54(3):C421–C430, 2004.

[18] Andrea Macchi, Marco Borghesi, and Matteo Passoni. Ion acceleration by superintense laser-plasma interaction. *Reviews of Modern Physics*, 85(2):751, 2013.

[19] M Mahdavi and SF Ghazizadeh. An investigation on the effect of ponderomotive force during laser-plasma interactions on plasma characteristics and laser propagation. *The African Review of Physics*, 8, 2013.

[20] L Torrisi. Coulomb-boltzmann-shifted distribution in laser-generated plasmas from 10^{10} up to 10^{19} w/cm^2 intensities. *Radiation Effects and Defects in Solids*, 171(1-2):34–44, 2016.

[21] G Ceccio, L Torrisi, and M Cutroneo. Advanced targets preparation for tnsa laser irradiation and their characterization. *Journal of Instrumentation*, 11(04):C04017, 2016.

[22] Lorenzo Torrisi. Ion acceleration from intense laser-generated plasma: methods, diagnostics and possible applications. *Nukleonika*, 60(2):207–212, 2015.

[23] L Torrisi, M Cutroneo, L Calcagno, M Rosinski, and J Ullschmied. Tnsa ion acceleration at 10^{16} w/cm^2 sub-nanosecond laser intensity. In *Journal of Physics: Conference Series*, volume 508, page 012002. IOP Publishing, 2014.

[24] Andrea Macchi and Carlo Benedetti. Ion acceleration by radiation pressure in thin and thick targets. *Nuclear Instruments and Methods in Physics Research Section A: Accelerators, Spectrometers, Detectors and Associated Equipment*, 620(1):41–45, 2010.

[25] Andrei Seryi. *Unifying physics of accelerators, lasers and plasma.* CRC Press, 2015.

[26] E Woryna, P Parys, J Wołowski, and W Mroz. Corpuscular diagnostics and processing methods applied in investigations of laser-produced plasma as a source of highly ionized ions. *Laser and Particle beams*, 14(3):293–321, 1996.

[27] Lorenzo Torrisi, Gaetano Foti, Lorenzo Giuffrida, Donatella Puglisi, J Wolowski, J Badziak, P Parys, M Rosinski, Daniele Margarone, J Krasa, et al. Single crystal

silicon carbide detector of emitted ions and soft x rays from power laser-generated plasmas. *Journal of Applied Physics*, 105(12):123304, 2009.

[28] M Cutroneo, P Musumeci, M Zimbone, L Torrisi, F La Via, D Margarone, A Velyhan, J Ullschmied, and L Calcagno. High performance sic detectors for mev ion beams generated by intense pulsed laser plasmas. *Journal of Materials Research*, 28(1):87–93, 2013.

[29] L Torrisi, A Sciuto, L Calcagno, P Musumeci, M Mazzillo, G Ceccio, and A Cannavò. Laser-plasma x-ray detection by using fast 4h-sic interdigit and ion collector detectors. *Journal of Instrumentation*, 10(07):P07009, 2015.

[30] Jeffrey Dellert Kmetec. Ultrafast laser generation of hard x-rays. *IEEE journal of quantum electronics*, 28(10):2382–2387, 1992.

[31] Peter H Dawson. *Quadrupole mass spectrometry and its applications*. Elsevier, 2013.

[32] Philip E Miller and M Bonner Denton. The quadrupole mass filter: basic operating concepts. *J. Chem. Educ*, 63(7):617, 1986.

[33] A Torrisi, M Cutroneo, ED Castrizio, and L Torrisi. Laser ablation coupled to mass quadrupole spectrometry for analysis in the cultural heritage. In *Journal of Physics: Conference Series*, volume 508, page 012025. IOP Publishing, 2014.

[34] L Torrisi, M Cutroneo, and G Ceccio. Effect of metallic nanoparticles in thin foils for laser ion acceleration. *Physica Scripta*, 90(1):015603, 2014.

[35] N Zhang, F Sun, L Zhu, MP Planche, H Liao, C Dong, and C Coddet. Electron temperature and density of the plasma measured by optical emission spectroscopy in vlpps conditions. *Journal of thermal spray technology*, 20(6):1321–1327, 2011.

[36] XT Wang, BY Man, GT Wang, Z Zhao, Y Liao, BZ Xu, YY Xia, LM Mei, and XY Hu. Optical spectroscopy of plasma produced by laser ablation of ti alloy in air. *Journal of applied physics*, 80(3):1783–1786, 1996.

[37] WL Wiese, MW Smith, and BM Miles. Atomic transition probabilities. volume 2. sodium through calcium. Technical report, NATIONAL STANDARD REFERENCE DATA SYSTEM, 1969.

[38] Glenn F Knoll. *Radiation detection and measurement*. John Wiley & Sons, 2010.

[39] Katherine Walden. Bulk etch rate properties of naoh/ethanol as a cr-39 nuclear track detector etchant. 2009.

[40] A Casal, R Cerrato, MP Mateo, and G Nicolas. 3d reconstruction and characterization of laser induced craters by in situ optical microscopy. *Applied Surface Science*, 374:271–277, 2016.

[41] L Torrisi, L Andò, S Gammino, J Kràsa, and L Laska. Ion and neutral emission from pulsed laser irradiation of metals. *Nuclear Instruments and Methods in Physics Research Section B: Beam Interactions with Materials and Atoms*, 184(3):327–336, 2001.

[42] C Altana, A Muoio, F Schillaci, GA P Cirrone, G Lanzalone, S Tudisco, F Brandi, G Cristoforetti, P Koester, L Fulgentini, et al. Thomson parabola spectrometer: A powerful tool for on-line plasma analysis. In *Advancements in Nuclear Instrumentation Measurement Methods and their Applications (ANIMMA), 2015 4th International Conference on*, pages 1–4. IEEE, 2015.

[43] RF Schneider, CM Luo, and MJ Rhee. Resolution of the thomson spectrometer. *Journal of applied physics*, 57(1):1–5, 1985.

[44] Joseph Ladislas Wiza. Microchannel plate detectors. *Nuclear Instruments and Methods*, 162(1-3):587–601, 1979.

[45] Hugo Bouchard, Frédéric Lacroix, Gilles Beaudoin, Jean-François Carrier, and Iwan Kawrakow. On the characterization and uncertainty analysis of radiochromic film dosimetry. *Medical physics*, 36(6):1931–1946, 2009.

[46] CG Freeman, G Fiksel, C Stoeckl, N Sinenian, MJ Canfield, GB Graeper, AT Lombardo, CR Stillman, SJ Padalino, C Mileham, et al. Calibration of a thomson parabola ion spectrometer and fujifilm imaging plate detectors for protons, deuterons, and alpha particles. *Review of Scientific Instruments*, 82(7):073301, 2011.

[47] M Cutroneo, L Torrisi, S Cavallaro, A Velyhan, et al. Thomson parabola spectrometry of laser generated plasma at pals laboratory. In *Journal of Physics: Conference Series*, volume 508, page 012020. IOP Publishing, 2014.

[48] Lorenzo Torrisi, Salvadore Cavallaro, Marcin Rosiński, Vincenzo Nassisi, Victor Paperny, and Igor Romanov. Post acceleration of ions emitted from laser and spark-generated plasmas. *Nukleonika*, 57:323–332, 2012.

[49] Kotaro Kondo, Takeshi Kanesue, Robert Dabrowski, and Masahiro Okamura. Angular distribution of laser ablation plasma. Technical report, Brookhaven National Laboratory (BNL) Relativistic Heavy Ion Collider, 2010.

[50] T Zeng, J Y Zhao, W Liu, and S L Chin. Backward angular distribution of air lasing induced by femtosecond laser filamentation. *Laser Physics Letters*, 11(7):075401, 2014.

[51] Andrea Thum-Jager and Klaus Rohr. Angular emission distributions of neutrals and ions in laser ablated particle beams. *Journal of Physics D: Applied Physics*, 32(21):2827, 1999.

[52] Jan Badziak, Piotr Parys, Jerzy Wolowski, Heinrich Hora, Josef Krasa, Leos Laska, and Karel Rohlena. Fast ion generation by a picosecond high-power laser. *Optica Applicata*, 35(1), 2005.

[53] L Andò, L Torrisi, S Gammino, J Beltrano, C Percolla, and O Parasole. Laser ion source for multiple ta ion implantation. In *Plasma Production by Laser Ablation*, pages 142–148, 2004.

[54] L Torrisi, S Cavallaro, M Cutroneo, L Giuffrida, J Krasa, D Margarone, A Velyhan, J Kravarik, J Ullschmied, J Wolowski, et al. Monoenergetic proton emission from nuclear reaction induced by high intensity laser-generated plasma a. *Review of Scientific Instruments*, 83(2):02B111, 2012.

[55] Giuseppe AP Cirrone, Massimo Carpinelli, Giacomo Cuttone, Santo Gammino, S Bijan Jia, Georg Korn, Mario Maggiore, Lorenzo Manti, Daniele Margarone, Jan Prokupek, et al. Elimed, future hadrontherapy applications of laser-accelerated beams. *Nuclear Instruments and Methods in Physics Research Section A: Accelerators, Spectrometers, Detectors and Associated Equipment*, 730:174–177, 2013.

[56] A Schempp. Radio-frequency quadrupole linacs. 2005.

[57] M Okamura, T Katayama, RA Jameson, T Takeuchi, T Hattori, and H Kashiwagi. Scheme for direct plasma injection into an rfq linac. *Laser and Particle Beams*, 20(3):451–454, 2002.

[58] S Gammino, L Torrisi, L Andò, G Ciavola, L Celona, L Laska, J Krasa, M Pfeifer, K Rohlena, E Woryna, et al. Production of low energy, high intensity metal ion beams by means of a laser ion source. *Review of scientific instruments*, 73(2):650–653, 2002.

[59] Hirotsugu Kashiwagi, Mitsuhiro Fukuda, Masahiro Okamura, RA Jameson, Toshiyuki Hattori, Noriyosu Hayashizaki, Kazuhiko Sakakibara, Junpei Takano, Kazuo Yamamoto, Yoshiyuki Iwata, et al. Acceleration of high current fully stripped carbon ion beam by direct injection scheme. *Review of scientific instruments*, 77(3):03B305, 2006.

[60] Jun Tamura, Masafumi Kumaki, Kotaro Kondo, Takeshi Kanesue, and Masahiro Okamura. Iron plasma generation using a nd: Yag laser pulse of several hundred picoseconds. *Review of Scientific Instruments*, 87(2):02A919, 2016.

[61] M Okamura. Laser ion source for high brightness heavy ion beam. *Journal of Instrumentation*, 11(09):C09004, 2016.

[62] Jun Tamura, Toshiyuki Hattori, Noriyosu Hayashizaki, Takuya Ishibashi, Taku Ito, T Kanesue, H Kashiwagi, and M Okamura. Multiple charge state ion beam acceleration with an rfq linac. *Venice, ITALY*, 2009.

[63] Y Fuwa, S Ikeda, M Kumaki, T Kanesue, M Okamura, and Y Iwashita. Beam dynamics of multi charge state ions in rfq linac.

[64] Hirotsugu Kashiwagi, Masahiro Okamura, Jun Tamura, and Junpei Takano. Direct plasma injection scheme with beam extraction in a radio frequency quadrupole linac cavity a. *Review of Scientific Instruments*, 79(2):02C716, 2008.

[65] T Yamamoto, K Kondo, M Sekine, M Okamura, and M Washio. Rfq linac commissioning and carbon^{4+} acceleration for ag^{15+} acceleration via direct plasma injection scheme. Technical report, BROOKHAVEN NATIONAL LABORATORY (BNL), 2012.

[66] J Alessi, D Barton, E Beebe, D Gassner, et al. Electron beam ion source preinjector project (ebis) conceptual design report. Technical report, BROOKHAVEN NATIONAL LABORATORY (US), 2005.

[67] J Alessi, E Beebe, S Binello, L Hoff, K Kondo, R Lambiase, V LoDestro, M Mapes, A McNerney, J Morris, et al. Commissioning of the ebis-based heavy ion preinjector at brookhaven. Technical report, Brookhaven National Laboratory (BNL) Electron Beam Ion Source, 2010.

[68] Masahiro Okamura, James Alessi, Edward Beebe, Michael Costanzo, Leonard DeSanto, Shunsuke Ikeda, James Jamilkowski, Takeshi Kanesue, Robert Lambiase, Daniel Lehn, et al. Performance of the low charge state laser ion source in bnl. In *13th Heavy Ion Accelerator Technology Conference (HIAT2015), Yokohama, Japan, 7-11 September 2015*, pages 274–276. JACOW, Geneva, Switzerland, 2016.

[69] T Kanesue, M Okamura, J Alessi, E Beebe, A Pikin, D Raparia, CJ Liaw, R Lambiase, M Sekine, and S Ikeda. The commissioning of the laser ion source for rhic ebis. *WEOAB01, Proceedings of IPAC*, 14, 2014.

[70] S Ikeda, M Kumaki, T Kanesue, and M Okamura. Effect of the solenoid in various conditions of the laser ion source at brookhaven national laboratory. *Review of Scientific Instruments*, 87(2):02A915, 2016.

[71] Karel Strijckmans. The isochronous cyclotron: principles and recent developments. *Computerized Medical Imaging and Graphics*, 25(2):69–78, 2001.

[72] S Gammino, L Ando, L Celona, G Ciavola, L Torrisi, J Krasa, L Laska, M Pfeifer, K Rohlena, B Badziak, et al. The eclisse project. In *Proc. Eur. Particle Accel. Conf., EPAC*, page 1709, 2002.

[73] S Gammino, L Torrisi, G Ciavola, L Andò, L Celona, S Manciagli, J Krasa, L Laska, M Pfeifer, K Rohlena, et al. The electron cyclotron resonance coupled to laser ion source for charge state enhancement experiment: Production of high intensity ion beams by means of a hybrid ion source. *Journal of applied physics*, 96(5):2961–2968, 2004.

[74] Lorenzo Giuffrida and Lorenzo Torrisi. Post-acceleration of ions from the laser-generated plasma. *Nukleonika*, 56:161–163, 2011.

[75] A Sciuto, L Torrisi, A Cannavò, G Ceccio, P Musumeci, M Mazzillo, and L Calcagno. Sic interdigit detectors for post-accelerated ions generated by laser plasma. *Vacuum*, 131:170–175, 2016.

[76] L Torrisi, L Giuffrida, M Rosinski, and C Schallhorn. Ge and ti post-ion acceleration from laser ion source. *Nuclear Instruments and Methods in Physics Research Section B: Beam Interactions with Materials and Atoms*, 268(17):2808–2814, 2010.

[77] M Cutroneo, A Mackova, L Torrisi, and V Lavrentiev. Laser ion implantation of ge in sio_2 using a post-ion acceleration system. *Laser and Particle Beams*, 35(1):72–80, 2017.

[78] Marco Borghesi. Laser-driven ion acceleration: State of the art and emerging mechanisms. *Nuclear Instruments and Methods in Physics Research Section A: Accelerators, Spectrometers, Detectors and Associated Equipment*, 740:6–9, 2014.

[79] L Torrisi, M Cutroneo, G Ceccio, A Cannavò, D Batani, G Boutoux, K Jakubowska, and JE Ducret. Near monochromatic 20 mev proton acceleration using fs laser irradiating au foils in target normal sheath acceleration regime. *Physics of Plasmas*, 23(4):043102, 2016.

[80] Lorenzo Torrisi, Lucia Calcagno, Mariapompea Cutroneo, Jan Badziak, Marcin Rosinski, Agnieszka Zaras-Szydlowska, and Alfio Torrisi. Nanostructured targets for tnsa laser ion acceleration. *Nukleonika*, 61(2):103–108, 2016.

[81] L Torrisi. Ion energy enhancement from tnsa plasmas obtained from advanced targets. *Laser and Particle Beams*, 32(3):383–389, 2014.

[82] TH Tan, GH McCall, and AH Williams. Determination of laser intensity and hot-electron temperature from fastest ion velocity measurement on laser-produced plasma. *The Physics of fluids*, 27(1):296–301, 1984.

[83] FN Beg, AR Bell, AE Dangor, CN Danson, AP Fews, ME Glinsky, BA Hammel, P Lee, PA Norreys, and Ma Tatarakis. A study of picosecond laser–solid interactions up to 10^{19} wcm^{-2}. *Physics of plasmas*, 4(2):447–457, 1997.

[84] EL Clark, K Krushelnick, M Zepf, FN Beg, M Tatarakis, A Machacek, MIK Santala, I Watts, PA Norreys, and AE Dangor. Energetic heavy-ion and proton generation from ultraintense laser-plasma interactions with solids. *Physical Review Letters*, 85(8):1654, 2000.